

JPL Publication 12-9

# **Galileo Interim Radiation Electron Model Update—2012**

*H. B. Garrett, M. Kokorowski, and I. Jun  
Jet Propulsion Laboratory, California Institute of Technology  
Pasadena, California*

*R. W. Evans  
Mori Associates  
Montrose, California*

**National Aeronautics and  
Space Administration**

**Jet Propulsion Laboratory  
California Institute of Technology  
Pasadena, California**

---

***March 2012***

This research was carried out at the Jet Propulsion Laboratory, California Institute of Technology, under a contract with the National Aeronautics and Space Administration.

Reference herein to any specific commercial product, process, or service by trade name, trademark, manufacturer, or otherwise, does not constitute or imply its endorsement by the United States Government or the Jet Propulsion Laboratory, California Institute of Technology.

© 2012 All rights reserved.

## ***ABSTRACT***

Measurements of the high-energy, omnidirectional electron environment, and magnetic field by the Galileo spacecraft Energetic Particle Detector (EPD) and Magnetometer (MAG) were used to revise the original Divine and GIRE models of Jupiter's trapped electron radiation in the jovian equatorial plane. 10-minute averages of the EPD data were averaged to provide an omni-directional differential flux spectrum at 0.238, 0.416, 0.706, 1.5, 2.0, 11.0, and 31 MeV (the latter based on estimates by Pioneer 10 and 11) in the jovian equatorial plane as a function of radial distance. This model has been combined with the original Divine model and recent synchrotron observations of jovian high energy electrons inside  $L = 4$  to yield estimates of the radiation environment from  $\sim 1$  to  $\sim 50$  Jupiter radii (1 jovian radius = 71,400 km). The revised model, referred to here as the Galileo Interim Radiation Electron model-Version 2 (or GIRE2), is intended to address several concerns with the original Divine/GIRE model. In particular, there were noticeable discontinuities at the boundaries between the GIRE and the Divine models. Also, the GIRE model did not extend out past  $L \sim 16$  and depended on the original Divine model for pitch angle distributions. The new GIRE2 model consists of an inner trapped omni-directional model between  $L = 7.2$  and  $22.5$  that has been modified to smoothly join onto the original Divine model between  $L = 7.2$  and  $10.5$  and onto a GIRE2 plasma sheet model between  $L = 17$  and  $25$ . The latter component is a function of jovian radius and height above the plasma sheet as given by the Khurana magnetic field model. The model, the steps leading to its creation, and relevant issues and concerns are discussed in detail in the report. The GIRE2 model, like its predecessor GIRE, represents a step forward in the study of the jovian radiation environment and is a useful and valuable tool for estimating that environment for future missions to Jupiter.

**KEY WORDS:** Jupiter, Radiation Models, Radiation Belts, Galileo Spacecraft, Europa, High Energy Electrons, Trapped Particles, Space Radiation



## ***EXECUTIVE SUMMARY***

Energetic Particle Detector (EPD) and Magnetometer (MAG) measurements from Galileo of the jovian high-energy, omnidirectional electron environment and the jovian magnetic field were reanalyzed along with synchrotron measurements of the inner jovian radiation belt to update the Divine electron model (Divine and Garrett, 1983) and the Galileo Interim Radiation Electron (GIRE) model (Garrett et al., 2003). The results of the analyses were used to revise the GIRE model of Jupiter's trapped electron radiation along the equatorial magnetic plane for the range 8 to 16 Jupiter radii (1 jovian radius = 71,400 km) and then to extend the original GIRE model range beyond the original 16 R<sub>J</sub> to 50 R<sub>J</sub>. This omnidirectional, equatorial model was then combined with the Divine model of jovian electron radiation (Divine and Garrett, 1983, with the revisions presented in Garrett et al., 2005) inside of L=8 to yield estimates of the high-energy electron radiation environment from ~1 to 50 R<sub>J</sub>. That model, referred to here as the Galileo Interim Radiation Electron model—Version 2 (GIRE2), the steps leading to its creation, and relevant issues and concerns are discussed in detail in the report. That effort and its major findings are summarized briefly below.

The first step in developing the new model was to combine the high-energy particle count rate data from the Johns Hopkins University Applied Physics Laboratory (JHU/APL) EPD with data on the location and magnetic environment at the spacecraft—specifically, the position of the Galileo spacecraft in various coordinate systems and the magnetic field vector (as modeled by the VIP4 magnetic field model (Connerney, 1998) inside L = ~16 and the Khurana magnetic field model (Khurana and Schwarzl, 2005) outside L = ~16) at the spacecraft. 10-minute averages of these data formed an extensive database of observations of the jovian radiation belts between Jupiter orbit insertion (JOI) in 1995 and the end of the mission in 2005. In addition, Prof. K. Khurana of UCLA provided timings for crossings of the jovian magnetic equator as determined by the MAG instrument.

As in the previous GIRE model, the second step was to convert the raw EPD count rates to scientific flux units. The EPD data are available in discrete channels ranging from ~0.2 MeV up to more than 11 MeV. The high-energy channels were not as well calibrated as desired before the launch of Galileo. To improve the calibration, a Monte Carlo radiation transport analysis (see Jun et al., 2002) was performed on the EPD design to determine the instrument response to the energetic electrons and protons in the jovian environment. Three-dimensional Monte Carlo radiation transport codes (Monte Carlo N-Particle Transfer Code (MCNP) version 4B for electrons and Monte Carlo N-Particle eXtended (MCNPX) version 2.2.3 for protons) were employed for this purpose. The results of that analysis were presented in the form of “geometric factors” for the high-energy channels. Of specific interest to the current study are the B1, DC2, and DC3 channels for electrons as these channels bracket the energy range of most interest for jovian radiation dose calculations. These channels had thresholds of approximately 1.5, 2.0, and 11.0 MeV, respectively. The geometric factor corresponding to each channel is an energy-dependent detector response function that relates the incident particle fluxes to instrument count rates. As demonstrated in Jun et al. (2002), the trend of actual data measured by the EPD was successfully reproduced using the geometric factors obtained by the MCNP/MCNPX programs and the experimenter-provided drawings.

In the third step, the geometric factors in combination with simplifying assumptions about the particle distribution functions were used to generate differential fluxes versus energy. Specifically, assuming that the electron particle flux spectra could be modeled over the 1–30 MeV energy range by a power law spectrum in energy, a method for inverting the count rates was devised that gave the electron fluxes versus energy. In addition, geometric factors for the lower energy EPD F1, F2, and F3 electron channels (0.239, 0.416, and 0.706 MeV, respectively) were provided by JHU/APL (the latter were updated from GIRE using more recent estimates provided by JHU/APL) that allowed the inclusion of lower energy fluxes. Finally, electron flux data from the Pioneer 10 and 11 spacecraft at 31 MeV were also included to extend the range of the model to higher energies. This gave flux estimates at 0.239, 0.416, 0.706, 1.5, 2.0, 11.0, and 31 MeV, to which a differential flux spectrum was fit of the form:

$$F(E) = J_0 E^{-A} \left(1 + \frac{E}{E_0}\right)^{-B} \quad (1)$$

where:

- $F =$  Differential electron flux as a function of  $E$
- $E =$  Electron energy (MeV)
- $J_0 =$  Constant (roughly the differential flux at  $E = 1$  MeV)
- $A =$  Constant (approximately the power law index for the low-energy component)
- $B =$  Constant ( $A+B$  is approximately the power law index for the high-energy component)
- $E_0 =$  Constant (approximately the breakpoint energy between low- and high-energy spectra)

This process allows the count rates to be converted to differential fluxes for each 10-minute interval which can then be integrated in energy to give the integral fluxes.

In the next step in the modeling process the count rates along the magnetic equator (as defined by Khurana) and, in the outer region, in distance above or below the magnetic equator were directly averaged for discrete spatial regions. The averages were then converted to fitted flux spectra using the above procedure. This process is done for the two different spatial regions—the trapped environment between 7.5 and 22.5 L and the plasma sheet environment between 17.5 and 50 R<sub>j</sub> (note: as will be discussed there is a difference between L and R<sub>j</sub> that needs to be taken into account). For the trapped environment, averages were computed in discrete radial intervals of 1.5 L along the magnetic equator for Galileo orbits between L-shells of ~8 and ~38 L. L is the distance, in R<sub>j</sub>, from Jupiter’s magnetic axis at which a given magnetic field line crosses the magnetic equator, the plane of which is slightly tilted and twisted with respect to the jovigraphic equatorial plane. For the outer plasma sheet, the averages were over radial distance from Jupiter and distance from the magnetic equator as defined by the Khurana model. These averages formed the base GIRE2 omnidirectional model.

At this time, the EPD pitch angle data are still being analyzed. Pitch angle information (i.e., the particle flux relative to the magnetic field direction) is required to estimate fluxes at high latitudes. In this new version, we chose to ignore the pitch angle variations for the trapped model and assume a “worst case”, omnidirectional flux at all locations along an L-shell (note: inside ~8 L, the Divine model pitch angles are assumed). This gives a complete model of the

inner radiation environment that can be used to provide estimates of the radiation environment. Unlike the original Divine model, which was based on single flybys by four spacecraft, the new inner GIRE2 model covers  $\sim 7$  years of data and more than 30 orbits of Jupiter by a single spacecraft, providing a significant improvement in our knowledge of the variations in the jovian radiation environment.

Outside of  $\sim 17$  R<sub>j</sub>, all the EPD count rates were fit with a simple functional form in terms of  $R$  (the radial distance from Jupiter to the point) and the parameter  $Z_{\text{map}}$  as defined by the Khurana magnetospheric model (Khurana and Schwarzl, 2005).  $Z_{\text{map}}$  represents the distance from the model's estimated center of the jovian plasma sheet and the observational point. It is variable in local time relative to the Sun and radial distance from Jupiter. The functional form of the outer model is given by:

$$\log_{10}(CR_i(R, Z_{\text{map}})) = A_{0i} + B_{0i}R + C_{0i}Z_{\text{map}} \quad (2)$$

where:

$$\begin{aligned} CR_i &= \text{Electron count rates at } E_i \\ E_i &= 0.239, 0.416, 0.706, 1.5, 2.0, 11.0 \text{ MeV for } i = 1-6 \\ A_{0i}, B_{0i}, C_{0i} &= \text{Constants determined by fits to data for } i = 1-6 \\ Z_{\text{map}} &= \text{Perpendicular distance from the jovian plasma sheet} \\ R &= \text{Radial distance in Rj from Jupiter's center} \end{aligned}$$

The count rates (along with a similar fit to the Pioneer 10 and 11 31 MeV data) averaged into discrete  $R$  and  $Z_{\text{map}}$  bins were then converted to spectra as defined in Eq. 1. The resulting constants (Eq. 1) were then individually fit in terms of  $(R, Z_{\text{map}})$  with an equation of the form:

$$\begin{aligned} Y_k(R, Z_{\text{map}}) &= A_{k0} + A_{k1}R + A_{k2}Z_{\text{map}} + A_{k3}R^2 + A_{k4}Z_{\text{map}}^2 + A_{k5}R \cdot Z_{\text{map}} + A_{k6}R^2Z_{\text{map}} + \\ &+ A_{k7}R \cdot Z_{\text{map}}^2 + A_{k8}R^2Z_{\text{map}}^2 \end{aligned} \quad (3)$$

where:

$$Y_k = J_0, A, B, E_0 \text{ for } k=1,4 \text{ are the constants in Eq. 1 used to generate the differential flux } F_{\text{outer}}(E, R, Z_{\text{map}})$$

This gives a simple representation in  $(R, Z_{\text{map}})$  over the region outside the  $\sim 17$  L magnetic shell (as determined by the Connerney magnetic field). The fact, however, that the inner trapped model is based on the L shell and the Connerney magnetic field model while the outer plasma sheet model is based on the Khurana model and  $(R, Z_{\text{map}})$  means there is a discontinuity between the two models that varies along the  $\sim 17$  L shell and in local time. The two models were smoothly merged by assuming the following approximation in the region 17 to 22.5 L:

$$F2(E, L, R_j, Z_{\text{map}}) = F_{\text{inner}}(E, L) \cdot (22.5 - L) / 5.5 + F_{\text{outer}}(E, R_j, Z_{\text{map}}) \cdot (L - 17) / 5.5 \quad (4)$$

where:

$$F2 = \text{Interpolated differential electron flux as a function of } (E, L, R, Z_{\text{map}}) \text{ between } 17\text{--}22.5 \text{ L; Coordinate system is System III}$$

$F_{inner}$  = Differential flux as determined for the inner trapped region

$F_{outer}$  = Differential flux as determined for the outer plasma sheet region

This method was also used to smooth the new inner trapped model with the Divine model inside an L shell of 8.

As for the original GIRE model, there remain several opportunities for refinement and extension of the model—hence the terminology “Interim” in “Galileo Interim Radiation Electron” model. In particular, there is an inconsistency in the fluxes estimated from the B1 and DC2 channels when extrapolated to 1 MeV. Although a factor of 2-3 difference was found between the two estimates, this agreement was deemed adequate in formulating a model of the omnidirectional electron fluxes as it is on the order of the observed uncertainties in overall model when compared with the actual data. There were also a few “extreme events” (e.g., orbit C22) where the fluxes were a factor of 100 higher than normal for a short time—these made up only ~1% of the 10-minute values and apparently had little effect on the data averages. Finally, the issue of pitch angle distributions for the electrons, particularly in the trapped inner zone, still needs to be addressed though any corrections it would introduce should reduce the off-equatorial fluxes. While work remains to be done in studying “extreme variations” (e.g., orbit C22), in completing the Galileo pitch angle analysis, and in reconciling remaining inconsistencies in the data, the GIRE2 model clearly represents a significant step forward in the study of the jovian radiation environment and is a useful and valuable tool for estimating that environment for future space missions.



## ***TABLE OF CONTENTS***

<b>INTRODUCTION .....</b>	<b>1</b>
<b>GALILEO ENERGETIC PARTICLE DETECTOR (EPD)</b>	
<b>—1.5–11 MEV ELECTRONS.....</b>	<b>2</b>
<b>EPD LEMMS AND MCNP/MCNPX MODELING .....</b>	<b>4</b>
<b>GEOMETRIC FACTOR TO FLUX—B1, DC2, AND DC3.....</b>	<b>6</b>
<b>GEOMETRIC FACTOR TO FLUX—F1, F2, AND F3.....</b>	<b>11</b>
<b>DATA COMPARISONS .....</b>	<b>12</b>
<b>“REAL TIME” EPD DATA VERSUS “PLAYBACK” DATA.....</b>	<b>17</b>
<b>AVERAGING PROCESS .....</b>	<b>19</b>
<b>DISPLAY OF DATA ACROSS MODE CHANGES.....</b>	<b>19</b>
<b>COMPARISON OF DATA MODES .....</b>	<b>20</b>
<b>ESTIMATING THE 31 MEV ELECTRON FLUX .....</b>	<b>21</b>
<b>DATA CONSISTENCY—COMPARISONS WITH PIONEER</b>	
<b>AND VOYAGER.....</b>	<b>24</b>
<b>DATA CONSISTENCY—SUMMARY .....</b>	<b>27</b>
<b>DEVELOPING AN INNER ZONE OMNIDIRECTIONAL,</b>	
<b>EQUATORIAL MODEL .....</b>	<b>27</b>
<b>DEVELOPING AN OUTER ZONE OMNI-DIRECTIONAL MODEL.....</b>	<b>32</b>
<b>SPICE.....</b>	<b>34</b>
<b>JOVIAN MAGNETIC FIELD MODEL .....</b>	<b>35</b>
<b>GALILEO EPD DATA .....</b>	<b>39</b>
<b>FITTING PROCESS .....</b>	<b>40</b>
<b>CONVERTING THE OUTER MODEL COUNT RATES TO FLUXES.....</b>	<b>46</b>
<b>COMBINING THE INNER AND OUTER GIRE2 MODELS .....</b>	<b>47</b>
<b>CONCLUSIONS .....</b>	<b>49</b>
The GIRE2 Omnidirectional, Equatorial Flux Model-Summary .....	49
<u>Issues with GIRE2</u> .....	50
<u>Limits on GIRE2 and its Validity</u> .....	51
<u>Accomplishments</u> .....	54
<b>ACKNOWLEDGMENTS.....</b>	<b>54</b>
<b>REFERENCES.....</b>	<b>55</b>
<b>APPENDIX I. ACRONYMS AND ABBREVIATIONS .....</b>	<b>57</b>

## **FIGURES**

Fig. 1. Detail of the EPD LEMMS detector head (Williams et al., 1992).....	3
Fig. 2. LEMMS modeling used in the MCNP/MCNPX simulations: (a) Cross sectional view and (b) Iso-view.....	5
Fig. 3. Geometric factors estimated for the EPD B1, DC2, and DC3 channels. “p” stands for proton channels and “e” for electron channels. Note that B1(p) is 0.....	7
Fig. 4. Assuming EPD counts are given by Eq. 1 and $J(E) = (E/E_0)^{-x}$ (i.e., $J_0 = 1$ ), the estimated count rates for B1, DC2, and DC3 are plotted versus the coefficient X. ....	10
Fig. 5. Assuming EPD counts are given by Eq. 1 and $J(E) = J_0 (E/E_0)^{-x}$ , the ratios [Cts(DC3)/Cts(B1)] and [Cts(DC3)/Cts(DC2)] are plotted vs. the coefficient X. ....	11
Fig. 6. DC2 raw count rates versus B1 raw count rates for the EPD (data are through Day 52, 2000).....	13
Fig. 7. DC3 raw counts versus B1 raw count rates for the EPD.....	13
Fig. 8. DC3 raw count rates versus DC2 raw count rates for EPD.....	13
Fig. 9. “Clean” EPD raw counts per second for DC2 and B1 for 10-minute average intervals. (The line is for an index of 1.) .....	14
Fig. 10. The electron differential flux at 1 MeV estimated from the 10-minute count rate pairs (B1,DC3) and (DC2,DC3). Over the flux range of interest, the DC2 fluxes are approximately a factor of 1.5–3 times higher than the B1 fluxes at 1 MeV. (Note: The fits are only for $B1 > 10^4$ .) .....	15
Fig. 11. The estimated fluxes at 1 MeV for fits to the (F1,F2,F3) EPD channels are compared with the fluxes predicted by the (B1,DC3) pair. (Note: The fits are only for $B1 > 10^4$ .)	16
Fig. 12. The estimated fluxes at 1 MeV for fits to the (F1,F2,F3) EPD channels are compared with the fluxes predicted by the (DC2,DC3) pair. (Note: The fits are only for $B1 > 10^4$ .) .....	16
Fig. 13. Representative examples of the pitch angle distributions for B1, DC2, and DC3 for the Playback data. Note that the differences in motor position correspond to varying degrees of obscuration—the highest values at each position represent the un-obscured data. ....	17
Fig. 14. Plots of EPD channels DC2, DC3, and B1 as functions of time for two Galileo orbits. Center segments in each plot are the 10-minute averaged Record Mode data, and side segments are adjacent Real Time data segments. Left plot data collected at $R_J \cong 130$ and right plot at $R_J \cong 9.5$ . ....	18
Fig. 15. Plot of Real Time data particle flux vs. 10-minute averaged Record Mode data at adjacent point. Legends identified “<” are points across transitions from Real Time to Record Mode. Legends identified “>” are across transitions from Record Mode to Real Time. The upward curve at high flux rates suggests an uncorrected dead time effect in the Record Mode data. ....	18
Fig. 16. Data of Figure 15 replotted following a dead time correction to the Record Mode data, assuming a non-extendable dead time of 1.6 $\mu$ sec.....	21
Fig. 17. Pioneer 10 differential fluxes (in units of electrons/cm <sup>2</sup> -s-MeV) for Jupiter closest approach on Day 338, 1973. GTT data are from the Planetary Data System.....	22
Fig. 18. Pioneer 11 differential fluxes (in units of electrons/cm <sup>2</sup> -s-MeV) for Jupiter closest approach on Day 337, 1974. GTT data are from the Planetary Data System.....	23
Fig. 19. Fits to a representative EPD differential flux spectrum. The 7 diamonds correspond to the best-case EPD flux estimates at 0.239, 0.416, 0.706, 1.5, 2.0, 11.0, and 31.0 MeV.	

(The 31 MeV value is from Pioneer 10 and 11.) “Composite Fit” corresponds to a functional fit to these 7 flux estimates using Eq. 15. ....	25
Fig. 20. Estimates of the omnidirectional differential electron flux (particles/(cm <sup>2</sup> -s-sr-MeV) versus distance from Jupiter (R <sub>J</sub> ) at 1.5 MeV. Dark blue points correspond to the EPD estimated fluxes for the Galileo 10-minute averages. The lavender crosses correspond to the equivalent Pioneer/Voyager (i.e., Divine Model) estimates for the same spatial locations. ....	26
Fig. 21. Estimates of the omnidirectional differential electron flux (particles/(cm <sup>2</sup> -s-sr-MeV) versus distance from Jupiter (R <sub>J</sub> ) at 11 MeV. Dark blue crosses correspond to the EPD estimated fluxes for the Galileo 10-minute averages. The lavender points correspond to the equivalent Pioneer/Voyager (i.e., Divine Model) estimates for the same spatial locations. ....	26
Fig. 22. DC3 counts versus distance from Jupiter in units of R <sub>J</sub> for individual Galileo orbits G02 to I33. Note the radial oscillations in each orbit. ....	28
Fig. 23. DC3 counts versus L-shell for Galileo orbits G02 to I33. ....	29
Fig. 24. Averages of the 10-minute EPD count rate data along the magnetic equator in discrete 1.5 L-shell bins. ....	30
Fig. 25. Line plots of the differential electron fluxes as predicted by the inner region GIRE and GIRE2 models. ....	32
Fig. 26. Schematic diagram of an ideal Harris Current sheet. The magnetic field $B_\theta$ is equal and opposite on either side of $Z_{map}=0$ . The field strength reduces from $B_\theta$ and $Z_{map}=\pm L$ to zero at the neutral line. The scale L in this figure is unrelated to the McIlwain L parameter. [From Parks, 1991] ....	33
Fig. 27. Magnetic field line traces at 315° W longitude using the VIP4 (blue) and Khurana (red) models. Each trace begins at z=0 in SIII coordinates. Traces should be interpreted qualitatively because of a slight skew in the longitudinal projection. [From Figure 3 in Kokorowski, 2010] ....	34
Fig. 28. A schematic diagram that includes the normal distance between the current sheet and a given location of interest. The line labeled Z is what we are calling $Z_{map}$ in this report to emphasize that it is in the direction normal to the current sheet. [From Khurana, 1992] ....	35
Fig. 29. EPD DC3 (>11 MeV e <sup>-</sup> ) count rate during outbound portion of orbit I33. The count rate falls sharply near 62 R <sub>J</sub> . This is interpreted as a transition from the jovian magnetosphere to solar wind. Data collected outside of the magnetosphere are not included in the construction of GIRE2. ....	40
Fig. 30. F1 174-304 keV electron count rate averages (solid) and modeled fit (dashed) as a function of R for different $Z_{map}$ values between 0 and 12.5 R <sub>J</sub> . ....	43
Fig. 31. F2 304-527 keV electron count rate averages (solid) and modeled fit (dashed) as a function of R <sub>J</sub> for different $Z_{map}$ values between 0 and 12.5 R <sub>J</sub> . ....	43
Fig. 32. F3 527-884 keV electron count rate averages (solid) and modeled fit (dashed) as a function of R <sub>J</sub> for different $Z_{map}$ values between 0 and 12.5 R <sub>J</sub> . ....	44
Fig. 33. B1 1.5-10.5 MeV electron count rate averages (solid) and modeled fit (dashed) as a function of R <sub>J</sub> for different $Z_{map}$ values between 0 and 12.5 R <sub>J</sub> . ....	44
Fig. 34. DC2 >2 MeV electron count rate averages (solid) and modeled fit (dashed) as a function of R <sub>J</sub> for different $Z_{map}$ values between 0 and 12.5 R <sub>J</sub> . ....	45

Fig. 35. DC3 >11 MeV electron count rate averages (solid) and modeled fit (dashed) as a function of $R_J$ for different $Z_{map}$ values between 0 and 12.5 $R_J$ .	45
Fig. 36. The outer model differential electron fluxes (at $Z_{map} = 0$ ) compared with the inner model estimates versus $L$ as determined by the Khurana magnetic field model.	47
Fig. 37. “GIRE+Divine (2003)” integral fluxes ( $n^\#/\text{cm}^2\text{-s}$ ) at: 0.1, 1.0, 10.0, 30.0 MeV showing discontinuities at $\sim 8$ and $\sim 16 R_J$ .	48
Fig. 38. Comparisons between original “GIRE+Divine (2003)” and the new “GIRE (2011)” integral fluxes ( $n^\#/\text{cm}^2\text{-s}$ ) at: 0.1, 1.0, 10.0, 30.0 MeV along the jovian equatorial plan at $110^\circ\text{W}$ . Note that the discontinuities between the models have virtually disappeared in the GIRE2 model.	49
Fig. 39. Comparisons between all (red) EPD data, Khurana crossings (blue), and new “GIRE(2011)” (green) electron integral fluxes ( $n^\#/\text{cm}^2\text{-s}$ ) at A) 2.0 and B) 11.0 MeV	52
Fig. 40. Meridian contours of GIRE2 (A) 1 MeV and (B) 10 MeV electron integral fluxes ( $\text{cm}^2\text{-s}^{-1}$ ) for the $110^\circ\text{W}$ meridian and for the Sun at $110^\circ\text{W}$ . Note that the “outer” GIRE2 model has been extrapolated inwards of $\sim 15 R_J$ and up to $\pm 20$ in $Z_{map}$ to fill in the region outside an $L$ of 22.5.	53

## TABLES

Table 1. Description of the LEMMS high-energy electron and protons channels considered in this study (Williams et al., 1992).	4
Table 2. Electronic threshold energies used in the channels described in Table 1 (in MeV) (Williams et al., 1992).	4
Table 3. Electron geometric factors in $\text{cm}^2\text{-sr}$ for the LEMMS high-energy channels.	8
Table 4. Proton geometric factors in $\text{cm}^2\text{-sr}$ for the LEMMS high-energy channels.	9
Table 5. The energy bands, average energies for those bands, and the estimated geometric factor-efficiency factor ( $GF'(X)$ ) for the corresponding energy spectra given by Eq. 4. These latter values were taken from Lagg (1998).	11
Table 6. Table of EPD detector dead time constants for the energetic electron study, provided by T. H. Choo at JHU/APL.	20
Table 7. Fitted electron differential flux parameters corresponding to Eq. 15. Units are $(\text{cm}^2\text{-s-sr-keV})^{-1}$ . The model results produce an omni-directional flux.	31
Table 8. Spherical harmonic Schmidt coefficients used in VIP4 and Khurana models for the internal component of the magnetic field. The Khurana (1997) model uses the $O_6$ model coefficients. However, the most up-to-date version of the Khurana model (used in this analysis) contains coefficients identical to those used in the VIP4 model.	37
Table 9. Radial bin values used for the outer portion of GIRE2.	41
Table 10. $Z$ bin values used for the outer portion of GIRE2.	41
Table 11. GIRE2 EPD count rate fit results for each energetic electron energy channel for outer model. Each coefficient is accompanied by a 95% confidence interval estimate. The adjusted R-squared value is also provided as a goodness-of-fit statistic.	42
Table 12. Constants for Eq. 24 used to give $(J_0, A, B, E_0)$ for the outer electron model distribution as a function of $(R, Z_{map})$ .	46

# GALILEO INTERIM RADIATION ELECTRON MODEL UPDATE—2011

H. B. Garrett<sup>a</sup>, M. Kokorowski<sup>a</sup>, I. Jun<sup>a</sup>, and R. W. Evans<sup>b</sup>

<sup>a</sup>*Jet Propulsion Laboratory, California Institute of Technology, 4800 Oak Grove Drive, Pasadena, California 91109*

<sup>b</sup>*Mori Associates, 2550 Honolulu Blvd., Montrose, California 91020*

## INTRODUCTION

This report utilizes the Galileo Energetic Particle Detector (EPD) and Magnetometer (MAG) measurements of the charged particles near Jupiter to estimate the jovian radiation environment. Specifically, the report describes the steps undertaken to update the current GIRE model of Jupiter's trapped electron radiation in the jovian equatorial magnetic plane in the range  $\sim 8$  to  $\sim 16$  Jupiter radii (1 jovian radius = 71,400 km) and then to extend the original GIRE model range out to 50 R<sub>j</sub>. This omnidirectional, equatorial model was then combined with the Divine model of jovian electron radiation (Divine and Garrett, 1983), with the revisions presented in Garrett et al. (2005) inside of  $L = 8$  to yield estimates of the high-energy electron radiation environment from  $\sim 1$  to 50 R<sub>j</sub>. The revised model will be referred to here as the Galileo Interim Radiation Electron—Version 2 (or GIRE2) model.

The first step in developing the model was to combine 10-minute averages of the high-energy particle count rate data from the Johns Hopkins University Applied Physics Laboratory (JHU/APL) EPD with data on the location and magnetic environment at the spacecraft—specifically, the position of the Galileo spacecraft in various coordinate systems and the magnetic field vector (as modeled by the VIP4 magnetic field model inside an  $L$  shell of 7 and the Khurana magnetic field model outside of 17  $L$ ) at the spacecraft. 10-minute averages of these data represent an extensive database of observations of the jovian radiation belts between Jupiter orbit insertion (JOI) in 1995 and the end of the mission in 2005. Of particular importance to the new model, only data associated with the crossings of the jovian magnetic equator (provided by K. Khurana) as determined by the MAG instrument were used to compute the inner, trapped model rather than the entire data set. Secondly, the Khurana magnetic field model was used outside of  $\sim 17 L$  to order the Galileo observations in  $R$  and  $Z_{\text{map}}$ —this region was not updated in the original GIRE version (Garrett et al., 2003).

Despite the success of the original GIRE modeling process, there remained several opportunities for refinement and extension of the model—hence the terminology “Interim” in its name. A key step in the original process was the determination of the EPD geometric factors. Based on these estimates, a self-consistent method for converting the observed counts into estimates of the electron flux was developed. This report, in addition to reviewing the original steps in that process, extends the GIRE model, which was limited to an  $L$  of  $\sim 16$ , to 50 R<sub>j</sub>. Also, the geometric factors for the EPD F channels are updated with more recent estimates by APL. The discontinuities at the boundaries between the innermost Divine model and the new trapped model and between the trapped model and the outer plasma sheet model are resolved. Finally, the Pioneer 10 and 11 31-MeV electron data are revisited and an attempt made to more consistently incorporate these critical data into the model. Two outstanding issues not

considered here, that will need to be considered in future studies, are the inclusion of data from the Galileo high resolution EPD pitch angle measurements (incorporating these data will allow extension of the GIRE model to higher latitudes) and the development of a Galileo-based proton model.

### ***GALILEO ENERGETIC PARTICLE DETECTOR (EPD)—1.5–11 MEV ELECTRONS***

The primary data set used in this study is from the Galileo EPD instrument (Williams et al., 1992). This instrument provides  $4\pi$  angular coverage and spectral measurement for  $Z \geq 1$  ions, for electrons, and for the elemental species helium through iron. The EPD consists of two bi-directional telescopes mounted on a platform that can be stepped in look angle. The two bi-directional telescopes are called the Low-Energy Magnetospheric Measurement System (LEMMS) and the Composition Measurement System (CMS). Of these two instruments, the LEMMS provides the information most directly applicable to the high-energy, trapped radiation environment and was the focus of this study. The LEMMS telescopes are designed to measure low to medium energy ion and electron fluxes with wide dynamic range and high angular and temporal resolution. The LEMMS detector head, shown in Fig. 1, is a double-ended telescope containing eight heavily shielded detectors (silicon solid state totally depleted surface barrier type) providing measurements of electrons from 15 keV to  $>11$  MeV, and ions from 22 keV to  $\sim 55$  MeV in 32 rate channels. The LEMMS design uses a baffled collimator and shaped-field magnetic deflection to provide separation between ions and electrons in detectors A, B, E, and F ( $0^\circ$  end in Fig. 1), and extends the measurements to much higher energies via detectors C and D in the oppositely-directed double-absorber-detector telescope stack on the  $180^\circ$  end.

Of the 32 LEMMS channels, the most important ones for radiation modeling are the electron and proton channels for energies above  $\sim 1$  MeV, as these contribute the majority of the dose for typical ( $\geq 2.5$  mm or 100 mils) spacecraft shielding levels common for jovian missions. Therefore, the B0, B1, B2, DC0, DC1, DC2, and DC3 channels were the primary channels studied in this paper (note: the lower energy F channels are included in the analysis, but ultimately do not contribute much to the actual dose calculations as their energies are below 1 MeV). These channels involve the detectors A, B, C, and D. The characteristics of these channels are summarized in Table 1. The last column of Table 1 shows the logic for each channel, and Table 2 shows the detector threshold energies relevant to the channels mentioned above (Williams et al., 1992). The information in Tables 1 and 2 are used together to form a complete channel description. For example, to register as a count in the B0 channel, a particle should deposit more than or equal to 0.820 MeV in the detector A, more than or equal to 0.075 MeV in the detector B, and less than 2.170 MeV in the detector C. Other channels can be understood in a similar fashion.

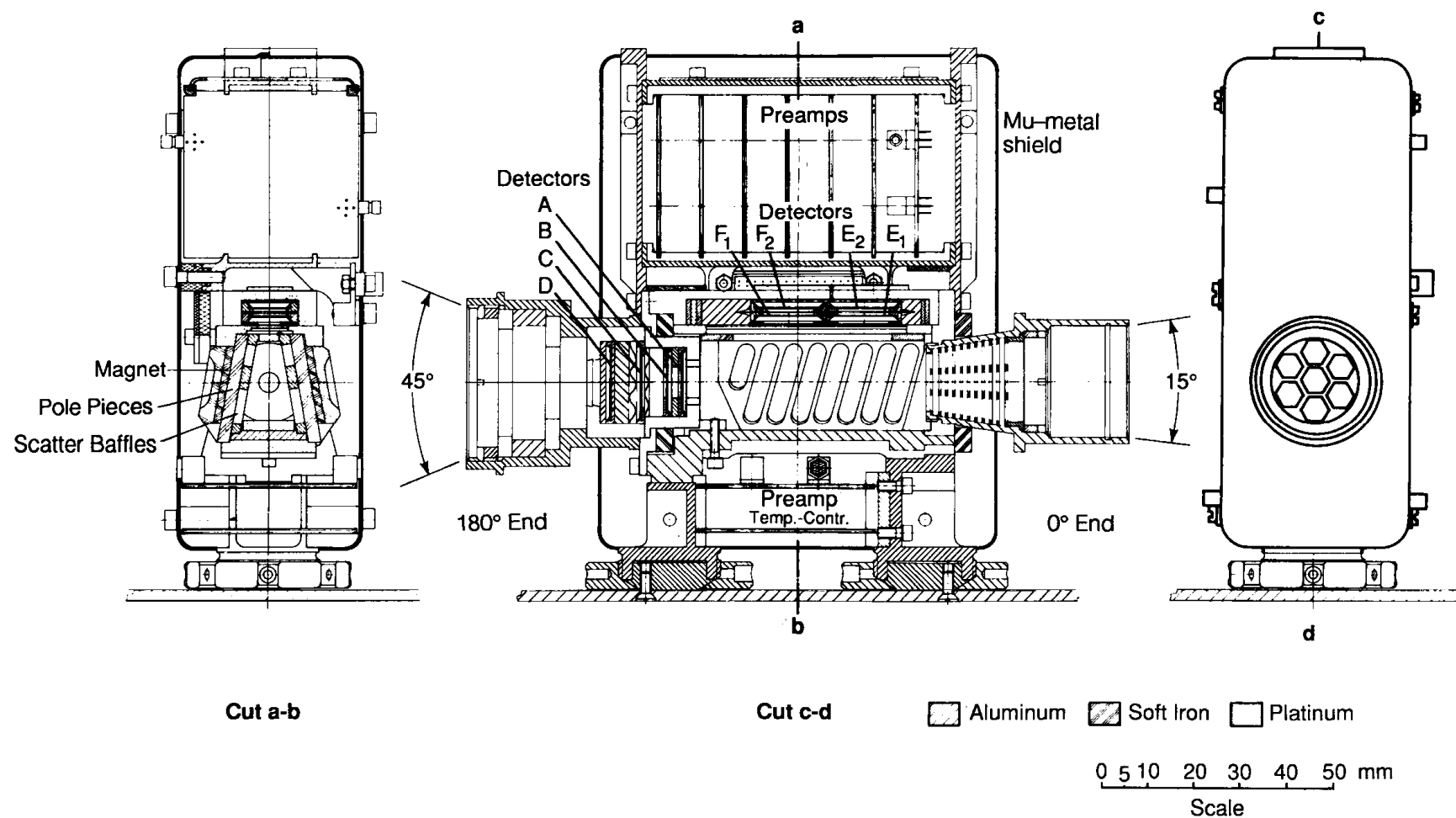


Fig. 1. Detail of the EPD LEMMS detector head (Williams et al., 1992).

**Table 1. Description of the LEMMS high-energy electron and protons channels considered in this study (Williams et al., 1992).**

Channel Name	Species	Nominal Energy Range (MeV)	Channel Logic
B0	$Z = 1$	3.20–10.1	A7 B1 NC2
B1	Electrons	1.5–10.5	A2 NA4 B1 NB2 NC2
DC0	$Z \geq 1$	14.5–33.5	NB1 D2 NC1
DC1	$Z \geq 1$	51–59	NB1 C2 D1
DC2	Electrons	$\geq 2$	NB1 D1 ND2
DC3	Electrons	$\geq 11$	NB1 C1 NC2 D1

### ***EPD LEMMS AND MCNP/MCNPX MODELING***

Detector A is modeled as a silicon disk 25 mm<sup>2</sup> in area and 102  $\mu$ m thick, and detector B as a silicon disk 35 mm<sup>2</sup> in area and 984  $\mu$ m thick. There is  $\geq 12$  g/cm<sup>2</sup> thick platinum-iridium shielding around the detectors A/B. In addition to this very thick shielding, the detectors were designed to avoid background contamination by using coincident/anti-coincident schemes between detectors. The 0° end of the LEMMS telescope uses aluminum baffles and magnetic deflection to prevent the electrons with energy <1 MeV from reaching detector A directly and to minimize the scattering in the deflection region.

**Table 2. Electronic threshold energies used in the channels described in Table 1 (in MeV) (Williams et al., 1992).**

A1, A2, A3, A4, A5, A6, A7:	0.018, 0.034, 0.055, 0.110, 0.272, 0.510, 0.820
B1, B2, B3:	0.075, 0.800, 8.270
C1, C2:	0.162, 2.170
D1, D2:	0.133, 1.860

The C and D detectors are  $\sim 199$  mm<sup>2</sup>,  $\sim 500$   $\mu$ m thick devices separated by 0.48 cm. The detectors are shielded from the sides by  $> 7.24$  g/cm<sup>2</sup> of platinum. The rear-facing collimator provides a directional field of view of  $\sim 45^\circ$ . In the look direction, the D detector is shielded by a 2 mm thick (0.35 g/cm<sup>2</sup>) magnesium disk. Between C and D, there is an additional absorber of 3.2 mm of brass (2.8 g/cm<sup>2</sup>).

All of these design features and the information from the EPD engineering drawings were incorporated into a 3-dimensional model of the EPD (illustrated in Fig. 2) for use in the subsequent Monte Carlo modeling. Note that to simplify the model, cylindrical geometry was used when appropriate. For example, the 0° end of the actual LEMMS telescope is a complicated hexagonal shape with many internal structures (11 aluminum baffle plates, pole pieces, magnet, etc.) intended to minimize the scattering in the deflection region. The 0° end of the telescope also uses the magnetic field to deflect low-energy (<1 MeV) electrons away from detector A. The 0° end deflection region was modeled as a simplified cylindrical platinum tube in the Monte Carlo simulations. Scattering was suppressed by ceasing to follow those particles that hit the tube. The detailed geometry of the A/B detectors was estimated to give a geometrical factor of 0.006 cm<sup>2</sup>-sr (Williams et al., 1992). This geometric factor did not include the intrinsic efficiency of the detector. In the simulation, a



geometry consistent with this number was adopted. That is, the diameter and length of the platinum tube were chosen specifically to give a solid angle opening of  $0.006 \text{ cm}^2\text{-sr}$  for the detector using the expression in Thomas and Willis (1972). This simplification can be justified because in the Monte Carlo simulation no scatterings or interactions of the incoming source electrons were allowed in the deflection region, which satisfies the intent of the actual instrument design. (<1 MeV electrons cannot reach detector A directly, and the scattering is minimized in the deflection region.)

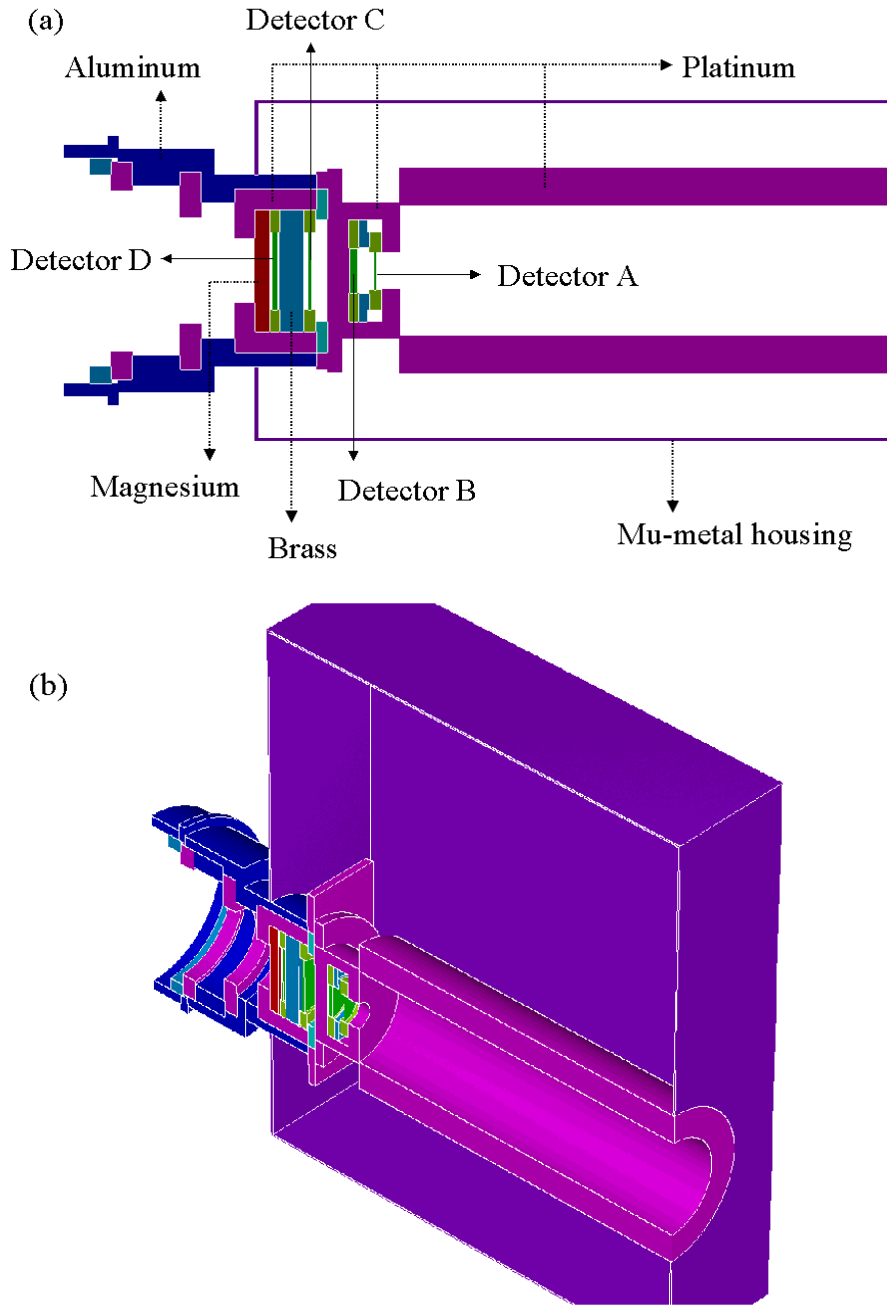


Fig. 2. LEMMS modeling used in the MCNP/MCNPX simulations: (a) Cross sectional view and (b) Iso-view

To determine the instrument geometric factors, a series of Monte Carlo calculations were performed to obtain the responses of the detectors as functions of incident particle energy. The energy range covered in the study was  $1 \leq E \leq 100$  MeV. MCNP version 4B was used for the electron transport, and MCNPX version 2.2.3 was used for the proton transport. The total number of source particles simulated for each case ranged from 1 million to 50 million, to ensure that the uncertainties of the results in the important energy ranges are reasonably low, e.g.,  $\sim 10\%$ . Basically, this is the simulation of a counting experiment, so the uncertainties follow Poisson statistics. Mono-energetic incident particles were simulated as an isotropic particle distribution. Each particle was tracked from the entry point of the problem geometry until its energy became lower than the code's cut-off energies (1 keV for electrons and 1 MeV for protons) or until it escaped from the problem geometry. Preliminary analysis indicated the source particles incident from sides of the instrument did not contribute much to the count rates due to thick shields ( $>7.24$  g/cm<sup>2</sup> of platinum for C/D detectors and  $>12$  g/cm<sup>2</sup> of platinum-iridium for A/B detectors). Therefore, these particles were not followed to speed up the Monte Carlo calculations. As described above, particles were also not followed if they hit the inner wall of the platinum tube in the 0° end of the telescope. However, the particles that traversed the collimator regions in either end of the instrument were followed rigorously, including the effects of scattering and secondary particle generation within the detectors and in their surrounding support structure.

The tracking of each particle was possible using the PTRAC option built into MCNP/MCNPX. The energy depositions in the detectors A, B, C, and D from each source particle and its secondary particles were recorded in the output, which was subsequently post-processed to check whether the total energy deposited in the detectors satisfied the specific channel logic described in Table 1. If it was satisfied, then the source particle was considered as a legitimate count for that channel. The computations were repeated for other energies. The results are depicted in Fig. 3. Note that no attempt was made to generate curve fits to these geometric factors because no single analytical form would be applicable to all channels. In the figure, straight lines were drawn between each data point simply to show the trend of the geometric factors. For clarity, the error bars are not shown in the figure. The values of the geometric factors and their uncertainties at selected energies are presented in Tables 3 and 4 for electrons and protons, respectively.

### ***GEOMETRIC FACTOR TO FLUX—B1, DC2, AND DC3***

Given the geometric factors in Fig. 3, the EPD high-energy electron B1, DC2, and DC3 count rates can be converted to flux estimates at selected energies. For the typical ambient environment at Jupiter, the proton contribution to the count rate was found to be insignificant and will be ignored in the subsequent discussion. The convolution of the actual electron spectra with the geometric factors yields complex results, making their interpretation less than straightforward at best. As will be discussed, simplifying assumptions about the functional form of the energy spectrum are necessary if meaningful flux estimates are to be made.

When convolved with representative jovian spectra, the electron geometric factors in Fig. 3 for B1, DC2, and DC3 appear to contribute to the count rates primarily over the energy range from  $\sim 1$  to  $\sim 100$  MeV. Previous studies of the jovian trapped radiation environment

indicate that to first order, the flux can be crudely represented over this range by a function of the form  $J_0 E^{-X}$  where  $X$  is a positive number between 1 and 5 and  $J_0$  is the differential electron flux at 1 MeV. So, to first order, the count rate for a given EPD channel can be estimated by:

$$(cts / s)_{APL} = \int_0^{\infty} \frac{dI(E)}{dE} G(E) \cdot dE = J_0 \int_0^{\infty} \left( \frac{E_i}{E_0} \right)^{-X} G(E) \cdot dE \cong J_0 \sum_{i=1}^{\infty} \left( \frac{E_i}{E_0} \right)^{-X} G(E_i) \cdot \Delta E_i \quad (1)$$

where:

- $E_i$  = Energy steps ( $E_i = 1$  MeV here)
- $E_0$  = 1 MeV
- $\Delta E_i$  = Energy interval between  $E_i$  and  $E_{i+1}$
- $(cts / s)_{APL}$  = Counts per second as reported by the APL EPD channel (B1, DC2, DC3)
- $I(E_i)$  = Integral electron flux at  $E_i$
- $\frac{dI(E_i)}{dE}$  =  $J(E_i)$  = Differential electron flux at  $E_i$
- $J(E_i)$  =  $J_0 (E_i/E_0)^{-X}$  (in units of  $(\text{cm}^2\text{-s-sr-MeV})^{-1}$ )
- $X$  = Unit-less constant
- $J_0$  = Constant in units of  $(\text{cm}^2\text{-s-sr-MeV})^{-1}$
- $G(E_i)$  = Geometric factor at  $E_i$

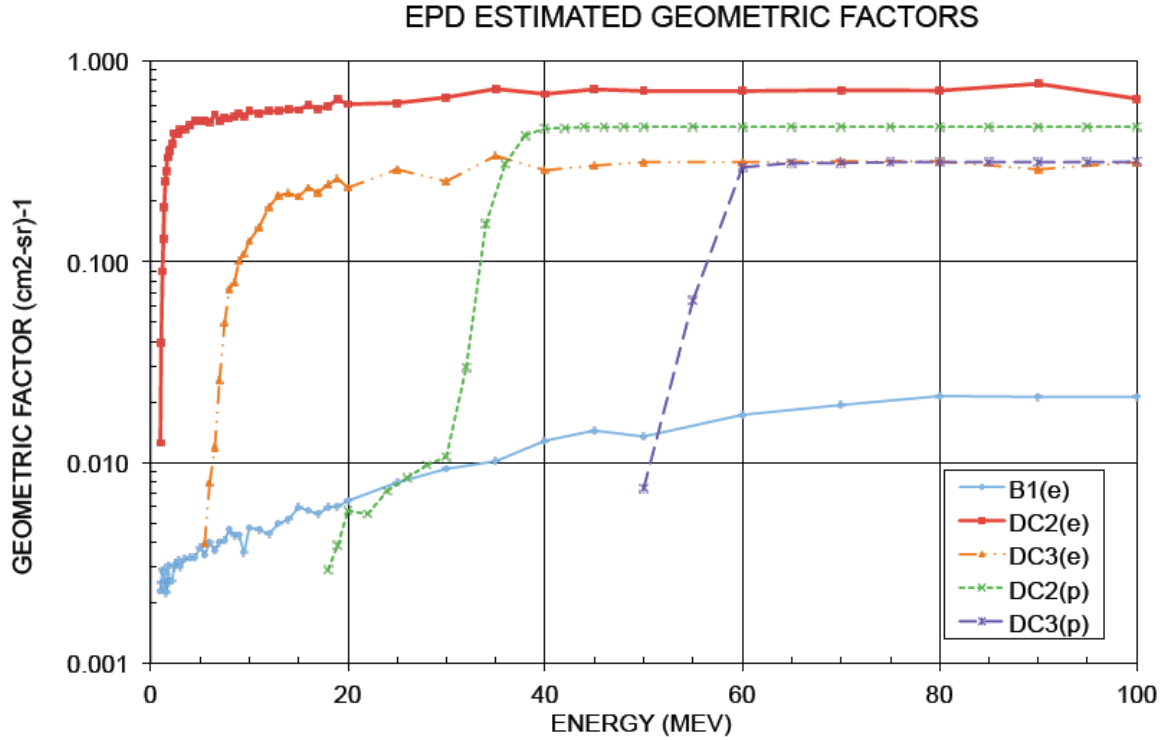


Fig. 3. Geometric factors estimated for the EPD B1, DC2, and DC3 channels. “p” stands for proton channels and “e” for electron channels. Note that B1(p) is 0.

**Table 3. Electron geometric factors in cm<sup>2</sup>-sr for the LEMMS high-energy channels.**

<b>Energy</b>	<b>Geometric Factor, cm<sup>2</sup>-sr (*)</b>		
MeV	B1	DC2	DC3
1.0	0.0043 (14%)	0.070 (3%)	
1.5	0.0058 (12%)	0.28 (2%)	
2.0	0.0067 (11%)	0.36 (1%)	
3.0	0.0073 (10%)	0.41 (1%)	
4.0	0.0080 (10%)	0.44 (1%)	
5.0	0.0079 (10%)	0.45 (1%)	0.00079 (32%)
6.0	0.0085 (10%)	0.45 (1%)	0.0077 (10%)
7.0	0.0092 (9%)	0.46 (1%)	0.038 (5%)
8.0	0.0094 (9%)	0.46 (1%)	0.080 (3%)
9.0	0.0093 (9%)	0.46 (1%)	0.12 (3%)
10.0	0.0097 (9%)	0.46 (1%)	0.15 (2%)
12.0	0.0096 (9%)	0.46 (1%)	0.20 (2%)
14.0	0.0099 (9%)	0.46 (1%)	0.22 (2%)
16.0	0.010 (9%)	0.46 (1%)	0.24 (2%)
18.0	0.010 (9%)	0.46 (1%)	0.26 (2%)
20.0	0.011 (9%)	0.46 (1%)	0.27 (2%)
25.0	0.011 (9%)	0.46 (1%)	0.29 (2%)
30.0	0.010 (9%)	0.46 (1%)	0.29 (2%)
35.0	0.010 (9%)	0.46 (1%)	0.29 (2%)
40.0	0.010 (9%)	0.46 (1%)	0.30 (2%)
45.0	0.010 (9%)	0.46 (1%)	0.30 (2%)
50.0	0.011 (9%)	0.45 (1%)	0.30 (2%)
60.0	0.011 (9%)	0.46 (1%)	0.31 (2%)
70.0	0.011 (9%)	0.45 (1%)	0.31 (2%)
80.0	0.011 (9%)	0.45 (1%)	0.31 (2%)
90.0	0.011 (9%)	0.45 (1%)	0.30 (2%)
100.0	0.011 (9%)	0.45 (1%)	0.31 (2%)

(\*) The numbers in parenthesis indicate the statistical uncertainties of the geometric factors.

**Table 4. Proton geometric factors in cm<sup>2</sup>-sr for the LEMMS high-energy channels.**

Energy MeV	Geometric Factor, cm <sup>2</sup> -sr (*)		
	B1	DC2	DC3
18.0		0.0028 (17%)	
20.0		0.0058 (12%)	
24.0		0.0072 (10%)	
28.0		0.0097 (9%)	
32.0		0.029 (5%)	
38.0		0.43 (1%)	
40.0		0.46 (1%)	
44.0		0.47 (1%)	
48.0		0.47 (1%)	
50.0		0.47 (1%)	0.0074 (10%)
55.0		0.47 (1%)	0.064 (4%)
60.0		0.47 (1%)	0.29 (2%)
65.0		0.47 (1%)	0.31 (2%)
70.0		0.47 (1%)	0.31 (2%)
80.0		0.47 (1%)	0.31 (2%)
90.0		0.47 (1%)	0.31 (2%)
100.0		0.47 (1%)	0.31 (2%)

(\*) The numbers in parenthesis indicate the statistical uncertainties of the geometric factors

Substitution of the geometric factors and  $J(E) \sim J_0 (E/E_0)^{-X}$  into Eq. 1 gives the count rate as a function of  $X$  and  $J_0$ . In particular, for  $J_0 = 1$ , the count rates for B1, DC2, and DC3 as functions of  $X$  are plotted in Fig. 4. The ratios [counts(DC3)/counts(B1)] and [counts(DC3)/counts(DC2)] are also readily estimated. The results for these two ratios versus  $X$  are plotted in Fig. 5. The curves in these two figures now allow one to estimate the original flux. That is, given the actual B1, DC2, and DC3 count rates, Figs. 4 and 5 can be interpolated to determine  $X$  and  $J_0$ . For example, to estimate the power  $X$  for each pair (e.g., [counts(DC3)/counts(B1)] and [counts(DC3)/counts(DC2)]), determine the relevant ratio and then interpolate in Fig. 5 to find the corresponding value of  $X$ . This was done computationally by using a fit to the curves in Fig. 5 so that  $X = F(\text{counts(DC3)/counts(B1)})$  or  $X = G(\text{counts(DC3)/counts(DC2)})$ . Once  $X$  has been estimated, that value can be used to interpolate for a given energy channel in Fig. 4 to find the count rate for  $J_0=1$  for that channel. The count rate from Fig. 4 divided into the actual count rate gives an estimate of  $J_0$ . That is, Fig. 4 can be used to derive a function  $H(X)$  of the form:

$$[\text{Count Rate from Fig. 4}]_i = H_i(X) \quad (2)$$

where  $i = \text{B1, DC2, or DC3}$

From this, the value of  $J_0$  is given by:

$$J_0 = [\text{Obs Count Rate}]_i / [\text{Count Rate from Fig. 4}]_i = [\text{Obs Count Rate}]_i / H_i(X) \quad (3)$$

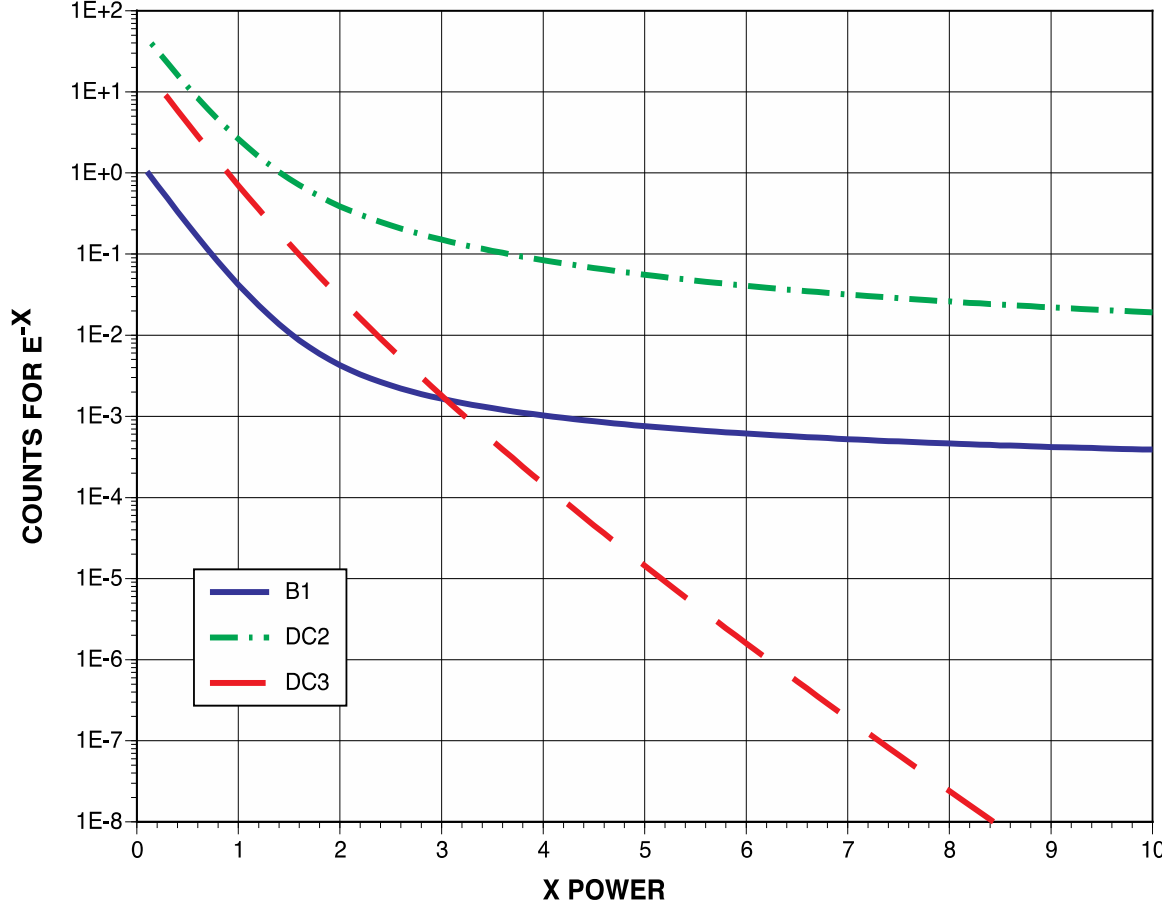


Fig. 4. Assuming EPD counts are given by Eq. 1 and  $J(E) = (E/E_0)^{-x}$  (i.e.,  $J_0 = 1$ ), the estimated count rates for B1, DC2, and DC3 are plotted versus the coefficient X.

Here, [Obs Count Rate] is the observed count rate for B1, DC2, or DC3. Note that this process gives two sets of estimates for  $J_0$  and X: one for the (B1,DC3) pair and another for the (DC2,DC3) pair. In summary, we now have the electron flux as a function of energy over the range  $E \sim 1\text{-}15$  MeV:

$$\frac{dI(E)}{dE} = J(E) = J_0 (E/E_0)^{-x} \quad (4)$$

where:

J and  $J_0$  are in units of  $(\text{cm}^2\text{-s-sr-MeV})^{-1}$

E is in MeV

$E_0$  is 1 MeV

X is determined from Fig. 5 and the count rate ratios

$J_0$  is determined from the actual count rate, X, and Fig. 4

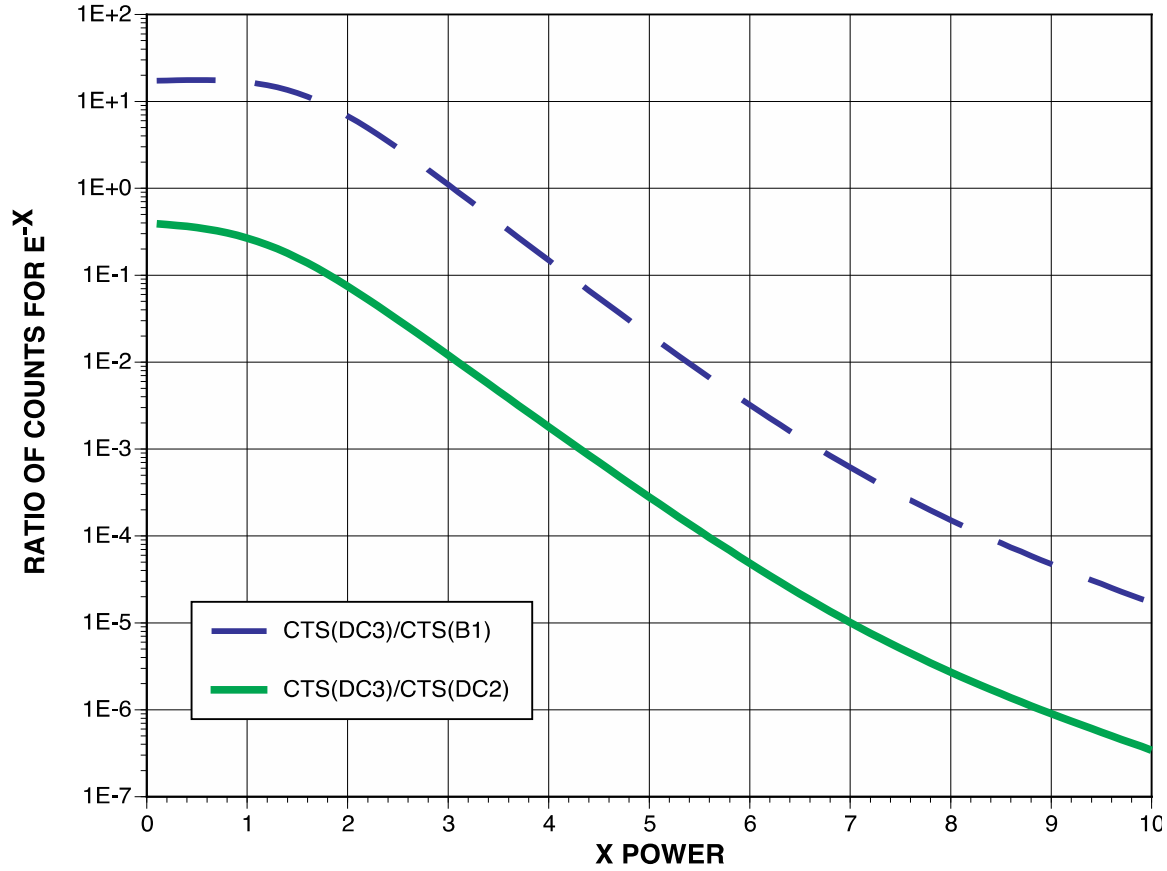


Fig. 5. Assuming EPD counts are given by Eq. 1 and  $J(E) = J_0 (E/E_0)^{-X}$ , the ratios  $[Cts(DC3)/Cts(B1)]$  and  $[Cts(DC3)/Cts(DC2)]$  are plotted vs. the coefficient  $X$ .

### GEOMETRIC FACTOR TO FLUX—F1, F2, AND F3

In addition to the high-energy electron channels B1, DC2, and DC3, the electron fluxes from ~174-884 MeV were estimated using the EPD F1, F2, and F3 channels. The energy ranges, average energies, and geometric factors (Lagg, 1998) are presented in Table 5. The latter are versus power  $X$  as in  $J(E) \sim J_0 (E/E_0)^{-X}$  as given in Eq. 4.

Table 5. The energy bands, average energies for those bands, and the estimated geometric factor-efficiency factor ( $GF'(X)$ ) for the corresponding energy spectra given by Eq. 4. These latter values were taken from Lagg (1998).

Channel	$E_{min}(KeV)$	$E_{max}(KeV)$	$E_{avg}(KeV)$	$GF'(cm^2-sr) \times 10^3$			
				X=0	X=1	X=3	X=5
<b>F1</b>	174	304	239	11.15	10.72	9.85	9.05
<b>F2</b>	304	527	416	15.44	15.48	15.52	15.53
<b>F3</b>	527	884	706	11.80	12.01	12.43	12.80

The F channel differential flux rates are then given by:

$$J(E_{AVG}) = \frac{cts/s}{(E_{\max} - E_{\min}) \cdot GF'(X)} \quad (5)$$

where:

- $J$  = Differential flux in  $(\text{cm}^2\text{-sr-s-KeV})^{-1}$
- $E_{avg}$  = Weighted average energy; here we assume  $E_{avg} = (E_{\max} + E_{\min})/2$
- $GF'$  = Product of the geometric factor and efficiency factor (see Lagg, 1998) weighted by the spectral index  $X$ . Here, for simplicity, we assume  $X \sim I$ .

### **DATA COMPARISONS**

In this section, the F-channels, B1, DC2, and D3 will be compared for internal consistency. Figures. 6, 7, and 8 compare DC2:B1, B1:DC3, and DC2:DC3. These data are taken directly from the original EPD Real Time counts, with the only manipulation being a dead time correction applied by APL. This can be used as the basis for checking subsequent operations on the data. The EPD Real Time data represent simple, on-board arithmetic averages (typically 5–10 minutes) over pitch angle that are relayed in near-real time back to the Earth.

The main feature of these plots is the striking relationship between DC2 and B1. Over a range of almost 5 orders of magnitude, the two count rates follow a nearly linear relationship where:

$$\text{Cts}(\text{DC2}) \sim 1.5 \times 10^2 \text{ Cts}(\text{B1}) \quad (6)$$

This close relationship is anticipated of course as the two channels have roughly the same energy cut-off—~1.5 MeV for B1 and ~2 MeV for DC2. (In passing, note that DC2 appears to be “quantized” for count rates of  $\sim 1.5 \times 10^6 \text{ s}^{-1}$  or higher—as will be discussed later, this is due to a dead time correction at the highest, saturated levels. Also note the presence of what is apparently a “noise level” for the B1 count rate below  $\sim 1 \text{ s}^{-1}$ .)

The raw count rate data, which are over somewhat arbitrary time intervals, were averaged over fixed 10-minute intervals to make comparisons with other Galileo data sets possible, and the results were “cleaned” by the removal of anomalous counts, extreme outliers, and periods when the B and DC channels were known to be out of calibration (e.g., the so-called “chicken mode,” in which the  $0^\circ$  end of the LEMMS took only occasional, brief forays out from the protection of a calibration shield). The count rate data for distances less than 20 R<sub>J</sub> (when Galileo was in the trapped radiation environment) for DC2 versus B1 averaged over equal 10 minute intervals are plotted in Fig. 9. The plot for the 10-minute intervals is nearly identical to Fig. 6 for count rates above  $10 \text{ s}^{-1}$  (B1) and  $1000 \text{ s}^{-1}$  (DC2) showing that the averaging had no effect on the database.



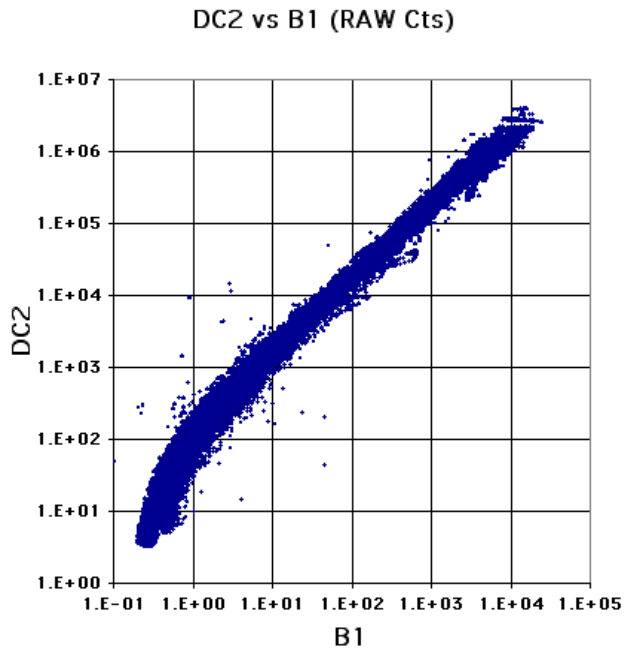


Fig. 6. DC2 raw count rates versus B1 raw count rates for the EPD (data are through Day 52, 2000).

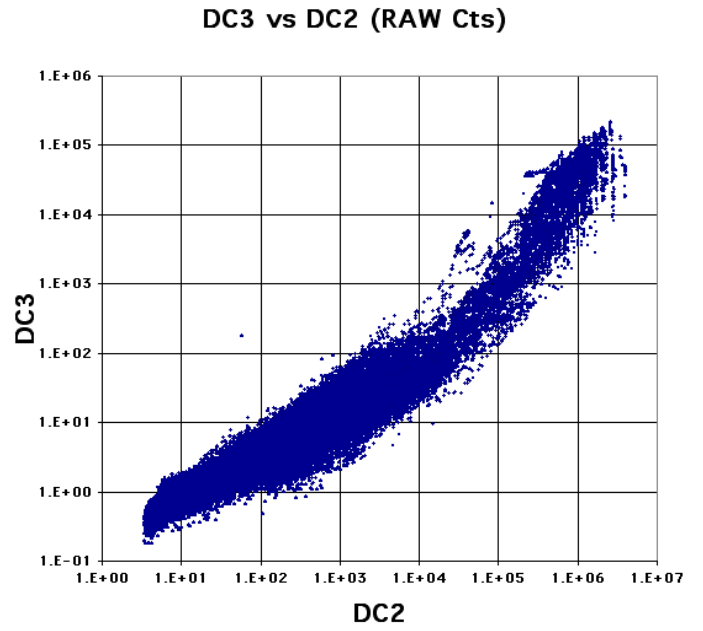


Fig. 8. DC3 raw count rates versus DC2 raw count rates for EPD.

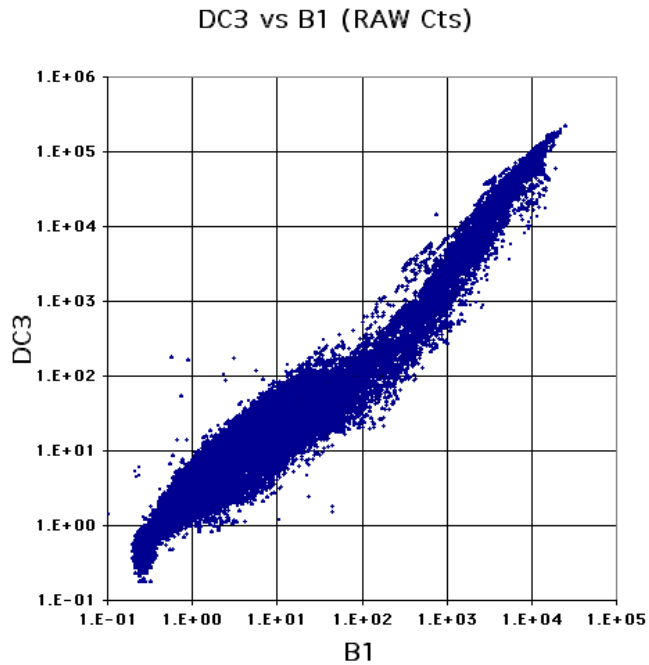


Fig. 7. DC3 raw counts versus B1 raw count rates for the EPD.

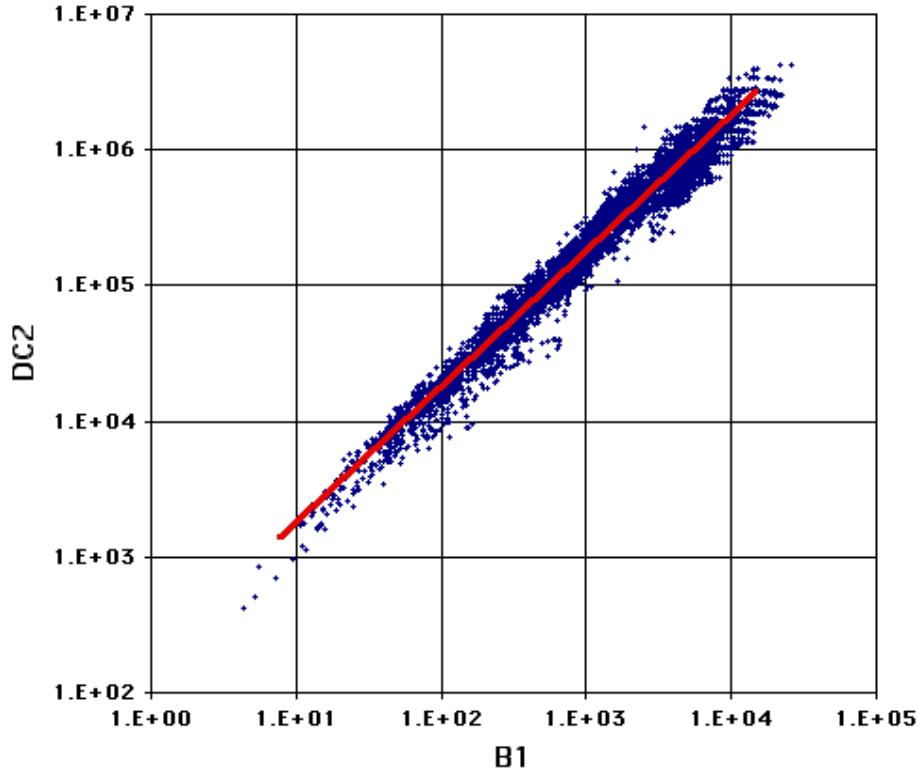


Fig. 9. “Clean” EPD raw counts per second for DC2 and B1 for 10-minute average intervals. (The line is for an index of 1.)

Given estimates of  $J_0$  and  $X$ , the next step in the data comparison process was to estimate the electron differential flux at 1 MeV as given by the two pairs of  $J_0$  and  $X$  values for each 10-minute average interval. Specifically, the  $J_0$  and  $X$  pairs determined for the 10-minute count rate pairs (B1,DC3) and (DC2,DC3) as described in the previous section were used to calculate:

$$J(1 \text{ MeV}) = J_0 (1/E_0)^{-X} \quad (7)$$

The differential flux values so determined are compared in Fig. 10.

The logs (base 10) of the differential fluxes at 1 MeV estimated by this process were then fit in the least square sense for the pairs (B1,DC2) and (DC2,B1). The results demonstrate that the proposed method of converting EPD high-energy electron counts to fluxes is at least self-consistent—the (B1,DC3) estimates of the flux at 1 MeV are within a factor of  $\sim 1.5$ -3 of the (DC2,DC3) flux estimates (as the B1 values are apparently at the detector noise floor below an equivalent flux of  $10^4$  at 1 MeV, the fits are only for  $B1 > 10^4$ ).

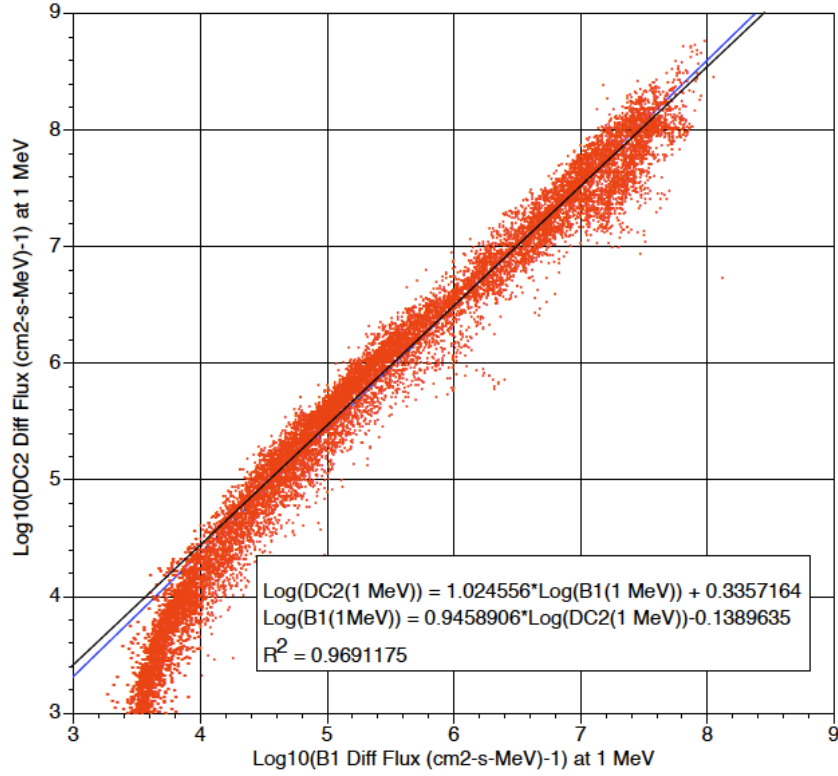


Fig. 10. The electron differential flux at 1 MeV estimated from the 10-minute count rate pairs (B1,DC3) and (DC2,DC3). Over the flux range of interest, the DC2 fluxes are approximately a factor of 1.5–3 times higher than the B1 fluxes at 1 MeV. (Note: The fits are only for  $B1 > 10^4$ .)

As another way of testing the B1 and DC2 flux estimates for consistency, the three lower energy EPD electron F channels (F1, F2, F3) were converted to differential fluxes using geometric factors in Table 5. (Note: These differ somewhat from the published curves in Williams et al., 1992, that were used in the original GIRE model.) The logs of these three flux estimates at the three different energies were then fit using a least squares method to  $J_0 (E/E_0)^{-x}$  for each 10 minute data interval. The resulting fits were extrapolated to 1 MeV and the estimates compared to the (B1,DC3) and (DC2,DC3) flux estimates. These are presented in Figs. 11 and 12 below. These plots imply that the B1 fluxes are roughly equal to the F fluxes over a range of 4 orders of magnitude. The DC2 fluxes are, by the same assumptions, about a factor of  $\sim 3$ – $3.5$  higher than the F channel predictions. Although there is no a priori reason to expect close agreement between extrapolations of the lower F channels to 1 MeV to the B1/DC2 channels, these results imply the DC2 flux estimates are proportionally higher at low energies than the F channel fluxes by a factor of  $\sim 3$  while the B1 and F channel estimates appear to be in agreement. Even so they all show the same trend/proportionality over a large range of fluxes, which implies reasonable consistency between the two very different counts to flux conversion methods.

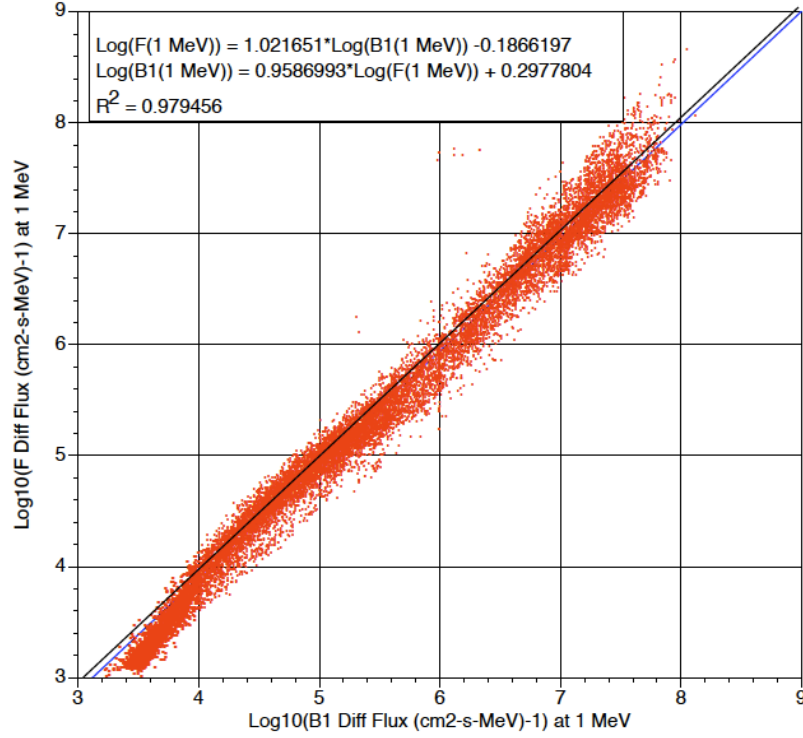


Fig. 11. The estimated fluxes at 1 MeV for fits to the (F1,F2,F3) EPD channels are compared with the fluxes predicted by the (B1,DC3) pair. (Note: The fits are only for  $B1 > 10^4$ .)

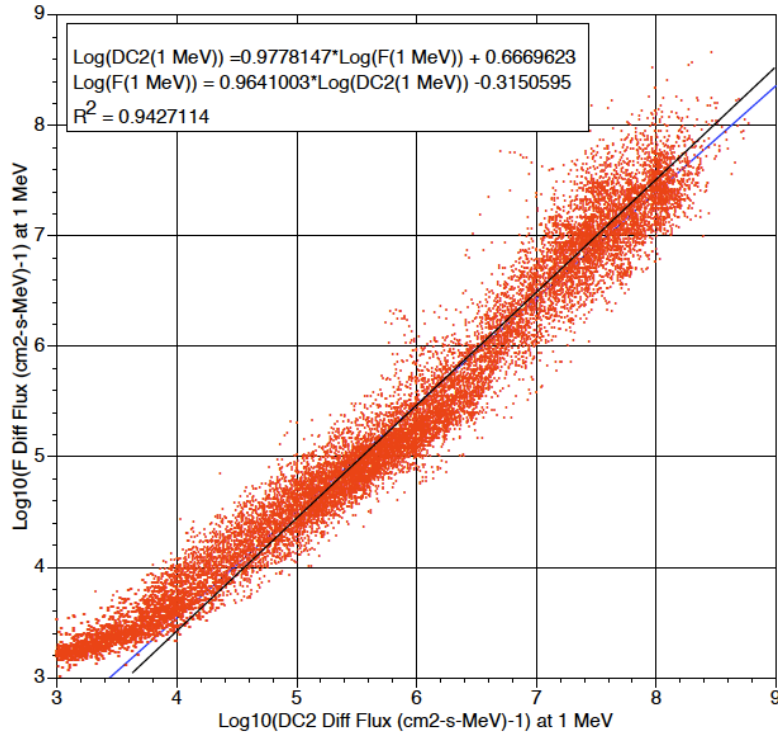


Fig. 12. The estimated fluxes at 1 MeV for fits to the (F1,F2,F3) EPD channels are compared with the fluxes predicted by the (DC2,DC3) pair. (Note: The fits are only for  $B1 > 10^4$ .)

### ***“REAL TIME” EPD DATA VERSUS “PLAYBACK” DATA***

As an independent test of the consistency of the raw data and to evaluate the method used to produce the EPD Real Time (low time resolution) data, the 10-minute average EPD counts can be compared with the corresponding high time resolution data taken in-situ (the so-called Playback or Record mode data). G. Clough (Garrett et al., 2003) worked with T. Armstrong (Fundamental Technologies and the University of Kansas) to study the particle pitch angle distribution as a function of L-shell. Intervals have been identified that give pitch angle distributions based on the Playback/Record Mode data for time periods unaffected by the jovian lunar flybys (the jovian moons perturb the plasma and field data in their immediate neighborhood in complex ways and thus these data are not included in this global jovian model). Several of those high time resolution intervals, as exemplified by Figs. 13 and 14, have been averaged over 10-minute intervals to give an estimate of the “omnidirectional” B1, DC2, and DC3 count rates equivalent to the Real Time data. For each selected channel (B1, DC2, DC3), averaged Playback/Record Mode data and time-adjacent points of Real Time data were compared across the transitions between the two modes. These data should be comparable unless the mode transition occurred in a region of large flux gradient.

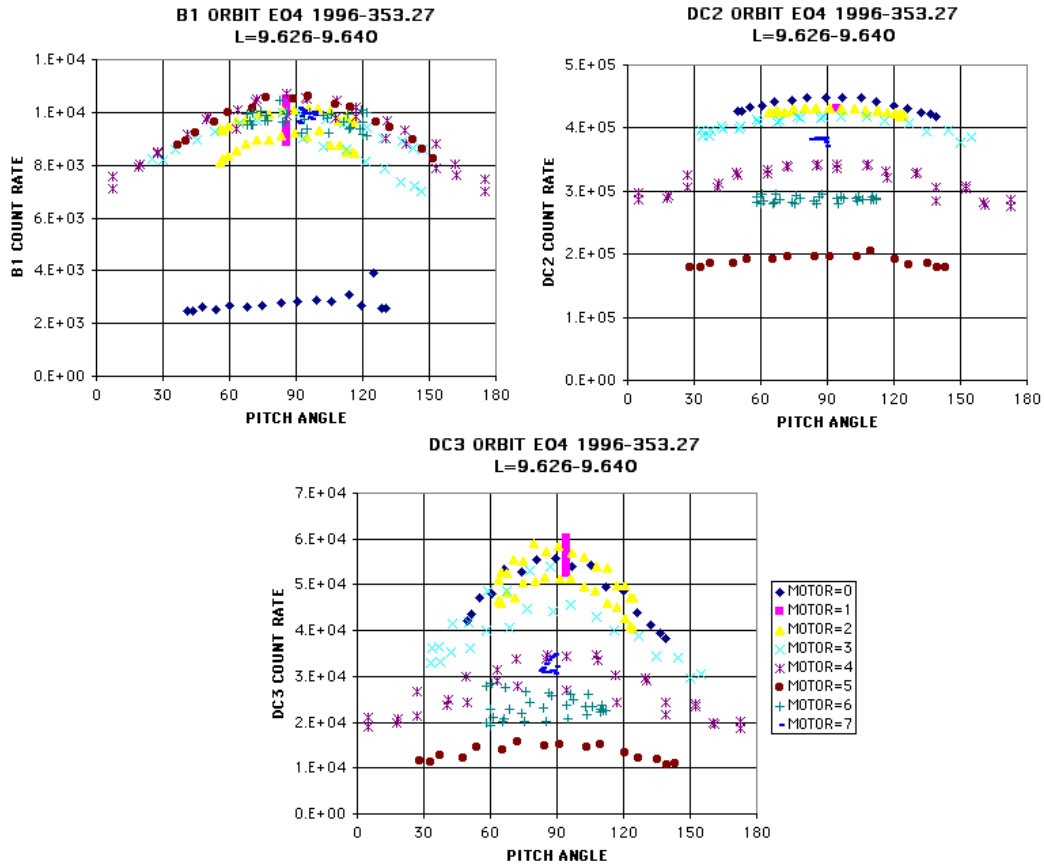


Fig. 13. Representative examples of the pitch angle distributions for B1, DC2, and DC3 for the Playback data. Note that the differences in motor position correspond to varying degrees of obscuration—the highest values at each position represent the unobscured data.

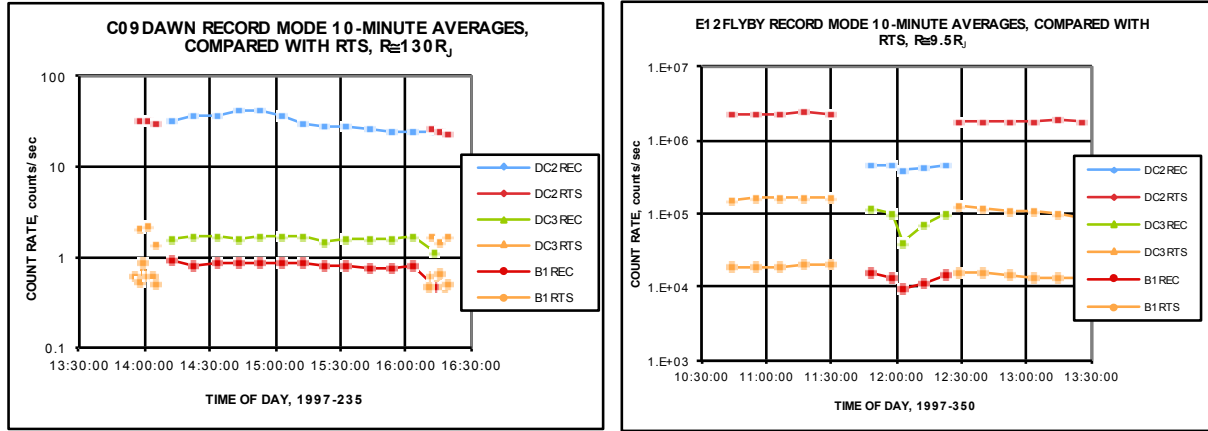


Fig. 14. Plots of EPD channels DC2, DC3, and B1 as functions of time for two Galileo orbits. Center segments in each plot are the 10-minute averaged Record Mode data, and side segments are adjacent Real Time data segments. Left plot data collected at  $R_J \approx 130$  and right plot at  $R_J \approx 9.5$ .

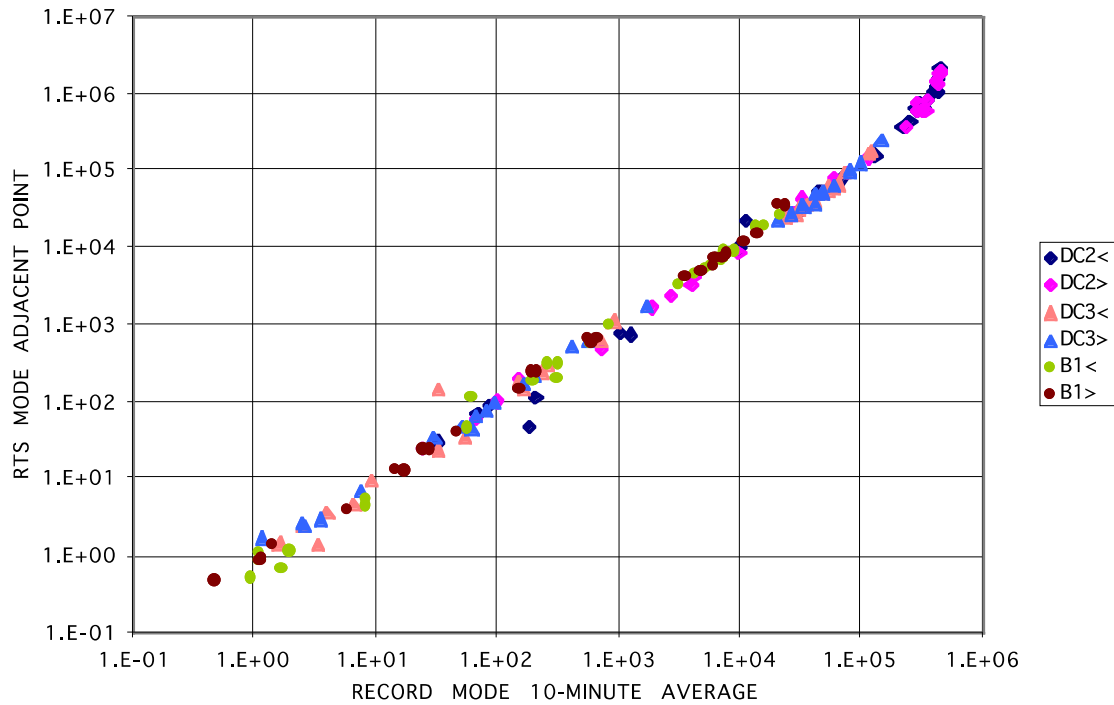


Fig. 15. Plot of Real Time data particle flux vs. 10-minute averaged Record Mode data at adjacent point. Legends identified “<” are points across transitions from Real Time to Record Mode. Legends identified “>” are across transitions from Record Mode to Real Time. The upward curve at high flux rates suggests an uncorrected dead time effect in the Record Mode data.

Plots (Fig. 15) of the Real Time and the estimates produced by averaging the Record Mode/Playback angular data (for the un-obscured motor positions) over 10-minute intervals show little scatter around a straight line and indicate a 1:1 correlation between the two count rate

data modes over a range from  $\sim 1 \text{ s}^{-1}$  to nearly  $10^5 \text{ s}^{-1}$ . Above  $\sim 10^5 \text{ s}^{-1}$ , the observed count rates for the averaged Record Mode data are systematically and progressively lower than for the Real Time data, a situation that can be corrected by applying a non-extendable dead time correction to the Record Mode data. The dead time constant required is near  $1.6 \mu\text{sec}$ , the value suggested by JHU/APL for the DC channels. (The count rates for channel B1 are so low that a dead time correction is irrelevant to the results.) This observation confirms that the Real Time data supplied to JPL by JHU/APL have already had a dead time correction made to them, while the Record Mode data received through FT/KU/PDS did not have the factor applied. The details of the averaging process and the dead time correction factor will be reviewed below.

### ***AVERAGING PROCESS***

Record Mode data available from the Galileo EPD are typically in blocks of about 1 to 2 hours in length, occasionally longer, and normally occur during fly-bys of the moons. Starting at the beginning “time stamp” for each block, data were read over successive 10-minute intervals. Because the spacecraft spin period is close to 20 seconds and the spin was divided into 16 “sectors” for data-collection purposes, the number of records available for averaging in each 10-minute window was nominally 480. It was occasionally smaller due to gaps in the data, and always smaller in the last window because the data ran out before 10 minutes had elapsed. The smallest number of records read in the last window was 14. The time assigned to each 10-minute average was the time at the center of the 10-minute window, even though this meant that for the last window the assigned time could be later than the time of the last data point.

Within each 10-minute window, only the count rate data from a subset of motor positions (look directions) were used to form the omnidirectional average. The subset varied with EPD channel. In all cases, data values of  $-1.0$  (bad data flag) or  $0$  were ignored (while  $0$  can be a valid number, the files in some cases contain blocks of zeros which are not plausibly valid data). For channel B1, all other count rates were averaged except for Motor Position  $0$  data, because the  $0^\circ$  end of the LEMMS EPD instrument is then pointing at the foreground shield. For channels DC2 and DC3, only count rates for Motor Positions  $0$ ,  $1$ , and  $2$ , were included because those are the only positions where the  $180^\circ$  end of the LEMMS EPD instrument is not partially or entirely blocked by various spacecraft structures. With these criteria, the number of values actually averaged for DC2 and DC3 was nearly always the same, and roughly  $1/3$  to  $1/2$  of the B1 value in most cases. 30 blocks of Record Mode data were identified for averaging. Some Galileo orbits had none, most had one or two, and orbit C09 had five. In a few cases, adjacent Real Time data existed only on one side of a block of Record Mode data.

### ***DISPLAY OF DATA ACROSS MODE CHANGES***

Real Time data taken approximately one hour before and after each Record Mode segment were extracted from the files obtained from JHU/APL. These data were merged with the averaged Record Mode data (which had not yet been corrected for detector dead time effects) and plotted as a function of time. Fig. 14 presents two of these plots. The plot of data obtained at a large radial distance from Jupiter, where count rates are low, shows no evidence of a “dead time” problem. The data obtained at  $9.5 \text{ R}_j$  shows the significant effect on DC2 counts of the dead time correction.

### **COMPARISON OF DATA MODES**

From all the plots like those of Fig. 14, the adjacent pairs of points across the mode change gaps were identified, and each Real Time data count rate was plotted as a function of the adjacent Record Mode count rate. This plot is presented as Fig. 15. Note that for count rates below  $\sim 10^5 \text{ s}^{-1}$ , the plot is nearly a straight line of slope 1, while above that point it curves upward, showing a decreased Record Mode count rate due to the absence of detector system dead time effects.

The dead time constant for the DC channels published by JHU/APL is  $\tau = 1.6 \text{ } \mu\text{sec}$ . Table 6 presents all the relevant detector dead time constants provided by JHU/APL. The EPD channels are best modeled as having a non-extendable dead time, for which the actual count rate should be computed from the observed count rate as follows:

$$\text{RATE}_{\text{ACTUAL}} = \text{RATE}_{\text{OBSERVED}} / (1 - \text{RATE}_{\text{OBSERVED}} * \tau) \quad (8)$$

Fig. 16 shows the results of this correction for the data plotted in Fig. 15. Note that the line of points now agree over the whole observational range. The small clump of points near the top is not different from other clumps seen along the line.

It should be noted that the dead-time correction provided by Eq. 8 is only an approximation in a system that involves coincidence detection. T. Choo (Personal Communication, 2002) has advised that the correct method replaces the observed rate in the denominator of Eq. 8 with the appropriate single-detector or sum-of-channels count rate from Table 6. For example, the D-single-count rate should be used to perform the dead-time correction for channel DC2. These more exact dead-time corrections have been applied to all of the data used for model construction.

**Table 6. Table of EPD detector dead time constants for the energetic electron study, provided by T. H. Choo at JHU/APL.**

<b>Channels</b>	<b>Time Constants</b>	<b>Comments</b>
E2	-	$R_{\text{obs}}$ vs. $R_{\text{act}}$ correction is done using a pileup-up simulation table to reverse out the 'real rate.' Channels used in the simulation are E0, E1, E2, E3, EB1
F1, F2, F3	1.2 $\mu\text{sec}$	Sum of F channels ( $0.5 * F0 + F1 + F2 + F3 + FB1 + FB2$ )
B0, B1, B2	1.2 $\mu\text{sec}$	B Single omni channels
DC0, DC2	1.6 $\mu\text{sec}$	D Single calibration position
DC1, DC3	1.6 $\mu\text{sec}$	C Single calibration position



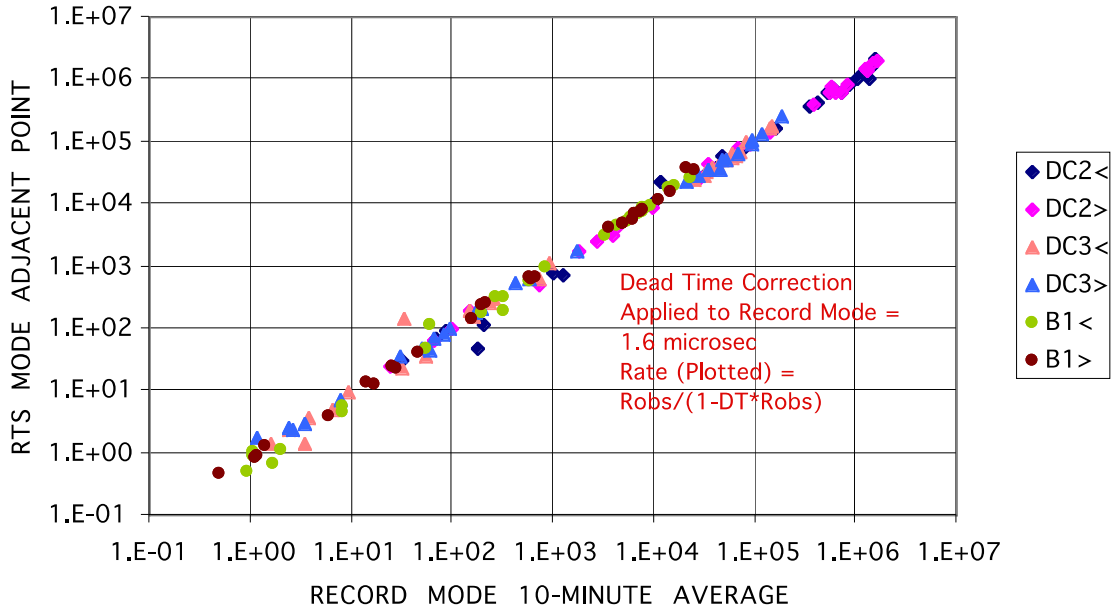


Fig. 16. Data of Figure 15 replotted following a dead time correction to the Record Mode data, assuming a non-extendable dead time of 1.6  $\mu$ sec.

This comparison between the Record Mode data and the Real Time data returned by the Galileo EPD demonstrates the methods used by APL to estimate Real Time count rates observed on Galileo and proves that the Real Time data, as made available to JPL by JHU/APL, have already been corrected for detector dead time in the DC channels. The Record Mode data made available by FT/KU/PDS were not. (This correction is to be applied to future versions.) Applying such a correction to the Record Mode data brings the two sets into the coincidence that one would expect if neither or both had received such a correction.

### ***ESTIMATING THE 31 MEV ELECTRON FLUX***

The highest Galileo EPD electron channel is DC3 which is an integral channel for  $E > 11$  MeV. Unfortunately, at the high flux levels observed at Jupiter, electrons with energies greater than 20 to 100 MeV are important in dose calculations. To extend the GIRE2 model to greater energies, we have made use of the  $E > 21$  MeV and  $E > 31$  MeV Geiger Tube Telescope (GTT) channels on Pioneer 10 and 11 (Van Allen et al., 1974, 1975; Van Allen, 1976; Baker and Van Allen, 1977). These two integral channels were converted into a differential channel at 31 MeV by assuming a simple power law such that:

$$I(E) = A_0 E^{B_0} \quad (9)$$

which implies

$$i(E) = -\frac{dI(E)}{dE} = -A_0 B_0 E^{B_0-1} \quad (10)$$

Given the integral fluxes  $I(21)$  and  $I(31)$  at 21 and 31 MeV from the Pioneer GTT:

$$B_0 = \frac{\log_{10}\left(\frac{I(31)}{I(21)}\right)}{\log_{10}\left(\frac{31}{21}\right)} \quad (11)$$

and

$$A_0 = \frac{I(21)}{21^{B_0}} \quad (12)$$

where:

$I(E)$  = Integral electron flux at energy  $E$

$i(E)$  = Differential electron flux at energy  $E$

$A_0, B_0$  = Constants (Eq. 9)

Using this approximation, the Pioneer 10 and 11 differential flux estimates are plotted in Figs. 17 and 18.

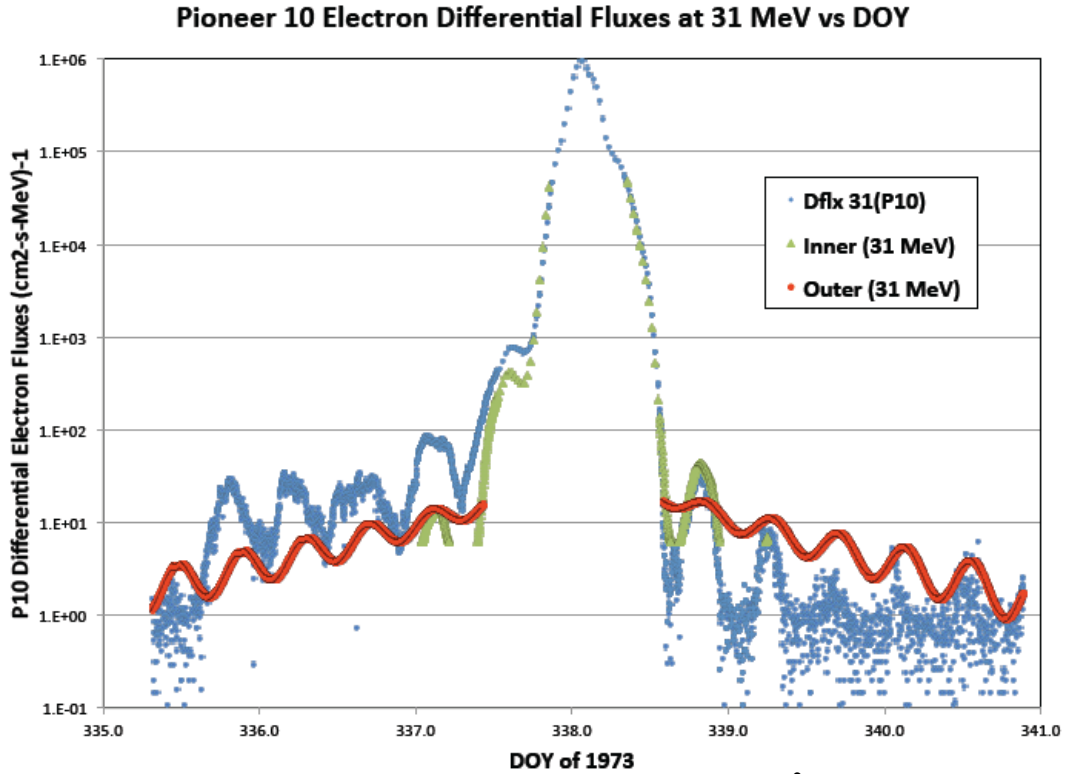


Fig. 17. Pioneer 10 differential fluxes (in units of electrons/cm<sup>2</sup>-s-MeV) for Jupiter closest approach on Day 338, 1973. GTT data are from the Planetary Data System.

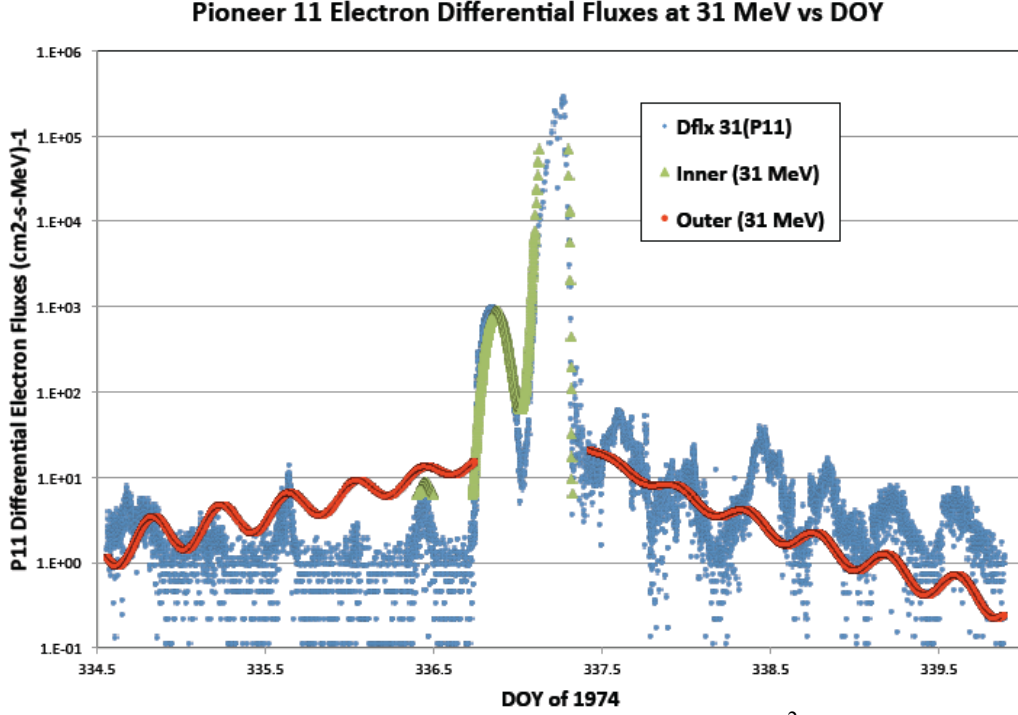


Fig. 18. Pioneer 11 differential fluxes (in units of electrons/cm<sup>2</sup>-s-MeV) for Jupiter closest approach on Day 337, 1974. GTT data are from the Planetary Data System.

The division of the jovian magnetosphere into inner and outer regions is very pronounced in Figs. 17 and 18. The Pioneer data also demonstrate a strong asymmetry in local time for the outer region. Here, the inner region differential fluxes at 31 MeV between  $L \sim 7.5$  and  $\sim 25$  were fit in terms of  $L$  to the following equation (note the absence of a pitch angle distribution function):

$$\log_{10}(i(31)) = -4.85300E-08 L^6 + 8.14264E-06 L^5 - 5.34188E-04 L^4 + 1.70288E-02 L^3 - 2.60446E-01 L^2 + 1.41317E+00 L + 3.16329E+00 \quad (13)$$

The outer region 31 MeV differential fluxes for Pioneer 10 and 11 were fit in terms of  $R$  (the radial distance in  $R_J$  to the observation point) between  $\sim 15$  to  $50 R_J$  and of  $Z_{\text{map}}$ , the distance from the plasma sheet for  $|Z_{\text{map}}| < 12 R_J$  by the following ( $Z_{\text{map}}$  is provided by the Khurana magnetic field model and will be defined later):

$$i(31) = 12 e^{-|Z_{\text{map}}|/12.5} \frac{e^{-0.055 R}}{e^{-0.055 \cdot 25}} \quad (14)$$

These fits are plotted in Figs. 17 and 18 as the green (inner) and red (outer) points. While the inner region is obviously a very good fit, the apparent asymmetries due to local time in the outer region are not as well represented, and a “median” fit has been assumed. This issue is currently under investigation, and we hope to resolve it in futures studies.

### ***DATA CONSISTENCY—COMPARISONS WITH PIONEER AND VOYAGER***

Given the estimates of the electron flux for the individual EPD channels and the Pioneer 31 MeV channel, it is possible to construct a “best fit” spectrum for each 10-minute data interval. This is accomplished by first determining “best estimates” of the electron fluxes at 6 fixed energies: 0.239, 0.416, 0.706, 1.5, 2.0, and 11.0 MeV. (These correspond approximately to the F1, F2, F3, B1, DC2, and DC3 low-energy cutoffs.) The F channel differential fluxes were determined using geometric factors provided by JHU/APL (see Table 5, Lagg, 1998) and then fitting a power law to the log of the 3 flux estimates as discussed. The B1 and DC2 differential fluxes were determined as outlined previously by using the (B1,DC3) and (DC2,DC3) data pairs. The DC3 differential flux was estimated as the geometric mean of the DC3 estimate from these pairs. To increase coverage to higher energy, a seventh energy channel was also included in the analysis based on the Pioneer 10 and 11 electron differential fluxes at 31 MeV as given by Eqs. 13 and 14 for each time interval. It should be noted that there is no a priori reason to expect agreement between the Pioneer data and the Galileo data as the data sets were taken roughly 20 years apart. Even so, inclusion of the 31 MeV data in the fitting process is believed to give a better model than if there were no data at that energy—at the least it lends credence to extrapolations into the 20–50 MeV energy range. The differential flux values at the 7 energies in each 10-minute interval were then fit using linear regression methods (see Garrett et al., 2011, for details of the fitting process) to an energy spectrum of the form:

$$F(E) = J_0 E^{-A} \left(1 + \frac{E}{E_0}\right)^{-B} \quad (15)$$

where:

$F$  = Omni-directional differential electron flux as a function of  $E$

$E$  = Electron energy (MeV)

$J_0$  = Constant (roughly the differential flux at  $E = 1$  MeV)

$A$  = Constant (approximately the power law index for the low-energy component)

$B$  = Constant ( $A + B$  is approximately the power law index for the high-energy component)

$E_0$  = Constant (approximately the breakpoint energy between low- and high-energy spectra)

A representative data set and spectral fit is presented in Fig. 19. Given the fitted differential energy spectrum, EPD estimates of the 10-minute jovian fluxes can now be compared with similar model estimates from the Pioneer 10 and 11 and Voyager 1 and 2 missions. The data from these four spacecraft were summarized in terms of a model of the jovian radiation belts developed by N. Divine (Divine and Garrett, 1983). Figs. 20 and 21 compare the EPD differential flux estimates at energies of 1.5 MeV and 11 MeV (roughly the B1 and DC3 channels) with the Divine Model at the same spatial positions as functions of distance ( $R$ ) from Jupiter. For the 1.5-MeV energy in Fig. 20, the flux estimates vary from a factor of 1 between 8–9  $R_J$ , to ~4 between 9–12  $R_J$ , and to ~2 between 12–16  $R_J$ . For the 11 MeV energy channel in Figure 21, the two flux estimates are in good agreement over the entire range. It is encouraging that the Galileo and Pioneer/Voyager 11 MeV data are in good agreement over this range as it suggests the high-energy electron population is about as stable over 20-year time periods as it is over the 7-year span of Galileo's data.

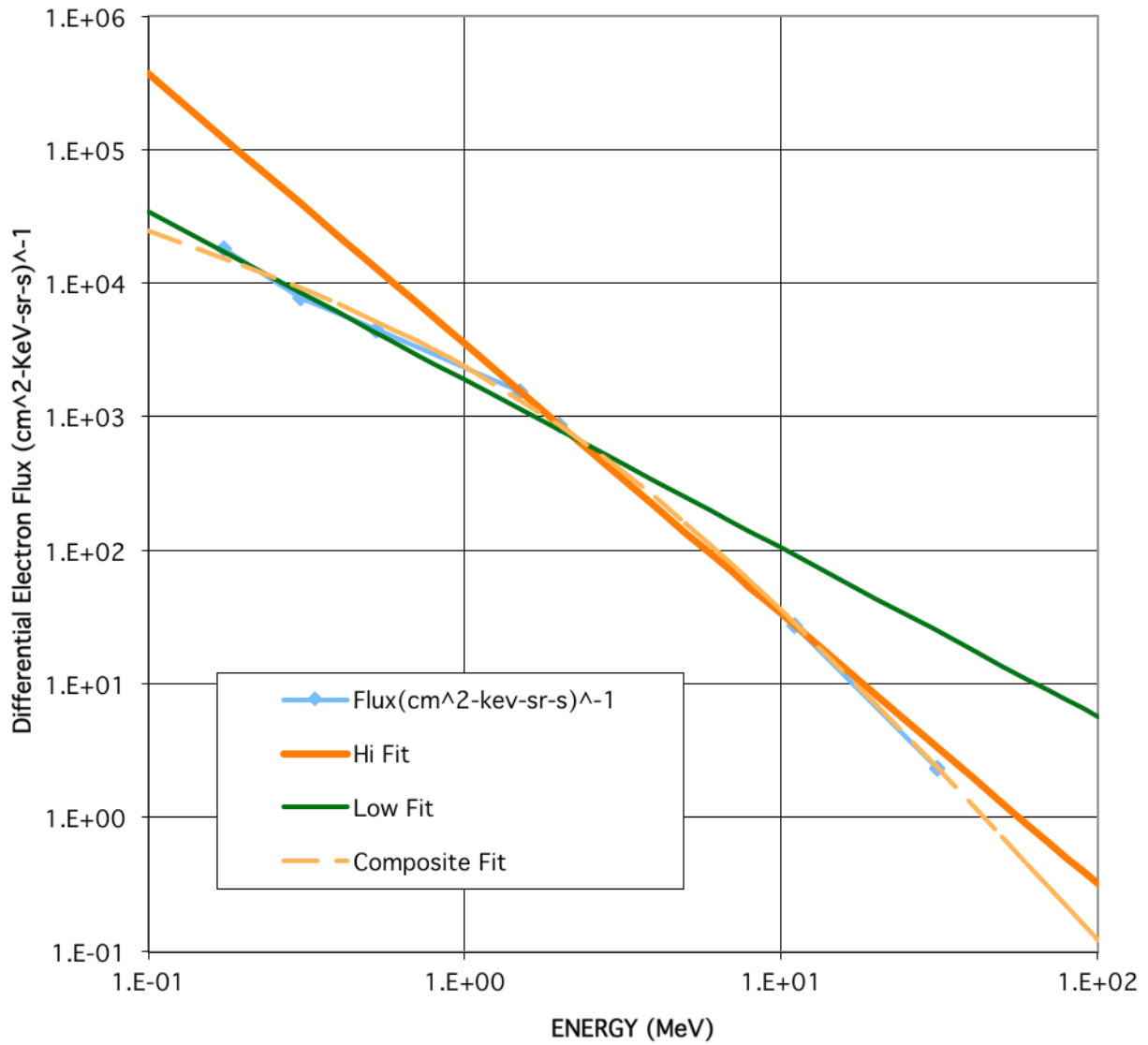


Fig. 19. Fits to a representative EPD differential flux spectrum. The 7 diamonds correspond to the best-case EPD flux estimates at 0.239, 0.416, 0.706, 1.5, 2.0, 11.0, and 31.0 MeV. (The 31 MeV value is from Pioneer 10 and 11.) “Composite Fit” corresponds to a functional fit to these 7 flux estimates using Eq. 15.

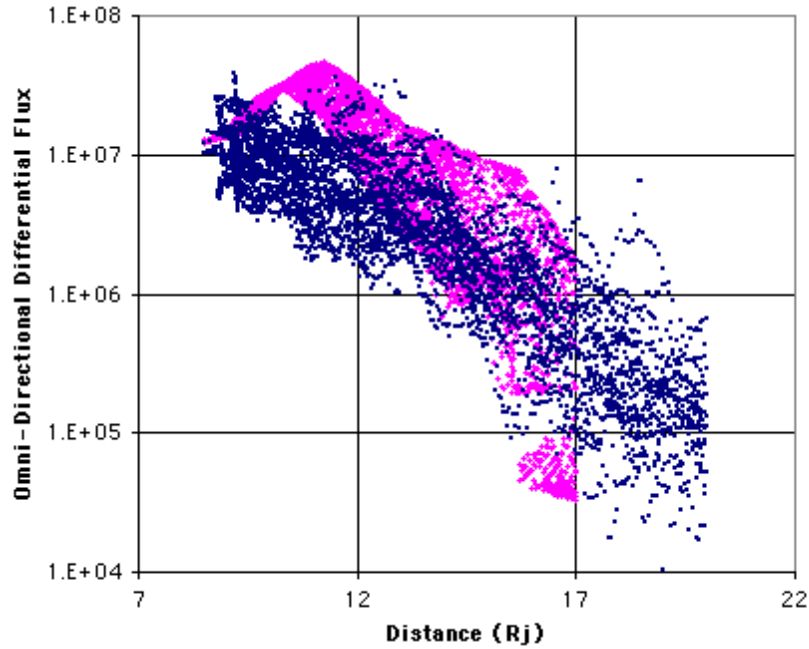


Fig. 20. Estimates of the omnidirectional differential electron flux (particles/(cm<sup>2</sup>-s-sr-MeV) versus distance from Jupiter (R<sub>J</sub>) at 1.5 MeV. Dark blue points correspond to the EPD estimated fluxes for the Galileo 10-minute averages. The lavender crosses correspond to the equivalent Pioneer/Voyager (i.e., Divine Model) estimates for the same spatial locations.

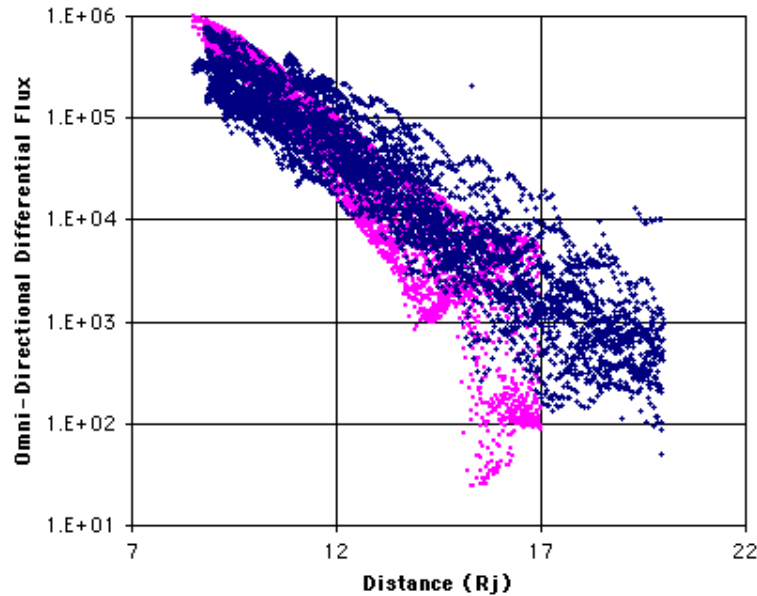


Fig. 21. Estimates of the omnidirectional differential electron flux (particles/(cm<sup>2</sup>-s-sr-MeV) versus distance from Jupiter (R<sub>J</sub>) at 11 MeV. Dark blue crosses correspond to the EPD estimated fluxes for the Galileo 10-minute averages. The lavender points correspond to the equivalent Pioneer/Voyager (i.e., Divine Model) estimates for the same spatial locations.

### ***DATA CONSISTENCY—SUMMARY***

To summarize, the geometric factors for the EPD B1, DC2, and DC3 electron channels have been estimated by Jun et al. (2002). Geometric factors for the lower energy F1, F2, and F3 channels were provided by T. Choo at JHU/APL (and updated as discussed). Based on these factors, estimates of the electron differential flux at energies corresponding to 0.239, 0.416, 0.706, 1.5, 2.0, and 11.0 MeV were developed. Several consistency checks were made of the data to determine their validity. Specific tests were made to determine the flux at 1 MeV by various methods. Results indicate agreement for the data pairs (B1,DC3) and (DC2,DC3) at 1 MeV to a factor of 2–3 or better with the DC2 values being higher. In cross comparisons between the Real Time and Playback/Record Mode data to verify the Galileo on-board processing, B1 and DC3 Real Time count rates were found to be consistent with simple averaging of the Playback/Record Mode data (provided a dead time correction is applied to high count rates)—this implies that the spacecraft on-board algorithms were consistent. The source of the 2–3 uncertainty factor in the DC2/B1 ratio is unclear, however. Although it is tempting to attribute it to a problem in the DC2 (as opposed to B1 as it appears to agree with the F channel predictions at 1 MeV) geometric factor, ultimately there is no way to verify this. Finally, the 7 years of EPD flux estimates appear to be consistent with the Pioneer and Voyager flux estimates taken over 20 years earlier in the 8–17 R<sub>J</sub> range through comparisons with the predictions of the Divine Pioneer/Voyager-based model (Figs. 20 and 21). Overall, there is good agreement between the various means of computing electron differential fluxes that form the basis of the GIRE2 model.

### ***DEVELOPING AN INNER ZONE OMNIDIRECTIONAL, EQUATORIAL MODEL***

The previous sections have outlined the steps necessary to convert the raw EPD count rates to particle fluxes and spectra over the range ~0.5 to ~30 MeV. Although some uncertainty remains in the results, the electron spectra thus estimated appear to be reasonable and consistent with previous flybys (e.g., Pioneers and Voyagers) for the trapped electron environment between 8 and 17 R<sub>J</sub>. The next step, to be detailed in this section, is to convert the EPD data into a model of the jovian inner radiation environment that can be applied to other missions. This will be accomplished by first summing the EPD count rate data in radial bins (instrument counts can be directly summed as this is equivalent to extending the time period of the observation) and then averaging them over time to give average count rates as functions of position. The resulting count rates are then converted into estimates of the differential electron spectra as described earlier for each radial bin. The results of this process will be presented in the following sections for the inner, trapped radiation zone. The FORTRAN codes used to accomplish the fitting are listed in Garrett et al. (2011).

As discussed, the EPD count rate data are to be averaged as functions of distance from Jupiter for the F1, F2, F3, B1, DC2, and DC3 channels. The two systems typically used for organizing the environmental data around Jupiter are either System III (west longitude, latitude, and radial distance fixed relative to Jupiter's spin axis) or the so-called magnetic B and L system, which is relative to the jovian magnetic field axis. To first order, as in the case of the Earth, it is assumed that the trapped radiation environment is symmetric longitudinally—indeed this is a major assumption in the B and L coordinate system. Given this assumption, the count rate data

are plotted by orbits in Figs. 22 and 23 versus radial distance in  $R_J$  and in L-shell for orbits G02 through I33. Although the two figures are similar, use of the L-shell parameter significantly improves on the ordering of the data, smoothing out the radial “ripples” in Fig. 22. In fact, except for apparent “storm” in Orbit C22 (and perhaps E06 and E16), the count rate data are remarkably ordered, the log of the count rate varying very nearly linearly with L from 8 to about 15. This ordering in L is not unexpected as the radiation belts are controlled and ordered by the jovian magnetic field.

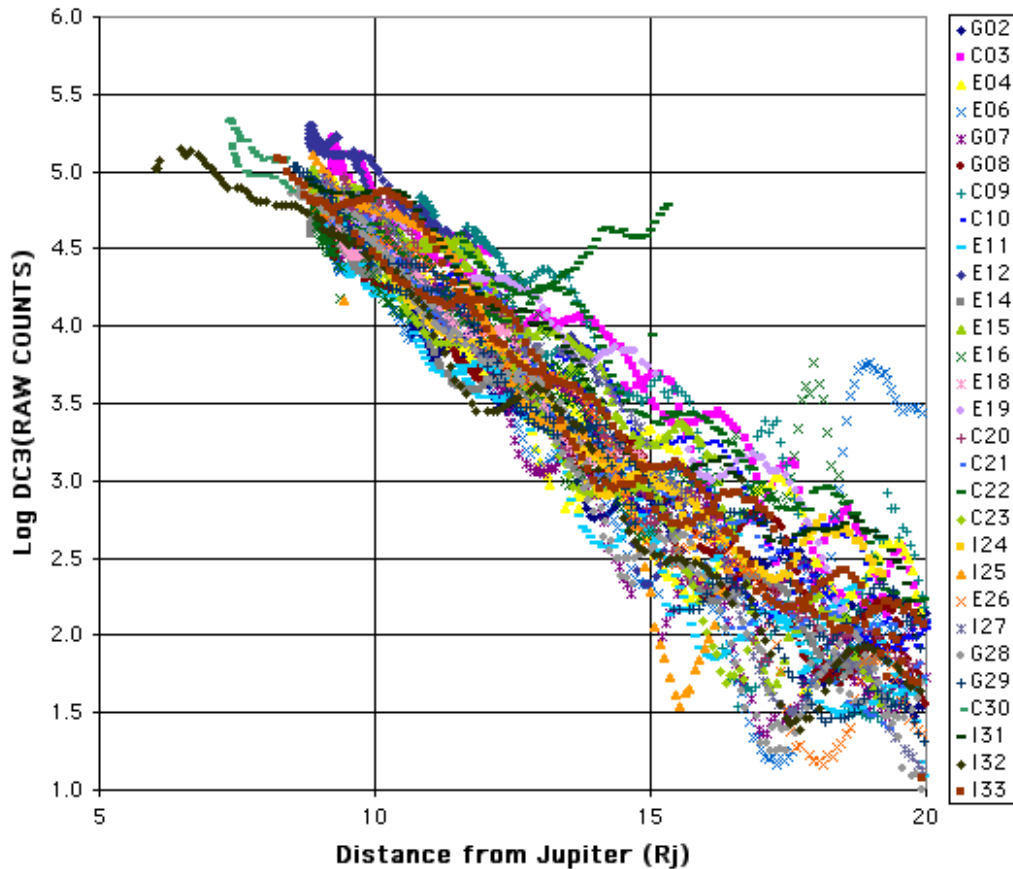


Fig. 22. DC3 counts versus distance from Jupiter in units of  $R_J$  for individual Galileo orbits G02 to I33. Note the radial oscillations in each orbit.

The jovian magnetic field is offset from the planet’s spin axis by about  $11^\circ$ . As Jupiter rotates in  $\sim 10$  hours, the particle fluxes at a fixed position in space will vary up and down every 5 hours in the equatorial plane as the radiation belts move over it—this behavior is seen in Fig. 22. B and L coordinates, however, are fixed to the magnetic field and, as is readily apparent in Fig. 23, the oscillating motion of the particle fluxes is almost entirely removed by plotting the data in terms of L-shell. Galileo does not venture more than  $10^\circ$  to  $20^\circ$  from the magnetic equator for most of its mission, so one might expect a fairly small variation with B (corresponding to a change in latitude along a fixed L-shell). However, the great extent to which the data are ordered only by the L parameter is actually rather surprising, and suggests that the jovian radiation flux has only a small variation with pitch angle near the jovian magnetic equator over this radial range.



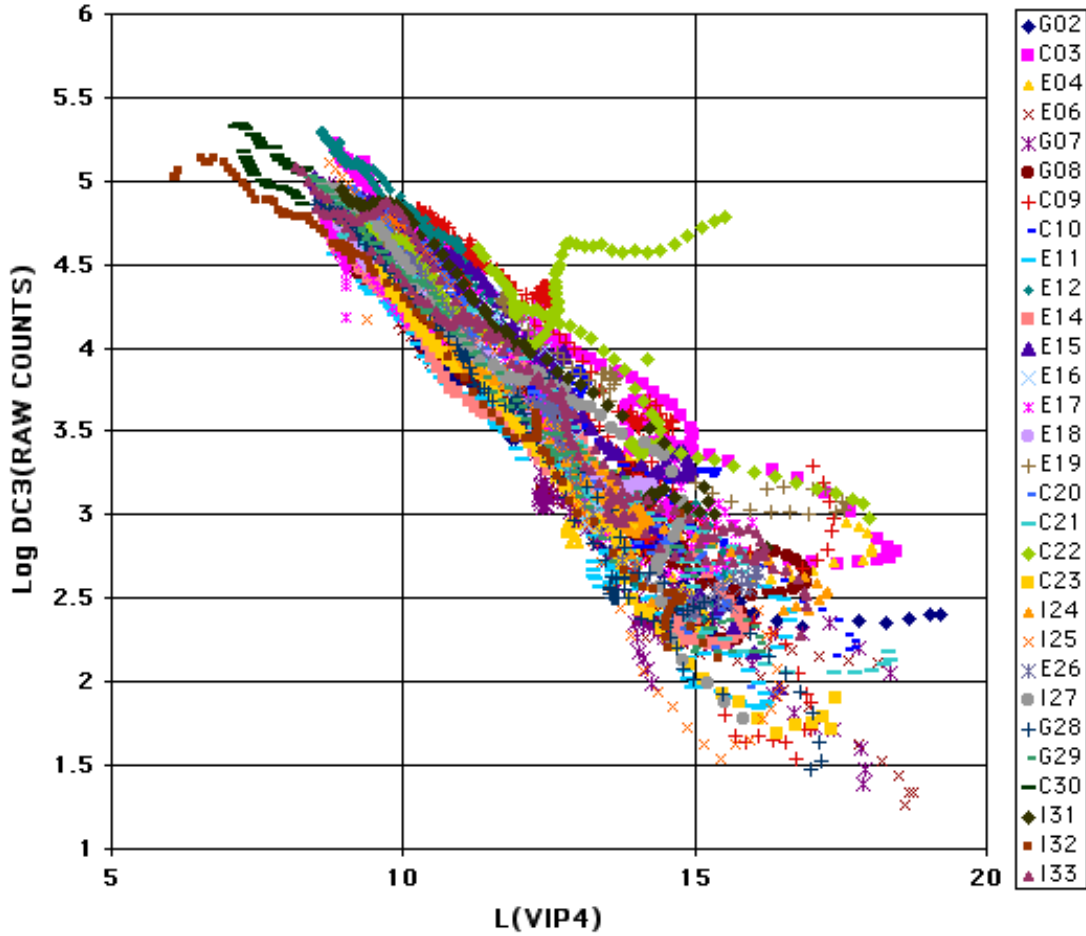


Fig. 23. DC3 counts versus L-shell for Galileo orbits G02 to I33.

Given that the Galileo inner zone high-energy electron data are well ordered in terms of L-shell alone, the first step was to average the count rate data at each of the 6 energies in L-shell bins. *In contrast to the original GIRE model, only intervals associated with magnetic equatorial crossings (as provided by K. Khurana) were analyzed.* The count rate averages are presented in Fig. 24 for each 1.5 L-shell range from 8 to 38. In this figure, all available orbits (though only for data along the magnetic equator) were included in the average.

As discussed in the previous section, a seventh electron channel at higher energies was added. This channel at 31 MeV was derived from fits to the Pioneer 10 and 11 data (*Van Allen et al.*, 1974, 1975). These flux variations are represented by Eq. 13 for the inner zone (here arbitrarily extended out to  $\sim 38$  L). The 6 EPD flux values (after converting to differential fluxes as discussed) and the Pioneer fluxes form an electron spectrum for each 1.5 L-shell interval. Each differential flux spectrum was then fit to give values of  $J_0$ , A, B, and  $E_0$  corresponding to Eq. 15. These values are listed in Table 7. This table and Eq. 15 constitute the GIRE2 average model of the electron omnidirectional differential flux along the jovian magnetic equator for energies from  $\sim 0.5$  to  $\sim 30$  MeV. Values at intermediate L-shells to those listed in Table 7 are derived by first determining the flux at the desired energy at the two L values which bracket the

desired L value and then linearly interpolating between the logarithms (base 10) of these flux values.

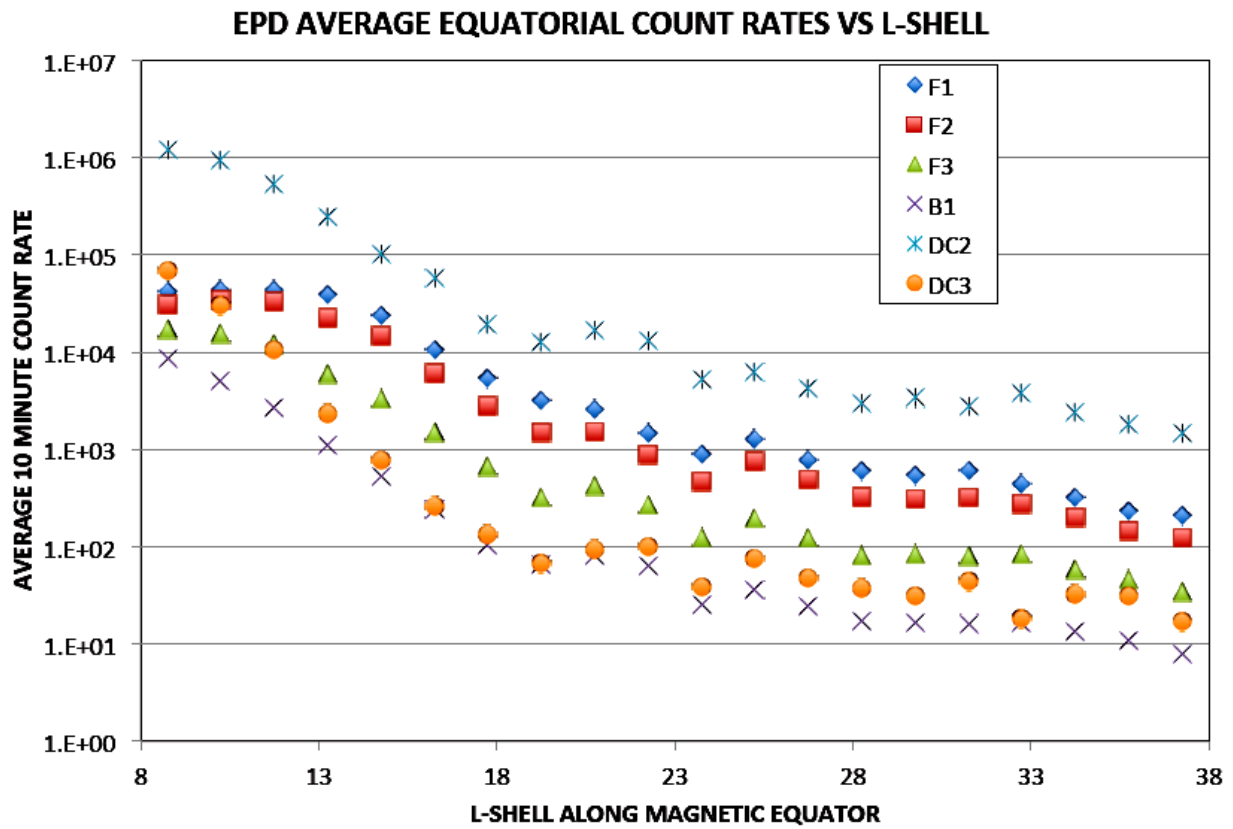


Fig. 24. Averages of the 10-minute EPD count rate data along the magnetic equator in discrete 1.5 L-shell bins.

**Table 7. Fitted electron differential flux parameters corresponding to Eq. 15. Units are  $(\text{cm}^2\text{-s-sr-keV})^{-1}$ . The model results produce an omni-directional flux.**

L(VIP4)	$J_0$	A	B	$E_0$
8.75	3.06E+03	1.52E+00	1.76E+00	1.03E+01
10.25	3.77E+03	1.44E+00	2.16E+00	4.68E+00
11.75	3.01E+03	1.62E+00	2.19E+00	3.67E+00
13.25	8.80E+02	2.36E+00	2.17E+01	2.37E+02
14.75	4.82E+02	2.47E+00	3.51E+00	2.59E+01
16.25	2.57E+02	2.33E+00	2.46E+00	9.70E+00
17.75	8.65E+01	2.61E+00	9.10E+00	1.18E+02
19.25	4.12E+01	2.83E+00	9.02E+06	2.22E+08
20.75	8.72E+01	2.08E+00	2.85E+00	7.58E+00
22.25	5.93E+01	1.92E+00	3.64E+00	1.07E+01
23.75	1.81E+01	2.45E+00	1.14E+01	1.50E+02
25.25	2.72E+01	2.41E+00	1.29E+02	1.49E+03
26.75	1.75E+01	2.40E+00	6.79E+00	7.72E+01
28.25	9.24E+10	1.39E+00	1.39E+00	6.36E-08
29.75	1.21E+01	2.38E+00	4.63E+00	5.42E+01
31.25	1.01E+16	-6.52E+00	9.48E+00	2.72E-02
32.75	1.70E+01	2.05E+00	1.89E+00	4.52E+00
34.25	8.97E+00	2.21E+00	7.00E+00	6.42E+01
35.75	7.36E+00	2.10E+00	4.23E+00	2.90E+01
37.25	5.10E+00	2.32E+00	1.33E+01	1.74E+02

The differential fluxes predicted at various energies versus equatorial L-shell value are compared with the original GIRE predictions in Fig. 25. Note that the original GIRE model only extended from  $\sim 8$  to 16 L. The new model was extended out to 38 L so that it can be compared with the outer model in a later section. The higher flux values for energies below  $\sim 1$  MeV are the result of changes in the F-channels' geometric factors discussed earlier. The good agreement between the GIRE and GIRE2 models in the 1–10 MeV range implies, even though the new model was limited to only values near the magnetic equator while the GIRE model was averaged over all data, the inner Galileo environment is well represented by an assumption of omni-directionality.

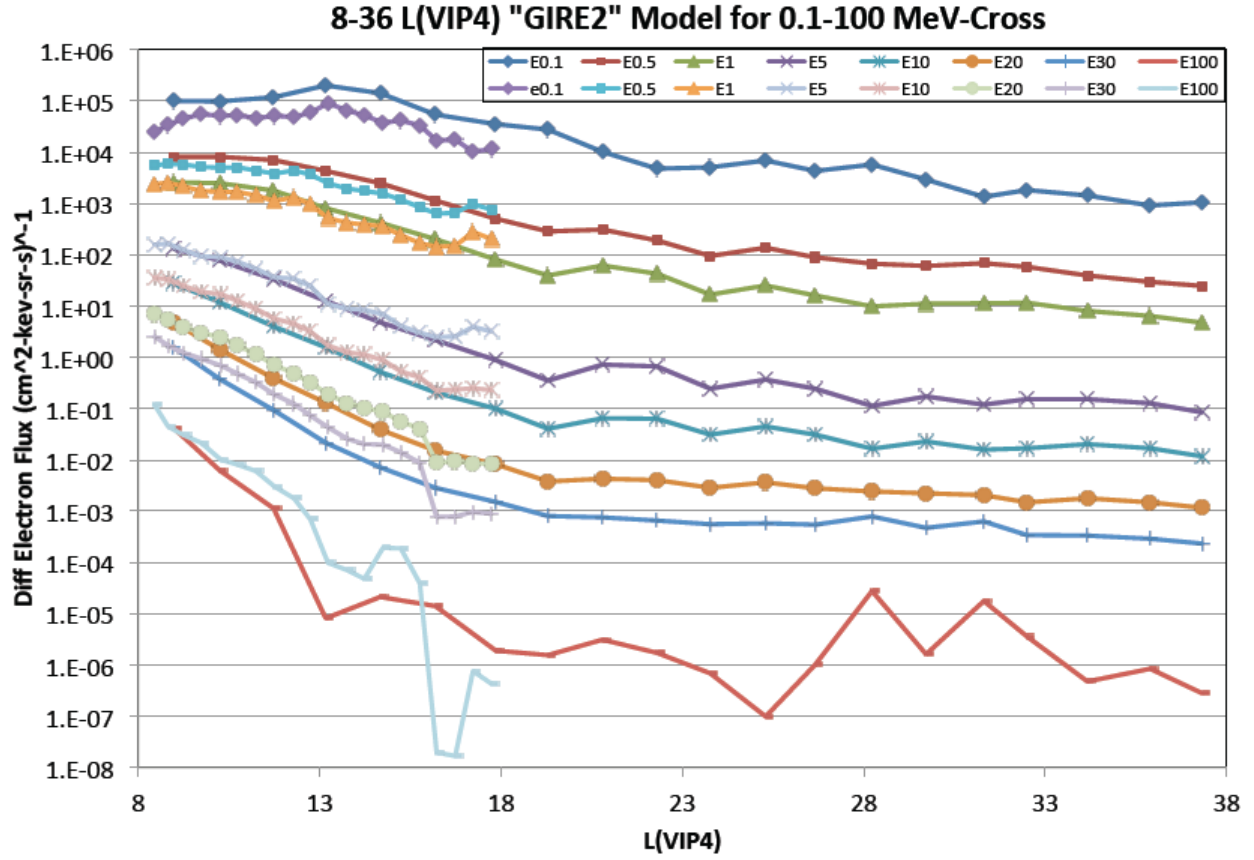


Fig. 25. Line plots of the differential electron fluxes as predicted by the inner region GIRE and GIRE2 models.

### ***DEVELOPING AN OUTER ZONE OMNI-DIRECTIONAL MODEL***

The GIRE2 model is split into two distinct sections (inner and outer) because the magnetic field structure, which governs charged particle dynamics, is intrinsically different. The inner jovian magnetosphere is dipole-like, while the outer region is essentially sheet-like. Within a planetary magnetic dipole, charged electron motion can be simplified to guiding-center bounce and drift. However, in a sheet structure, the scale size of particle gyroradii and gradients within the magnetic field, as well as boundary conditions, can become important.

The outer portion of GIRE2 is based on the premise that the structure of the outer jovian magnetosphere is essentially a thin current sheet. The center of the current sheet is defined as the location where the radial magnetic field component vanishes, with an antiparallel field on either side of the sheet. Fig. 26 shows a simplified Harris current sheet structure with oppositely pointing magnetic lines of force and a zero field in between. As the magnetic field goes to zero, the magnetic moment of a charged particle tends to infinity. Physically, the gyroradius of a charged particle becomes large with respect to the scale size of the magnetic field.

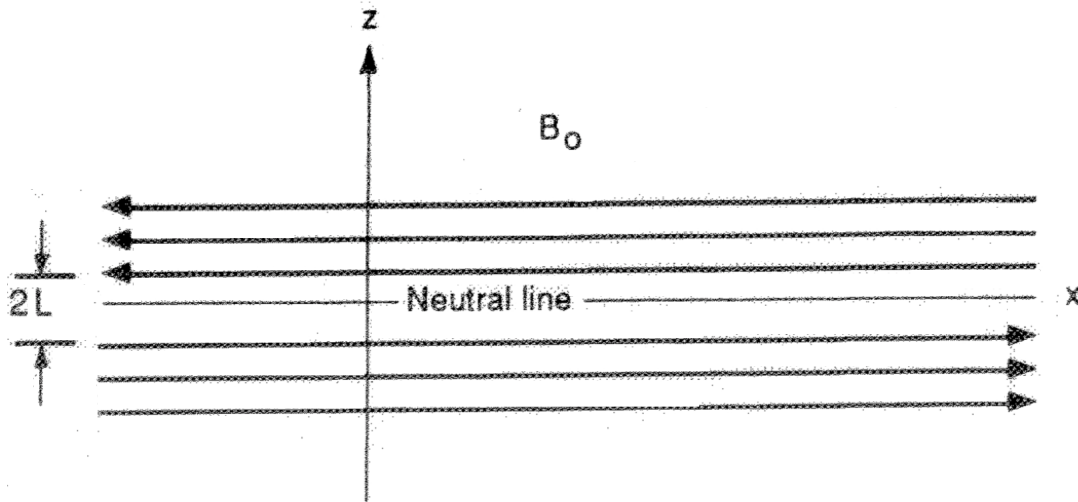


Fig. 26. Schematic diagram of an ideal Harris Current sheet. The magnetic field  $B_0$  is equal and opposite on either side of  $Z_{map}=0$ . The field strength reduces from  $B_0$  and  $Z_{map}=\pm L$  to zero at the neutral line. The scale  $L$  in this figure is unrelated to the McIlwain  $L$  parameter. [From Parks, 1991]

The transition between a dipole-like structure near Jupiter and a sheet in the outer section is often gradual, leaving an ambiguous region connecting the two. A report by Kokorowski (2010) shows that the inner edge of this transition region begins at  $\sim 15 R_J$  in the jovian equator. In reality, the topology of the outer region is that of a severely stretched dipole and not a strict current sheet within  $60 R_J$ , where GIRE2 is applicable. However, to a first approximation, a sheet structure was found to be sufficient. Fig. 27 shows modeled magnetic field line traces using two jovian magnetic field models, VIP4 and Khurana.

Like the inner portion, the outer portion of GIRE2 is azimuthally symmetric. The assumed symmetry is primarily a function of simplicity of the model and does not necessarily accurately reflect the fundamental controlling physics as was evidenced in the Pioneer 10 and 11 data analyzed earlier. Modifying the model to include outer region asymmetry is both interesting scientifically and potentially important for specific missions that need greater fidelity in outer zone radiation estimates but will not be studied in this update of GIRE.

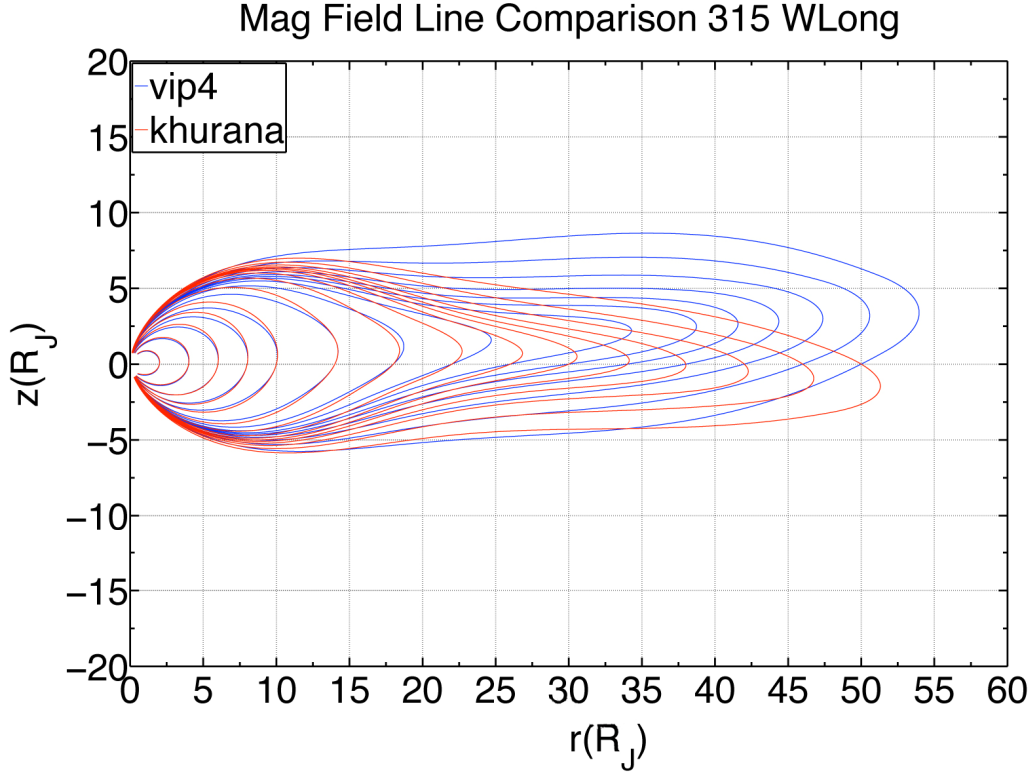


Fig. 27. Magnetic field line traces at 315° W longitude using the VIP4 (blue) and Khurana (red) models. Each trace begins at  $z=0$  in SIII coordinates. Traces should be interpreted qualitatively because of a slight skew in the longitudinal projection. [From Figure 3 in Kokorowski, 2010]

The range of applicability of the outer portion of GIRE2 spans the region from  $\sim 15 R_J$  at the inner edge to  $\sim 60 R_J$  at the outer edge. The inner edge depends greatly on the time-dependent position of the transition region. According to Kokorowski (2010), inside of  $15 R_J$ , the dipole-like structure of Jupiter's magnetic field has been observed to be relatively constant. Therefore, the inner portion of GIRE2 plasma sheet is expected to be more accurate. The outer edge of applicability for GIRE2 is largely dependent on the dayside magnetopause location. Models developed based on empirical spacecraft data suggest the noon magnetopause standoff distance is  $\sim 50$ - $100 R_J$  (Joy et al., 2002), while the inner edge of the magnetosheath can be as close as  $35 R_J$  (Khurana, 1997). As a result of the Galileo spacecraft's orbital pattern, the majority of the outer zone energetic electron data was recorded in the dawn, night, and dusk sectors. There is little data from the noon sector. Therefore, the azimuthal symmetry of the outer portion of GIRE2 more accurately reflects local times other than the noon sector. Caution should be used for radiation estimations made for spacecraft that spend a significant amount of time in the outer-zone at noon local time.

### ***SPICE***

For the outer portion of GIRE2, the SPICE system, produced and maintained by the Navigation and Ancillary Information Facility (NAIF) (NAIF, 2011), was used to determine the orbital elements for the Galileo spacecraft. The purpose of SPICE, as described on the NAIF

website, is ‘to assist scientists in planning and interpreting scientific observations from space-based instruments.’ For this project, SPICE was primarily used as a coordinate transformation tool. A detailed description of the complete SPICE tools can be found on the NAIF website.

### JOVIAN MAGNETIC FIELD MODEL

Jupiter has a strong magnetic field with a dipole moment offset from the center of Jupiter by  $\sim 0.1 R_J$  and tilted  $\sim 11^\circ$  with respect to the rotational axis [Smith et al., 1976]. The rotation period of Jupiter is slightly less than 10 hours, meaning that Galileo (as it is typically very close to the jovian equatorial plane) sees the magnetic equator wobble with a  $\sim 5$ -hour periodicity. The primary jovian coordinate system used to define spacecraft position is System-III (SIII) which is an inertial reference frame fixed to Jupiter. It is also useful for describing the inner dipole-like magnetosphere because the time-dependent wobble of the magnetic field can be expressed as a tilt in the magnetic equator with respect to the rotational equator. The outer magnetosphere, however, is dominated by the jovian plasma disk or current sheet. To describe this region from  $\sim 15 R_J$  outwards, GIRE2 uses the Khurana magnetic field model (Khurana, 1997) to define a coordinate  $Z_{map}$ . This is the normal distance away from the current sheet (see Fig. 28) to the observation point. The Khurana model includes a strong internal dipole moment and external sources that warp the dipole (to explain the current sheet) such that the total magnetic field is given by:

$$\vec{B} = \vec{B}_i + \vec{B}_e \quad (16)$$

where:

$\vec{B}_i$  = Internal magnetic field components  
 $\vec{B}_e$  = External magnetic field

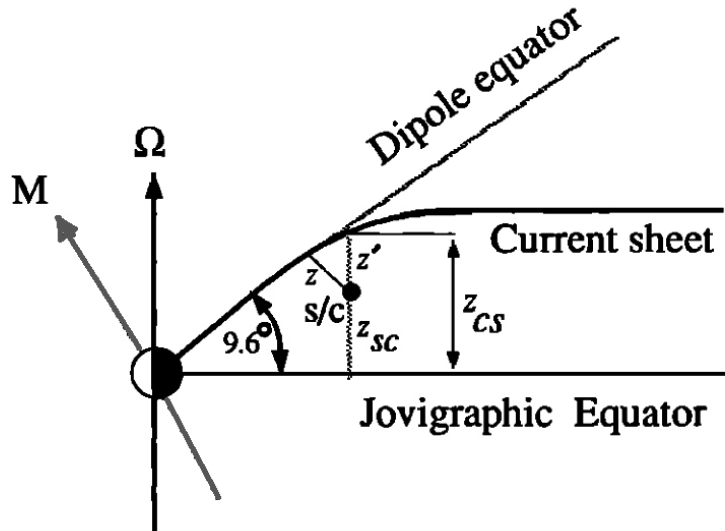


Fig. 28. A schematic diagram that includes the normal distance between the current sheet and a given location of interest. The line labeled  $Z$  is what we are calling  $Z_{map}$  in this report to emphasize that it is in the direction normal to the current sheet. [From Khurana, 1992]

If the internal field were represented by a pure dipole, then

$$\vec{B}_i = \frac{k_0}{r^3} (2 \cos \theta \hat{r} + \sin \theta \hat{\theta}) \quad (Gauss) \quad (17)$$

where:

$k_0$  = Magnetic dipole moment

$r$  = Distance from the center of the dipole

The Khurana model does not use a simple dipole for the internal field component, but rather includes a more complex scalar gradient description,

$$\vec{B}_i = -\nabla V \quad (18)$$

where  $V$  is defined by the sum of spherical harmonics.

$$V = R \sum_{l=1}^L \left( \frac{R}{r} \right)^{l+1} \sum_{m=0}^l P_l^m(\cos \theta) \{ g_l^m \cos(m\phi) + h_l^m \sin(m\phi) \} \quad (19)$$

Although Khurana (1997) stated that the  $O_6$  model coefficients from Connerney (1992) were the basis of his model, the version of the Khurana model used in this analysis (Drive\_KT\_2003\_sub.f) contains the identical set of coefficients as the VIP4 model (Connerney, 1998). The VIP4 Schmidt coefficients are listed in Table 8.



**Table 8.** Spherical harmonic Schmidt coefficients used in VIP4 and Khurana models for the internal component of the magnetic field. The Khurana (1997) model uses the  $O_6$  model coefficients. However, the most up-to-date version of the Khurana model (used in this analysis) contains coefficients identical to those used in the VIP4 model.

Schmidt Coefficient	VIP4/ Khurana 2003
$g_1^0$	4.205
$g_1^1$	-0.659
$h_1^1$	0.250
$g_2^0$	-0.51
$g_2^1$	-0.619
$g_2^2$	0.497
$h_2^1$	-0.361
$h_2^2$	0.053
$g_3^0$	-0.016
$g_3^1$	-0.520
$g_3^2$	0.244
$g_3^3$	-0.176
$h_3^1$	-0.088
$h_3^2$	0.08
$h_3^3$	-0.316
$g_4^0$	-0.168
$g_4^1$	0.222
$g_4^2$	-0.061
$g_4^3$	-0.202
$g_4^4$	0.066
$h_4^1$	0.076
$h_4^2$	0.404
$h_4^3$	-0.166
$h_4^4$	0.039

The Khurana model allows for additional terms to be included in the external component of the magnetic field by taking a combined approach of using a spherical harmonic formulation of the internal field and an Euler potential formulation for the external field. From Stern (1970, 1976) a divergence free magnetic field can be expressed in terms of two scalar functions (Euler potentials) by

$$\vec{B} = \nabla f \times \nabla g \quad (20)$$

Earlier work by Goertz et al. (1976) used an Euler potential approach to model the jovian magnetic field. However, there were problems with this model; namely, all of the components

tend to infinity at  $\rho = 0$  ( $\rho$  is the radial distance from the dipole axis measured in units of  $R_j$ ), and the current sheet crossings were out of phase with observations. To resolve these issues, Khurana (1997) used the spherical harmonic approach to generate the internal field (where Goertz et al. (1976) used an Euler potential approach for both internal and external components) and also allowed  $f$  and  $g$  to be functions of three spatial variables (where in Goertz et al. (1976) they were functions of only two cylindrical coordinates each,  $f(\rho, Z)$  and  $g(\rho, \phi)$ ). The advantages of this approach are the elimination the unreasonably large field at small radial distances and the ability to incorporate the hinging and delay of the current sheet, along with the sweep back of field lines producing radial currents.

The differences between the VIP4 and Khurana models lie within the incorporation of the external magnetic field components. Both models use the same internal spherical harmonic structure. Therefore, close to Jupiter, each model will predict the same magnetic field (see Fig. 27). Further away from the planet, the VIP4 model becomes less accurate while the method employed in the Khurana model holds validity even in the tail region.

In the middle and outer jovian magnetosphere, one of the key variables for organizing the radiation environment is the normal distance from the current sheet,  $Z_{map}$ . It is not possible to define with exact certainty what  $Z_{map}$  actually is for any given energetic charged particle observation. Current sheet crossings from spacecraft data, defined as the location where the radial component of the magnetic field goes to zero, can be identified, but off-sheet locations are difficult to identify uniquely. Therefore, a model must be employed to estimate  $Z_{map}$  when reducing data. Khurana and Schwarzl (2005) have developed a model that finds the  $Z_{map}$  given a location and time. The position of the current sheet above the System-III equator,  $Z_{CS}$ , is given by

$$Z_{CS} = \left( \sqrt{\left( x_H \tanh \frac{x}{x_H} \right)^2 + y^2} \right) \tan \theta_{VIP4} \cos(\phi - \phi') + x \left( 1 - \tanh \left| \frac{x}{x_H} \right| \right) \tan \theta_{sun} \quad (21)$$

where:

- $x_H$  = Current sheet hinging distance
- $x, y$  = JSO coordinates
- $\theta_{VIP4}$  = Dipole tilt angle
- $\phi$  = Longitude angle
- $\phi'$  = Prime meridian where the current sheet elevation is at a maximum
- $\theta_{sun}$  = Angle between the Sun-Jupiter line

Expanding on Eq. 21, it is possible to define the normal direction  $Z_{map}$  by calculating the modeled local gradient of the current sheet. The latest version of the Khurana magnetic field model (Drive\_KT\_2003\_sub.f) has this capability built in. As opposed to building a separate utility, GIRE2 simply pulls the value of  $Z_{map}$  from the Khurana model. (Note: for Khurana's model the variables  $Z_{map}$  and  $Z_N$  are used interchangeably in this report.)

### ***GALILEO EPD DATA***

The outer portion of GIRE2 is primarily based on data collected by the Galileo EPD instrument. The same data cleaning method was used for the outer portion of GIRE2 as was described for the inner portion with a few additional cleaning steps. The outer portion of GIRE2 attempts to describe the energetic electrons in the sheet-like portion of the jovian magnetosphere. All data that appear to be taken outside of the magnetopause within the solar wind were ignored. These data were easily identified by the sudden, sharp decrease in electron count rate to detector threshold levels (see Fig. 29). Additionally, a lower threshold count rate was identified for each EPD channel. All count rate values below the threshold level were ignored because they are more indicative of the EPD detector response at low flux levels than the actual physical flux.

The remaining data were binned by the variables  $R$  and  $Zmap$ . These coordinates are not always orthogonal, but are easy to use and understand for a larger audience. A completely orthogonal coordinate system (radial distance along the equator and  $Zcs$ , for instance) was deemed too cumbersome for use in this model. The radial and  $Z$  distance bins are given in Tables 9 and 10. The  $Zmap$  distance estimated at each data point is the absolute value of  $Zmap$  at that point. North-south symmetry is assumed. Within each data bin, the average value and standard deviation of the count rate data points were then taken. Since the count rate observations can vary over more than an order of magnitude within a given  $R$ - $Zmap$  bin and some bins have relatively few data points, outliers can mathematically skew linear averages. To mitigate this potential problem, data points beyond one standard deviation away from the average were ignored and a second count rate average was taken within the  $R$ - $Zmap$  bin. As a final method to suppress outliers and poor counting statistics, only bins with more than 11 data points were used in the fitting process.

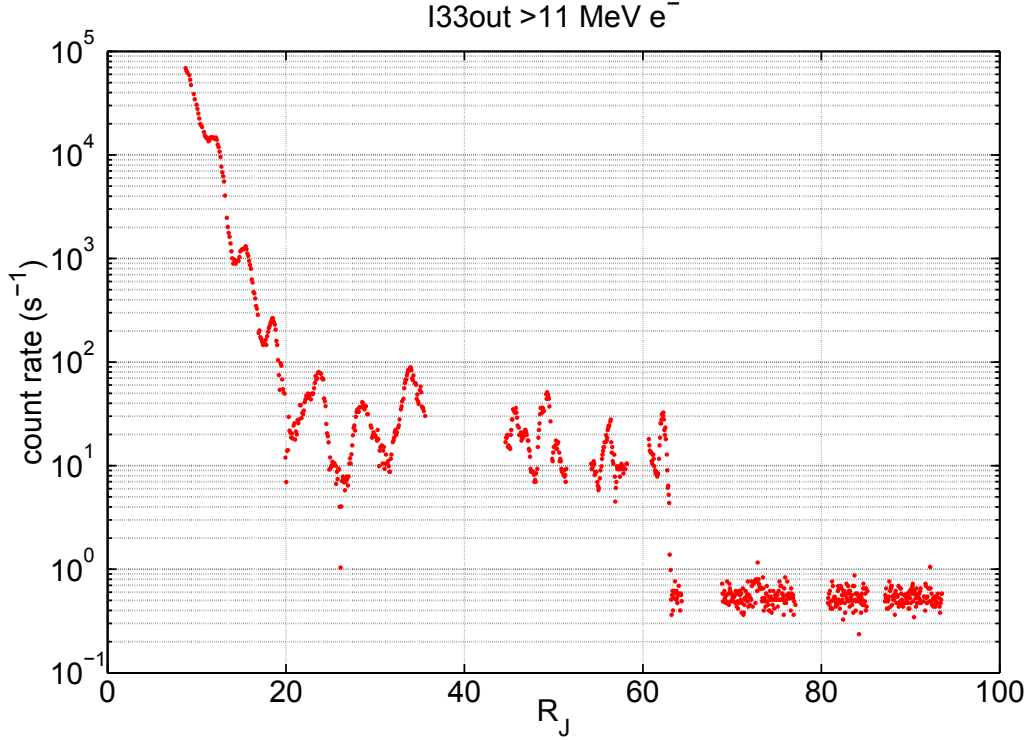


Fig. 29. EPD DC3 (>11 MeV  $e^-$ ) count rate during outbound portion of orbit I33. The count rate falls sharply near 62  $R_J$ . This is interpreted as a transition from the jovian magnetosphere to solar wind. Data collected outside of the magnetosphere are not included in the construction of GIRE2.

### ***FITTING PROCESS***

A robust, nonlinear least-squares fit to the logarithm of the averaged, binned count rate was made to obtain a first order estimate of the energetic electron count rate in the outer sheet-like region of Jupiter's magnetosphere. Each averaged count rate value was weighted by the square root of the number of values used to create the average. The fit follows the form of Eq. 22.

$$\log_{10}(CR) = p_{00} + p_{10}R + p_{01}Z_{map} \quad (22)$$

The resultant fit leads to a solution for the count rate,  $CR$ , as a function of  $R$  and  $Z_{map}$ . This process was repeated for each EPD energy channel. The results are given in Table 11. Comparisons between the averaged count rate and the estimated count rate based on fits to Eq. 22 are shown in Figs. 30–35.

**Table 9. Radial bin values used for the outer portion of GIRE2.**

<b>Rmin</b>	<b>Rmax</b>	<b>Rmid</b>
15	16	15.5
18	17	16.5
17	18	17.5
18	19	18.5
19	20	19.5
20	21	20.5
21	22	21.5
22	23	22.5
23	24	23.5
24	25	24.5
25	26	25.5
26	27	26.5
27	28	27.5
28	29	28.5
29	30	29.5
30	32	31
32	34	33
34	36	35
36	38	37
38	40	39
40	44	42
44	48	46
48	52	50
52	56	54
56	60	58

**Table 10. Z bin values used for the outer portion of GIRE2.**

<b>Zmin</b>	<b>Zmax</b>	<b>Zmid</b>
0	1	0
1	2	1.5
2	3	2.5
3	4	3.5
4	5	4.5
5	7	6
7	10	8.5
10	15	12.5

**Table 11. GIRE2 EPD count rate fit results for each energetic electron energy channel for outer model. Each coefficient is accompanied by a 95% confidence interval estimate. The adjusted R-squared value is also provided as a goodness-of-fit statistic.**

<b>EPD Channel Name</b>	<b>Electron energy range (MeV)</b>	<b><math>p_{00}</math> (with 95% confidence)</b>	<b><math>p_{10}</math> (with 95% confidence)</b>	<b><math>p_{01}</math> (with 95% confidence)</b>	<b>Adjusted R-square</b>
F1	0.174–0.304	4.264 (4.123, 4.405)	−0.04351 (−0.04773, −0.0393)	−0.119 (−0.1405, −0.09742)	0.8913
F2	0.304–0.527	3.854 (3.739, 3.968)	−0.03846 (−0.04189, −0.03502)	−0.1122 (−0.1295, −0.09481)	0.9184
F3	0.527–0.884	3.238 (3.128, 3.348)	−0.0369 (−0.04019, −0.03361)	−0.09359 (−0.1106, −0.0766)	
B1	1.5–10.5	2.429 (2.319, 2.54)	−0.03421 (−0.03751, −0.03091)	−0.07467 (−0.09186, −0.05748)	0.8902
DC2	>2	4.912 (4.787, 5.037)	−0.03853 (−0.04226, −0.03481)	−0.09379 (−0.1137, −0.07391)	0.8688
DC3	>11	2.282 (2.199, 2.364)	−0.0236 (−0.02605, −0.02115)	−0.05856 (−0.07152, −0.0456)	0.9071

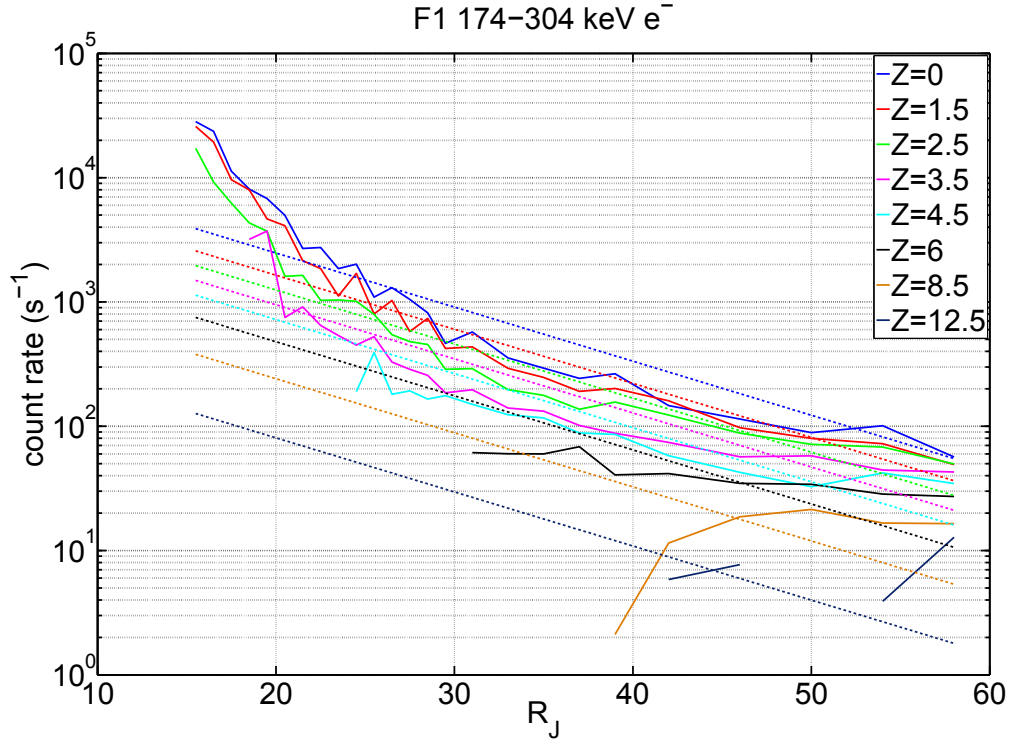


Fig. 30. F1 174-304 keV electron count rate averages (solid) and modeled fit (dashed) as a function of  $R$  for different  $Z_{map}$  values between 0 and  $12.5 R_J$ .

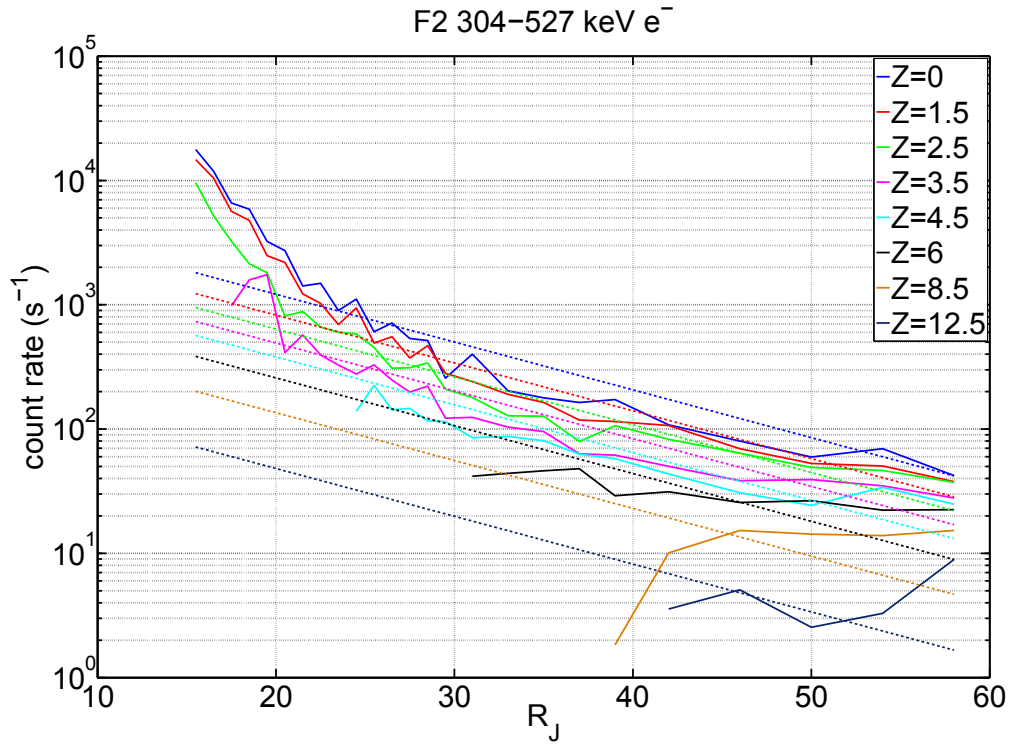


Fig. 31. F2 304-527 keV electron count rate averages (solid) and modeled fit (dashed) as a function of  $R_J$  for different  $Z_{map}$  values between 0 and  $12.5 R_J$ .

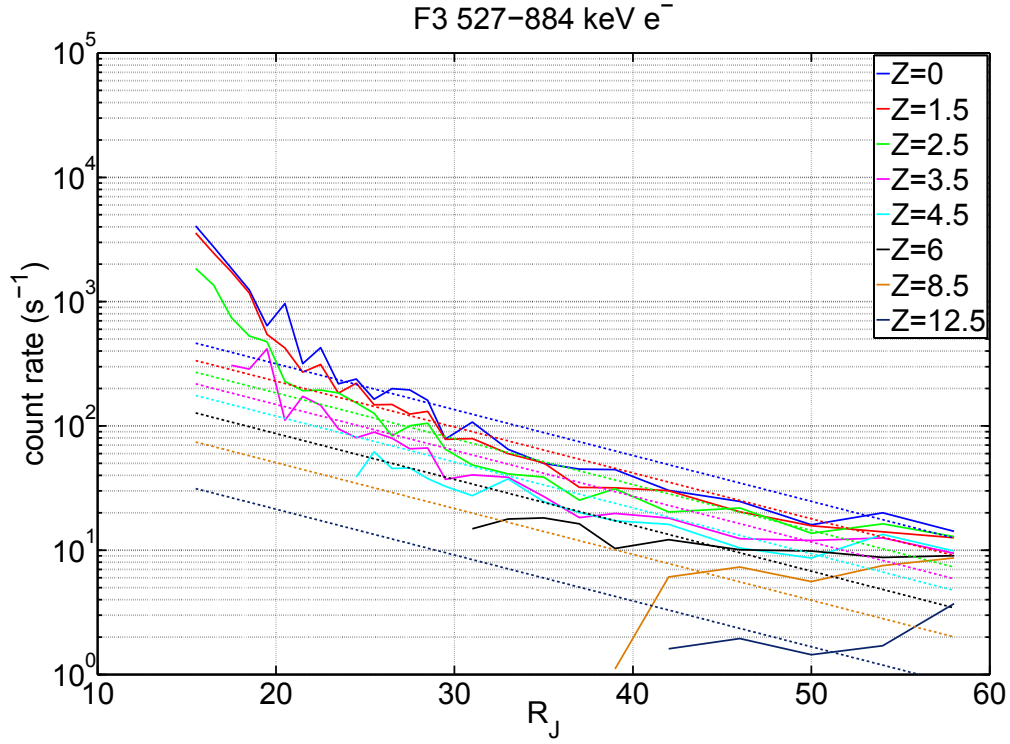


Fig. 32. F3 527-884 keV electron count rate averages (solid) and modeled fit (dashed) as a function of  $R_J$  for different  $Z_{map}$  values between 0 and  $12.5 R_J$ .

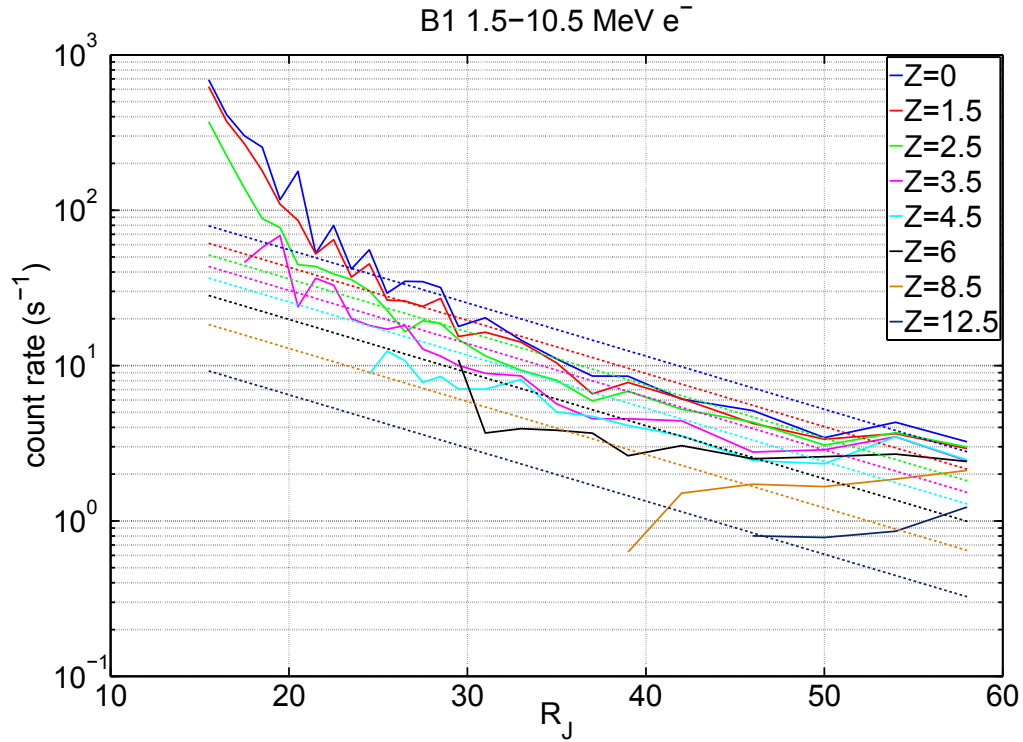


Fig. 33. B1 1.5-10.5 MeV electron count rate averages (solid) and modeled fit (dashed) as a function of  $R_J$  for different  $Z_{map}$  values between 0 and  $12.5 R_J$ .



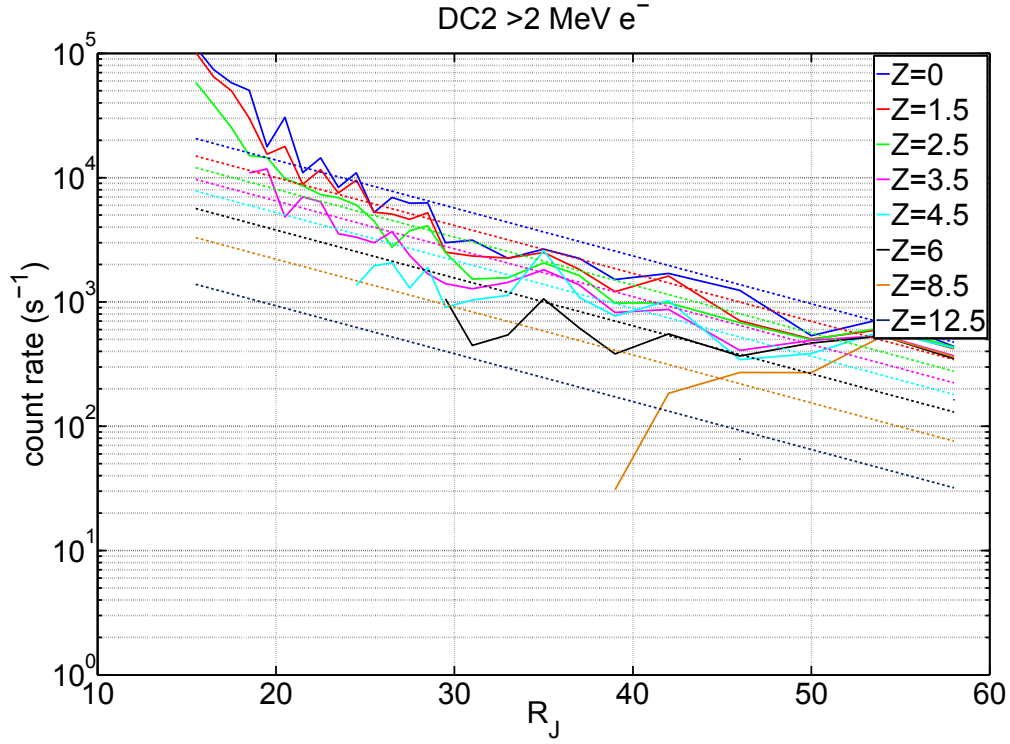


Fig. 34. DC2 >2 MeV electron count rate averages (solid) and modeled fit (dashed) as a function of  $R_J$  for different  $Z_{\text{map}}$  values between 0 and 12.5  $R_J$ .

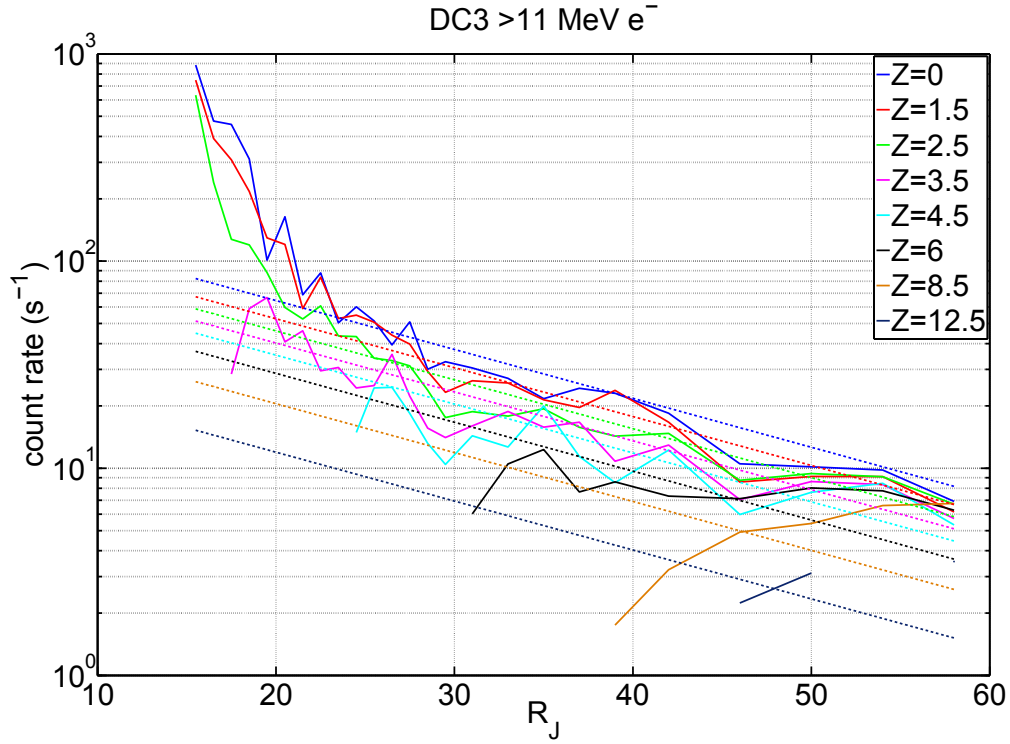


Fig. 35. DC3 >11 MeV electron count rate averages (solid) and modeled fit (dashed) as a function of  $R_J$  for different  $Z_{\text{map}}$  values between 0 and 12.5  $R_J$ .

### **CONVERTING THE OUTER MODEL COUNT RATES TO FLUXES**

As just discussed, outside of  $\sim 15$  R<sub>J</sub>, all the EPD count rates were directly fit with a simple functional form in terms of R<sub>J</sub> and the parameter  $Z_{map}$  as defined by the Khurana magnetospheric model (Khurana and Schwarzl, 2005).  $Z_{map}$  represents the distance from the model's estimated center of the jovian plasma sheet and the spacecraft position. It is variable in local time relative to the Sun and radial distance from Jupiter. To repeat, the functional form is given by:

$$\log_{10}(CR) = p_{00} + p_{10}R + p_{01}Z_{map} \quad (23)$$

where:

$CR$  = Electron count rates at  $E$

$E$  = Electron energy; 0.239, 0.416, 0.706, 1.5, 2.0, 11.0 MeV

$p_{00}, p_{10}, p_{01}$  = Constants determined by fits to data (Table 11)

$Z_{map}$  = Perpendicular distance from jovian plasma sheet to location of observation

$R$  = Radial distance from Jupiter's center to location of observation

The 31 MeV differential fluxes based on Pioneer 10 and 11 were approximated using Eq. 14. The 6 fitted count rates and the 31 MeV channel were then converted to spectra as defined by Eq. 15 using the regression methods discussed earlier. To simplify interpolation in  $(R, Z_{map})$ , each of the constants ( $J_0, A, B, E_0$ ) in Eq. 15 were then fit using a multiple linear regression program to an equation of the form:

$$Y(R, Z_{map}) = A_0 + A_1R + A_2Z_{map} + A_3R^2 + A_4Z_{map}^2 + A_5R \cdot Z_{map} + A_6R^2Z_{map} + A_7R \cdot Z_{map}^2 + A_8R^2Z_{map}^2 \quad (24)$$

where:

$Y = J_0, A, B, E_0$  = the constants in Eq. 15 used to generate the differential flux  $F(E, R, Z_{map})$

**Table 12. Constants for Eq. 24 used to give  $(J_0, A, B, E_0)$  for the outer electron model distribution as a function of  $(R, Z_{map})$ .**

	<b>log(<math>J_0</math>)</b>	<b>A</b>	<b>B</b>	<b>log(<math>E_0</math>)</b>
$A_0$	2.141327	2.552827	1.724840	1.266312
$A_1$	-3.152989E-02			
$A_2$	-7.022678E-02	-5.676055E-02	-1.026922E-01	-1.240556E-01
$A_3$		-1.392466E-04	-1.014636E-04	-4.963554E-05
$A_4$		-1.016197E-03	7.114015E-03	3.995305E-03
$A_5$		-7.700121E-04		
$A_6$	-7.062619E-07		1.493074E-05	
$A_7$				
$A_8$		9.804245E-07	-1.206777E-06	

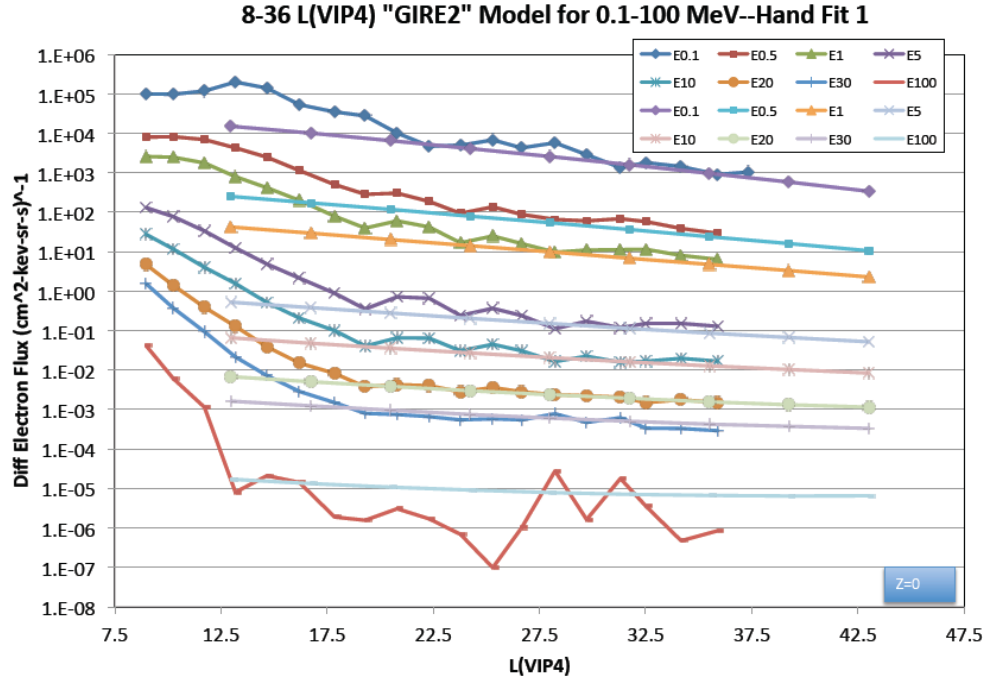


Fig. 36. The outer model differential electron fluxes (at  $Z_{\text{map}} = 0$ ) compared with the inner model estimates versus  $L$  as determined by the Khurana magnetic field model.

This gives a simple representation in  $(R, Z_{\text{map}})$  for the region outside the  $\sim 15$   $L$  (as determined by the Connerney magnetic field model) magnetic field lines. The fitted constants for the  $(J_0, A, B, E_0)$  values are given in Table 12. Based on this formulation, the predicted fluxes at  $Z_{\text{map}}=0$  are compared with the inner model fluxes in terms of  $L$  in Fig. 36. The close agreement between the two models between  $\sim 17$ – $35$   $L$  provides a useful validation of the outer model near the magnetic equator ( $Z_{\text{map}}=0$ ) given the very different fitting techniques employed to arrive at these fits.

### COMBINING THE INNER AND OUTER GIRE2 MODELS

The fact that the inner trapped model is based on  $L$  and the Connerney magnetic field model while the outer plasma sheet model is based on the Khurana model and  $(R, Z_{\text{map}})$  means there is a discontinuity between the two models that varies along the  $L$ -shell and in local time. This behavior is particularly pronounced for the original GIRE/Divine model combination and clearly evident in Fig. 37—note the sharp discontinuities at the inner ( $\sim 8$   $L$ ) and outer boundaries ( $\sim 16$   $L$ ).

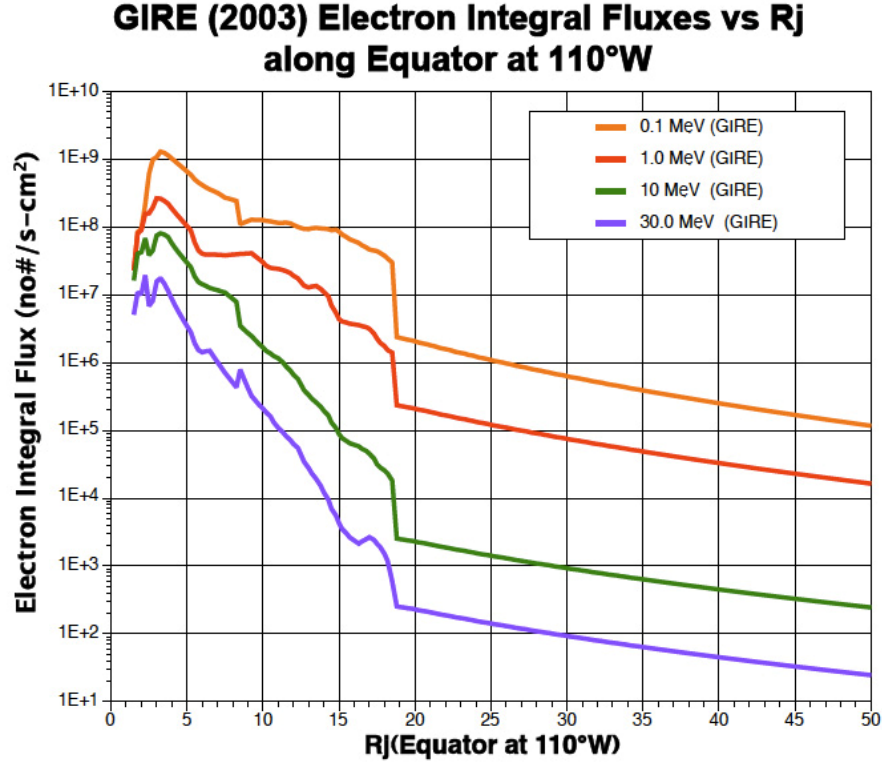


Fig. 37. “GIRE+Divine (2003)” integral fluxes ( $n^{\#}/cm^2 \cdot s$ ) at: 0.1, 1.0, 10.0, 30.0 MeV showing discontinuities at  $\sim 8$  and  $\sim 16$   $R_j$ .

In GIRE2, the inner and outer models were smoothly merged by assuming the following approximation in the region 17 to 22.5  $L$ :

$$F2(E, L, R, Z_{map}) = F_{inner}(E, L) \cdot (22.5 - L) / 5.5 + F_{outer}(E, R, Z_{map}) \cdot (L - 17) / 5.5 \quad (25)$$

This method was also used to smoothly join the new inner, trapped model with the Divine model between 7.2 and 10.5  $L$ :

$$F2(E, L, R, Z_{map}) = F_{inner}(E, L) \cdot (L - 7.2) / 3.3 + F_{Divine}(E, L) \cdot (10.5 - L) / 3.3 \quad (26)$$

where:

$F2$  = Interpolated differential electron flux as a function of  $(E, L, R, Z_{map})$  between 17–22.5  $L$  and 7.2 and 10.5  $L$ .  $(R, Z_{map})$  are based on the Khurana model while  $L$  is based on the Connerney magnetic field model.

$F_{inner}$  = Differential flux as determined for the inner trapped region (7.2–22.5  $L$ )

$F_{outer}$  = Differential flux as determined for the outer plasma sheet region ( $\sim 17$ –50  $R_j$ )

$F_{Divine}$  = Differential flux as determined for the Divine model inside 10.5  $L$ .

The results are presented in Fig. 38. The procedure, although simplistic, does a good job of smoothly joining the models.

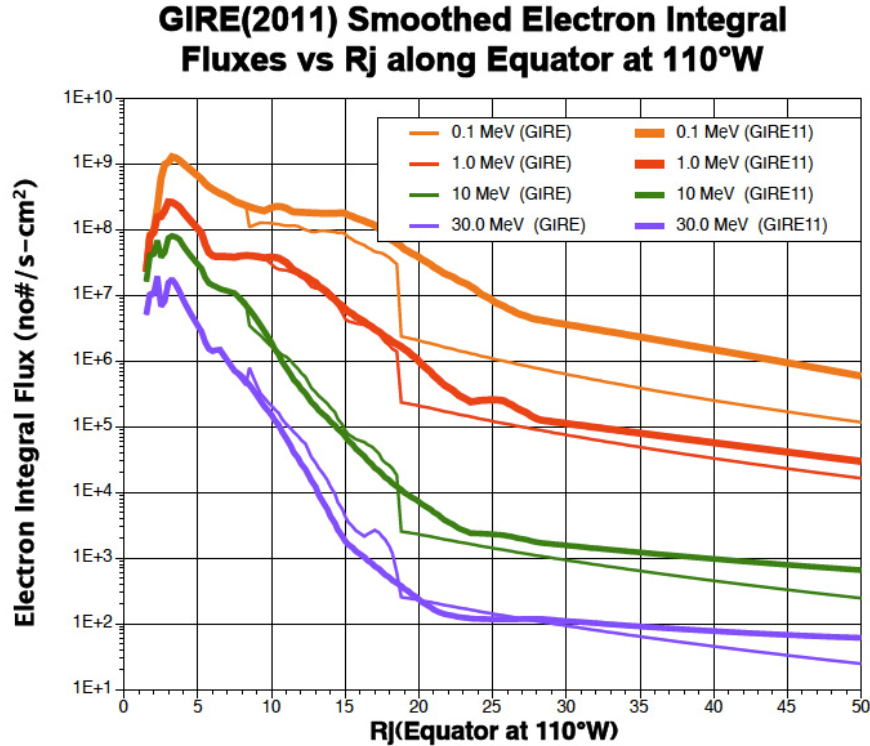


Fig. 38. Comparisons between original “GIRE+Divine (2003)” and the new “GIRE (2011)” integral fluxes ( $\text{n}^\#/\text{cm}^2\text{-s}$ ) at: 0.1, 1.0, 10.0, 30.0 MeV along the jovian equatorial plan at 110°W. Note that the discontinuities between the models have virtually disappeared in the GIRE2 model.

## *CONCLUSIONS*

### **The GIRE2 Omnidirectional, Equatorial Flux Model-Summary**

Previous information on Jupiter's electron belts came from the in-situ measurements of only four planetary flybys. As such, there was very limited temporal coverage making it difficult to determine the average environment and to know how much and how often it varied. The 35 orbits of Galileo EPD data studied here are significantly better in this regard, as the data are collected on parts of each orbit, separated by intervals of one to a few months, and over a 7-year period. The Galileo EPD instrument provides extensive data on the electron radiation environment close to the jovian equatorial plane at jovicentric distances between 8 and 100 R<sub>j</sub> (Jupiter radii) and over the energy range ~0.5 to ~11 MeV. Given this data coverage and the detailed simulation of the EPD instrument response, the derived particle fluxes should be a very good representation of this portion of the jovian electron environment. For spacecraft trajectories in the equatorial plane that do not venture inside 8 R<sub>j</sub> and that have moderate shielding protection (in the range of 50 to 500 mils (1.27 to 12.7 mm) aluminum through which electrons of a few MeV will pass), the EPD flux model is expected to give a good estimate of the radiation exposure of a spacecraft.

Based on the Galileo data, a model has been developed that gives the average omnidirectional electron flux seen by the EPD instrument between  $\sim 8 R_J$  and  $\sim 50 R_J$  (inside  $8 R_J$  the original Divine model is used with recent synchrotron data modifications inside  $L=5$ ). It provides estimates of the average exposure of a spacecraft near the jovian equator that is in the radiation belts for several months. A substantial portion of the radiation exposure behind shielding thicker than 500 mils (12.7 mm) of aluminum comes from electrons the EPD instrument does not measure—that is, electrons having more than 11 MeV of energy. For dose behind these thicker shields, the EPD flux model had to be augmented. Earlier mission flybys have provided data at higher electron energies than were measured by the EPD instrument. In particular, the Pioneer 10 and 11 energetic particle instruments measured 21 and 31 MeV electrons and were extensively calibrated. The resulting fluxes fit in terms of  $L$  and  $(R, Z_{map})$  have been used in combination with the EPD data to obtain functional fits of the electron energy spectra to 31 MeV.

An additional issue is that the GIRE2 flux inner model also does not give any information about the variation of electron flux with latitude. The small excursions of Galileo from the magnetic equatorial plane were not large enough to yield detailed latitude information based on the omnidirectional data alone. Because the Real Time EPD data were integrated over a nearly complete solid-angle sphere for the high-energy channels, there is no direction-specific information that would give the variation of flux with pitch angle, which determines variation with latitude—hence the term omnidirectional in the description of the model. However, because the outer model uses  $Z_{map}$  as a variable, latitude variations are implicitly included in that component of GIRE2. G. Clough (Garrett et al., 2003) has made use of the limited Record Mode data which did measure pitch angle information to study the electron and proton flux variations with latitude. We hope in future studies to incorporate those results into the model.

## **Issues with GIRE2**

The preceding sections have described the Galileo EPD instrument and carefully detailed the steps followed to convert that instrument's high-energy electron count rate data into particle fluxes for the energy range  $\sim 0.5$  to 31 MeV. Some internal inconsistency between the B1 and DC2 channels' data was found, but it was not great enough to preclude construction of a model of the omnidirectional electron fluxes on the jovian equatorial plane. Several factors could contribute to the inconsistency: over-estimation of the magnetic deflection field's effect on the B1 channel's geometric factor; a pitch-angle dependence that causes differences in spin-averaging between the  $0^\circ$  end and  $180^\circ$  end of the telescope; over-compensation in the dead-time correction of the DC2 channel, which gets multiplicative correction factors from 1.5 to 2 at its highest rates; or an artifact of the fitting routines and fitting functions used to make the comparisons. These possibilities have not yet been explored in sufficient detail to identify the culprits.

The GIRE2 model is considered interim in the sense that there is room for improved analysis of the data used for the GIRE2 model, and there are additional EPD data (at smaller  $R_J$  and as a function of pitch angle) that have yet to be considered. The internal inconsistency between B1 and DC2, and the large dead-time correction factor needed for DC2, both suggest systematic error in the model could be as much as a factor of two. That was also the estimated

error in the Divine model, but it was the error between the measured environment and the model; it presumed the measured environment was the average environment. What is significantly different about the EPD data is that their temporal variations, to the extent that average and severe flux levels can be defined, have been studied in detail (see Jun et al., 2005).

The electrons the F channels measure are too low in energy to be a radiation threat, except perhaps to spacecraft surface coatings. Their inclusion in the spectrum fitting process, however, changes not only the low-energy regime, but also the extrapolation into the high-energy regime beyond the data point at 31 MeV. This can be considered an artifact of the fitting procedure, but it makes evident the fact that there is no clearly "correct" way to extrapolate into the high-energy regime.

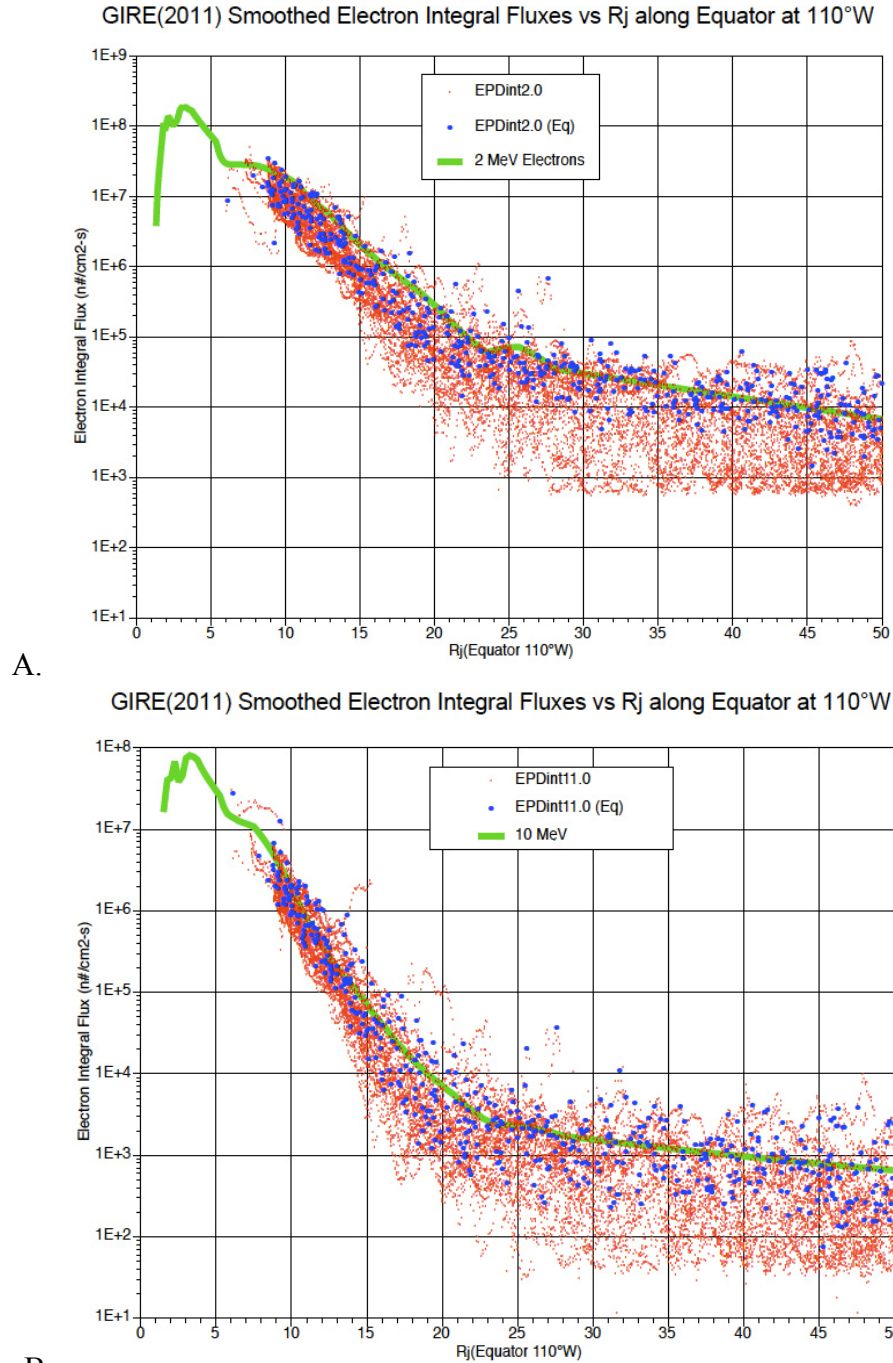
Aside from a portion of Galileo's inbound pass on orbit C22, the electron flux variations for the approximately 35 orbits were surprisingly similar from orbit to orbit as a function of radial distance. There is speculation about what actually occurred during what appears to be a large storm during C22, but no definitive explanation has been advanced. The fact that it was one event out of 30, and that it seemed to be a very short-lived phenomenon (as it was not evident a few hours later during Galileo's outbound pass), suggests such an event will not likely produce a serious enhancement of the radiation exposure to a spacecraft in orbit. (Note: There are ~6 other similar events in other orbits to that in C22, but these were several orders of magnitude smaller than the C22 event and not considered here.)

### **Limits on GIRE2 and its Validity**

To give an indication of the ability of the GIRE2 model to "predict" the radiation environment at Jupiter, Figs. 39A and 39B compare the predicted electron fluxes for all the 10-minute EPD data—the red values are for the entire EPD database, the blue values correspond to Khurana's magnetic equator crossings, and the green line to the GIRE2 predictions for the jovian equator ( $0^\circ$  latitude SIII) for a cut at  $110^\circ$ W (SIII) (note:  $(0^\circ, 110^\circ$ W) corresponds roughly to the magnetic equator at that longitude and  $Z_{map} \sim 0$ ). The figures demonstrate that the model does a very good job of fitting the magnetic equatorial fluxes. Further, within about 20 R<sub>J</sub> the equatorial crossing data are very representative of the overall data set—this implies that an assumption of omnidirectionality for the ~8–20 L range is adequate for our purposes. Beyond 20 R<sub>J</sub> the overall database deviates from the equatorial values as the data fall off with  $Z_{map}$  as would be expected. Here GIRE2 (for  $Z_{mag} = 0$  in this case) predicts the average of the equatorial crossings pretty well and represents a good upper limit for the data set as it should.

Another issue is the range of applicability of the GIRE2 model. Strictly, the Galileo data sources limit it to within a few degrees of the jovian equator with some extension to other latitudes by the Pioneer, Voyager, and remote sensing. For the inner, trapped region ( $<22.5$  L), the coverage is complete given either the pitch angle distributions of Divine or the assumption of omni-directionality. The outer model is, in principle, limited to a cylindrical region between ~15 R<sub>J</sub> to 50 R<sub>J</sub> in horizontal extent and  $\pm 12$  R<sub>J</sub> in  $Z_{map}$ . Though the model does not technically predict inside this cylinder and outside the L-shell at ~22.5, the outer GIRE2 model can be simply extrapolated between 0 to 20 R<sub>J</sub> to fill this "void". This is illustrated in the contour plots of the integral electron fluxes in Figs. 40A and 40B. The smoothing technique we have used

leads to what appear to be “reasonable” fluxes in this “undefined” region(s) inside  $\sim 25$  R<sub>j</sub> and outside 22.5 L—we cannot verify the reliability of the predictions in this region, however.



B.

Fig. 39. Comparisons between all (red) EPD data, Khurana crossings (blue), and new “GIRE(2011)” (green) electron integral fluxes ( $n\#/cm^2-s$ ) at A) 2.0 and B) 11.0 MeV



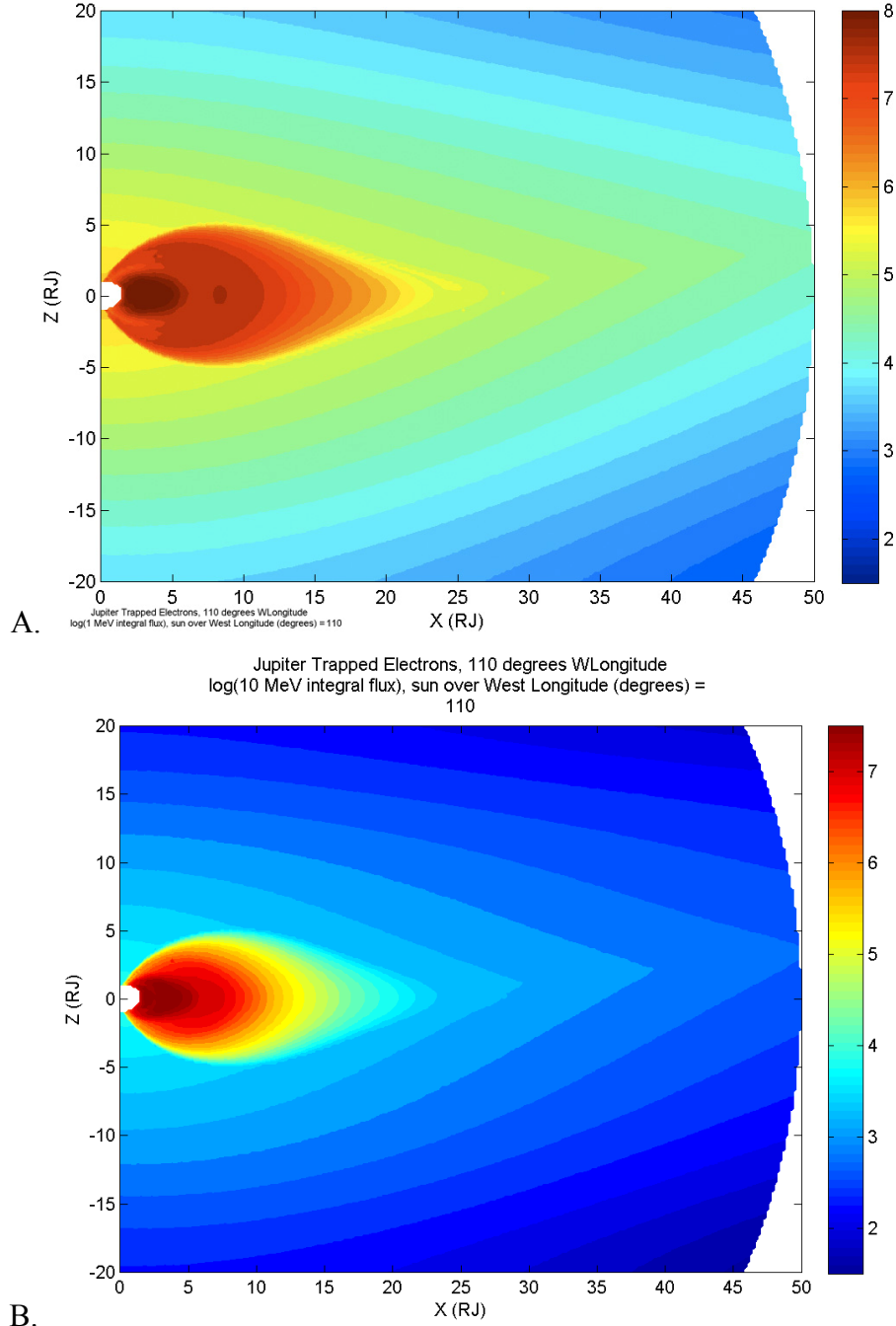


Fig. 40. Meridian contours of GIRE2 (A) 1 MeV and (B) 10 MeV electron integral fluxes ( $\text{cm}^{-2}\text{s}^{-1}$ ) for the  $110^\circ\text{W}$  meridian and for the Sun at  $110^\circ\text{W}$ . Note that the “outer” GIRE2 model has been extrapolated inwards of  $\sim 15 R_j$  and up to  $\pm 20$  in  $Z_{\text{map}}$  to fill in the region outside an  $L$  of 22.5.

A final issue is the energy range of validity of the GIRE2 electron data. As currently formulated, the model is strictly only valid for the energy range from  $\sim 0.5$  MeV (the F-channels) to  $\sim 11$  MeV (the DC channels). We have extended the apparent energy range of the GIRE2 model up to 31 MeV for the electrons by using fitted values to the 21-31 MeV electron fluxes as observed by Pioneer 10 and 11. While this extension is believed to be valid, given  $\sim 20$  years that

separates the data sources and the possibility of long term variations in the jovian environment, this cannot be formally validated. We suggest that the electron model is valid up to at least 11 MeV, reasonably extendable up to  $\sim 30$ – $50$  MeV, and probably not reliable above  $\sim 50$  MeV. The results can certainly be extrapolated up to  $\sim 200$  MeV but this is subject to very significant uncertainties.

## **Accomplishments**

The GIRE (Galileo Interim Radiation Electron) jovian radiation model was updated to the GIRE2 model by extending the equatorial range from  $\sim 15$  to  $\sim 50$  R<sub>J</sub>. Unlike GIRE, GIRE2 makes use primarily of data near the magnetic equator—despite this difference, the models agree quite well where they overlap (e.g., Fig. 25). As before, the inner portion of the model was merged with the Divine model. Separately a computer code version of the GIRE2 model has been developed (Garrett et al., 2011) that allows the user to estimate the radiation fluence for a given input trajectory. Finally, future work will address the unique variations in orbit C22, complete the pitch angle analysis, and reconcile remaining inconsistencies in the data. Even so, while more information still remains to be extracted from the EPD data, the GIRE2 model represents a significant step forward in the study of the jovian radiation environment, and is a useful and valuable tool for estimating that environment for future space missions to Jupiter over the entire range of the jovian radiation belts from  $\sim 1$  to  $\sim 50$  R<sub>J</sub>.

## ***ACKNOWLEDGMENTS***

The authors would like to thank R. Carlson for his helpful review comments. We further appreciate the help of Dr. R. W. McEntire and his colleagues at APL who provided the original EPD data and helped explain the operation of the experiment. We particularly want to thank Prof. K. K. Khurana of UCLA who provided his models of the jovian magnetic field and his estimates of the times and locations of the Galileo crossings of the jovian magnetic equator. These inputs allowed a significant step forward in our modeling of the jovian radiation environment.

## REFERENCES

- Baker, D. N., and J. A. Van Allen, "Revised Pioneer 10 absolute electron intensities in the inner Jovian magnetosphere," *J. Geophys. Res.*, **82** (4), 681–683, 1977.
- Connerney, J. E. P., "Doing More With Jupiter's Magnetic Field," in *Planetary Radio Emissions III*, edited by H. O. Rucker, et al., Österreichischen Akademie Der Wissenschaften, Vienna, Austria, 1992
- Connerney, J.E., M.H. Acuna, N.F. Ness, and T. Satoh, "New models of Jupiter's magnetic field constrained by the Io flux tube footprint," *J. Geophys. Res.*, **103** (A6), 11929–11940, 1998.
- Divine, T.N., and H.B. Garrett, "Charged particle distributions in Jupiter's magnetosphere," *J. Geophys. Res.*, **88** (A9, Sept.), 6889–6903, 1983.
- Garrett, H. B., I. Jun, J. M. Ratliff, R. W. Evans, G. A. Clough, and R.W. McEntire, "Galileo Interim Radiation Electron Model," *JPL Publication 03-006*, 72 pages, Jet Propulsion Laboratory, California Institute of Technology, Pasadena, CA, 2003.  
<http://www.openchannelfoundation.org/projects/GIRE/>
- Garrett, H. B.; Levin, S. M., Bolton, S. J., Evans, R. W., Bhattacharya, B., "A revised model of Jupiter's inner electron belts: Updating the Divine radiation model," *Geophys. Res. Lett.*, **32** (4), L04104 <http://dx.doi.org/10.1029/2004GL021986>, February 26, 2005.
- Garrett, H. B., M. Kokorowski, I. Jun, and R. W. Evans, "Galileo Interim Radiation Electron Model Update—2011," *JPL IOM-5130-11-053*, Jet Propulsion Laboratory, Pasadena, CA, November 29, 2011
- Goertz, C. K., et al., "Evidence for open-field lines in Jupiter's magnetosphere," *J. Geophys. Res.*, **81** (19), 3393–3398, 1976.
- Joy, S. P., M. G. Kivelson, R. J. Walker, K. K. Khurana, C. T. Russell, and T. Ogino, "Probabilistic models of the Jovian magnetopause and bow shock locations," *J. Geophys. Res.*, **107** (A10), 1309, doi:10.1029/2001JA009146, 2002.
- Jun, I., J.M. Ratliff, H.B. Garrett, and R.W. McEntire, "Monte Carlo simulations of the Galileo energetic particle detector," *Nucl. Instr. and Meth. A*, **490**, 465–475, 2002.
- Jun, I., H.B. Garrett, R. Swimm, R.W. Evans, and G. Clough, "Statistics of the variations of the high-energy electron population between 7 and 28 jovian radii as measured by the Galileo spacecraft," *Icarus*, **178**, pp. 386–394, doi:10.1016/j.icarus.2005.01.022, 2005.
- Khurana, K. K., "Euler potential models of Jupiter's magnetospheric field," *J. Geophys. Res.*, **102** (A6), 11295, 1997.
- Khurana, K. K., "A generalized hinged-magnetodisc model of Jupiter's Nightside current sheet," *J. Geophys. Res.*, **97** (A5), 6269, 1992.
- Khurana, K. K., and H. K. Schwarzl, "Global structure of Jupiter's magnetospheric current sheet," *J. Geophys. Res.*, **110** (A07227), 2005. doi:10.1029/2004JA010757.
- Kokorowski, M., "Using the VIP4 and Khurana Jupiter magnetic field models to calculate the L-parameter", *JPL-IOM 5132-10-047*, Jet Propulsion Laboratory, Pasadena, CA, 2010.
- Lagg, A., "Galileo EPD Science Team Meeting," March, 1998.
- Navigation and Ancillary Information Facility NAIF, *SPICE*, <http://naif.jpl.nasa.gov/naif/>, accessed 2011.
- Parks, G. K., *Physics of Space Plasmas*, Westview Press, Boulder, Colorado, 1991.
- Smith, E. J., et al., "Jupiter's Magnetic Field and Magnetosphere", in *Jupiter*, edited by T. Gehrels, pp. 788–829, University of Arizona Press, Tucson, 1976.

- Stern, D. P., "Euler potentials," *Amer. J. Phys.*, 38, 494, 1970.
- Stern, D. P., "Representation of magnetic fields in space," *Rev. Geophys.*, vol. 14, no. 2, pp. 199-214, 1976, doi:10.1029/RG014i002p00199.
- Thomas, G.R., and D.M. Willis, "Analytical derivation of the geometric factor of a particle detector having circular or rectangular geometry," *J. Phys. E: Scientific Instruments*, 5, 260–263, 1972.
- Van Allen, J.A., D.N. Baker, B.A. Randall, M.F. Thomsen, and D.D. Sentman, "The magnetosphere of Jupiter as observed with Pioneer 10, 1. Instrument and principal findings," *J. Geophys. Res.*, 79, 3559–3577, 1974.
- Van Allen, J.A., B.A. Randall, D.N. Baker, C.K. Goertz, D.D. Sentman, M.F. Thomsen, and H.R. Flindt, "Pioneer 11 observations of energetic particles in the Jovian magnetosphere," *Science*, 188, 459–462, 1975.
- Van Allen, J. A., "High-energy particles in the Jovian magnetosphere", in *Jupiter*, edited by T. Gehrels, pp. 928–960. University of Arizona Press, Tucson, 1976.
- Williams, D.J., R.W. McEntire, S. Jaskulek, and B. Wilken, "The Galileo Energetic Particle Detector," in *The Galileo Mission*, edited by C.T. Russell, pp. 385–412, Kluwer Academic Publishers, Dordrecht, The Netherlands, 1992.

## ***APPENDIX I. ACRONYMS AND ABBREVIATIONS***

APL	(Johns Hopkins University) Applied Physics Laboratory
CMS	Composition Measurement System
CR	count rate
CTS	counts per second
EPD	(Galileo) Energetic Particle Detector
ET	Solar System Barycentric Ephemeris Time
FT	Fundamental Technologies, Inc.
GIRE	Galileo Interim Radiation Electron
GIRE2`	Galileo Interim Radiation Electron
GTT	Geiger Tube Telescope
JHU	Johns Hopkins University
JOI	Jupiter orbit insertion
KU	The University of Kansas
LEMMS	Low-Energy Magnetospheric Measurement System
MAG	(Galileo) Magnetometer
MCNP	Monte Carlo N-Particle Transfer Code
MCNPX	Monte Carlo N-Particle eXtended Code
NAIF	(NASA) Navigation and Ancillary Information Facility
PDS	Planetary Data System
R <sub>j</sub>	Jupiter radius, 71,400 km
UT	Universal Time